Westbrook, G.K., Carson, B., Musgrave, R.J., et al., 1994
Proceedings of the Ocean Drilling Program, Initial Reports, Vol. 146 (Part 1)

4. SITE 888[1]

Shipboard Scientific Party[2]

HOLE 888A

Date occupied: 26 September 1992

Date departed: 26 September 1992

Time on hole: 8 hr, 15 min

Position: 48°10.009′N, 126°39.794′W

Bottom felt (rig floor; m; drill-pipe measurement): 2527.0

Distance between rig floor and sea level (m): 10.70

Water depth (drill-pipe measurement from sea level; m): 2516.3

Total depth (rig floor; m): 2536.50

Penetration (m): 9.50

Number of cores (including cores with no recovery): 1

Total length of cored section (m): 9.50

Total core recovered (m): 9.75

Core recovery (%): 102

Oldest sediment cored:
Depth (mbsf): 9.50
Nature: clayey silt
Earliest age: Holocene

HOLE 888B

Date occupied: 26 September 1992

Date departed: 3 October 1992

Time on hole: 6 days, 9 hr, 50 min

Position: 48°10.009′N, 126°39.794′W

Bottom felt (rig floor; m; drill-pipe measurement): 2527.0

Distance between rig floor and sea level (m): 10.70

Water depth (drill-pipe measurement from sea level; m): 2516.3

Total depth (rig floor; m): 3093.90

Penetration (m) 566.90

Number of cores (including cores with no recovery): 65

Total length of cored section (m): 566.90

Total core recovered (m): 364.85

Core recovery (%): 64

Oldest sediment cored:
Depth (mbsf): 566.90
Nature: interbedded clayey silt and sandy silt
Earliest age: late Pleistocene

HOLE 888C

Date occupied: 3 October 1992

Date departed: 5 October 1992

Time on hole: 1 day, 18 hr, 30 min

Position: 48°9.985′N, 126°39.802′W

Bottom felt (rig floor; m; drill-pipe measurement): 2527.0

Distance between rig floor and sea level (m): 10.80

Water depth (drill-pipe measurement from sea level; m): 2516.2

Total depth (rig floor, m): 3127.0

Penetration (m): 600.0

Number of cores (including cores with no recovery): 0

Principal results: Site 888 lies in an outer part of the Nitinat Fan, 7 km seaward of the toe of the accretionary wedge that forms the continental margin off Vancouver Island. The site provides a reference for the types, age, and physical properties of sediment in the sedimentary section that is stripped from the oceanic crust to form the accretionary wedge. The state of compaction and thermal structure of the sedimentary section are of particular relevance to understanding the mechanisms of growth of accretionary wedges and associated expulsion of pore water. The geochemistry of the pore fluids provides indicators of fluid movement, and it is important to define the distribution of organic and inorganic species within the sedimentary section before subduction or accretion.

The holes at Site 888 penetrated into the top 600 m of the sedimentary section, which the seismic section from line 89-04 shows has a total thickness of 2.5 km. The lower 1.5 km of the section has the appearance of a sequence of distal turbidites. The character of the upper 1 km shows the proximity of a submarine fan, with channels, lateral thickness changes, erosional surfaces, and localized progradation.

Three lithostratigraphic units were recognized at Site 888:

Unit I (0–175.1 m below seafloor [mbsf]): Holocene to upper Pleistocene, interbedded gray to dark greenish gray clayey silts, and gray to dark gray, fine- to medium-grained sands, with some thin beds containing pebbles, volcaniclastic fragments, and pieces of wood. Between Units I and II is a transition zone, in which there is a gradual increase with depth in the proportion of massive sand.

Unit II (193.0–457.0 mbsf): upper Pleistocene, thick beds (>1 m) of massive dark gray, fine- to medium-grained sand with interbeds of clayey silt. Unit II is predominantly sandy, and core recovery from it was poor. The sands are poorly sorted.

Unit III (457.0–566.9 mbsf): upper Pleistocene, dark gray, firm clayey silt and silt, finely laminated with thin interbeds of fine to coarse sand and gravel. Unit III may be divided into two subunits: IIIA (457.0–496.0 mbsf) comprising predominantly silts showing incipient lithification, and IIIB (496.0–566.9 mbsf) comprising clayey silts with sands, and also containing isolated pebbles of granite, granodiorite, basalt, and quartzite, which may be glacial dropstones.

Within the three lithostratigraphic units, three submarine fan facies types were recognized, which are described as Facies B, C, and D, after the model of Mutti and Ricci Lucchi (1972). Facies C and D, the products of deposition by normal-density and low-density turbidity currents, respectively, are represented in Unit I, with Facies D predominant. All three facies types occur in Unit II, but the sands of Facies B are the principal type. The facies

[1] Westbrook, G.K., Carson, B., Musgrave, R.J., et al., 1994. *Proc. ODP, Init. Repts.,* 146 (Pt. 1): College Station, TX (Ocean Drilling Program).
[2] Shipboard Scientific Party is as given in the list of participants preceding the contents.

association of Unit II is the "middle fan subassociation." Lithostratigraphic Unit III comprises facies types C and D, which form an "outer fan subassociation." The turbidites in Unit III are of a more distal character than those in Unit I.

The magnetic polarity of the whole of the cored interval is normal, except for a short interval at 100 mbsf that may correspond to the Blake Event of 110 ka. The section is therefore younger than 780 ka. Biostratigraphic control was poor. Radiolarians of the *Botryostrobus aquilonaris* Zone (less than 450 ka) were found to a depth of 170 mbsf. The dominance of sinistral *Neogloboquadrina pachyderma* throughout the sequence indicates that the age of the entire cored section at Site 888 is younger than 600 ka.

The geothermal gradient has been established as 68°C/km, from 11 good measurements of temperature down to 315 mbsf. Thermal conductivity measurements in the sediment cores increase in value downward through the uppermost 200 m to a mean value of 1.23 W/(m · K) for the section below that depth. The thermal gradient and conductivities yield a heat flow of about 73 mW/m^2 near the seafloor, which increases through Unit I to reach a value of 84 mW/m^2 through Units II and III. The upward decrease in heat flow is probably a consequence of the absorption of heat by the cool, rapidly deposited sediments.

Measurements of porosity and shear strength indicate that sediments in the cored intervals are underconsolidated. Wireline density and neutron logs show that the minimum porosity of the section lies at 300 mbsf. The downward increase in porosity shown by these logs beneath 300 mbsf, however, may be an artifact of poor hole conditions, especially in the case of the density log, which requires good contact with the wall of the hole. Porosity measured in core samples decreases with depth below 300 mbsf, as does porosity derived from the resistivity log. Sonic velocities also increase with depth below 300 mbsf. The general state of undercompaction indicated by the logs and the measurements of physical properties may be attributed to rapid deposition, especially of the sandy section of Unit II. A good match between the seismic section and the synthetic seismogram derived from the logs enables the section to be accurately correlated with data from the holes at the site.

The geochemistry of the pore water in the section varies downward in response to bacterial sulfate reduction, carbonate diagenesis, and fluid flow within some intervals. The variations in several species are, however, quite moderate in comparison with the other sites, such as Site 889, in the accretionary wedge. For example, chloride varies between 543 and 571 mM at Site 888, but at Site 889 chloride varies between 350 and 550 mM. Geochemical analyses of pore fluids and gases revealed several interesting aspects of fluid flow, gas migration, and diagenesis in the section. At 70 mbsf there is a sharp decrease in the concentration of chloride of 12 mM from 571 mM, to which it had steadily increased from 545 mM at the seafloor. Also, a pronounced minimum in chloride of 18 mM below surrounding values of about 563 mM occurs at 514 mbsf. Flow is required to sustain these anomalies, which would otherwise diminish by diffusion. The anomaly at 514 mbsf lies at a strong seismic reflector that most likely represents a sand along which pore fluid may have flowed (there was only poor core recovery from the interval of the anomaly, which lies in the unlogged section of the site).

Overall, organic carbon in the section is at a low concentration (0.2–0.4 wt%) and is refractory. Concentrations of methane above 200 mbsf are less than 5 ppmv. Ethane, propane, and butane are present only in trace amounts (C_1/C_2 > 1000), indicating that the methane is of bacterial origin. An anomaly of high methane gas content (27,698 ppmv) occurs in a high-porosity sand at 351 mbsf. It is not clear that the methane in this sand was formed in situ, yet fluid migration appears to be excluded as an explanation by the absence of anomalies in the fluid chemistry. In this instance the gas possibly may have migrated independently into the sand.

In summary, investigations at Site 888 revealed that the upper quarter of the sedimentary section on the ocean floor off Vancouver Island comprises a sequence of undercompacted sands and clayey silts that were rapidly deposited in a submarine fan, or in proximity to it. The rate of sedimentation of the upper 100 m of section has been close to 1 m/1000 yr, and sedimentation rates in the remainder of the cored interval have at least matched that rate, and were probably greater, judging from the character of sediments in Unit II (middle fan subassociation). In as many as four intervals of the cored section, there is evidence that fluid flow is occurring. It appears probable that much of this flow arises from differential compaction within the fan translating to horizontal flow, because of the heterogeneity of fan sediments, but the possibility that some of the flow has been transmitted horizontally from a region of compaction induced by the advancing accretionary wedge, 7 km distant, cannot be excluded.

BACKGROUND AND OBJECTIVES

Drilling at Ocean Drilling Program (ODP) Site 888 penetrated a portion of the sedimentary section in Cascadia Basin. This sequence is as yet unaffected by the accretionary tectonics that deform the eastern margin of Cascadia Basin along the Juan de Fuca/North American plate boundary. Site 888 provides a reference section for comparison with sites in the accretionary wedge on the continental margin. Site 888 lies 7 km west of the base of the continental slope, the topographic manifestation of the toe of the wedge (Fig. 1). This position places it lies at a distance from the accretionary wedge that is greater than the spacing of the imbricate thrusts, leaving it nearly isolated from the tectonic stresses that deform and consolidate the sediments within the wedge and in the proto-deformation zone seaward of the wedge toe.

The base of the continental slope, as imaged by sidescan sonar (Davis et al., 1987) is a complicated, lobate front formed from seaward-verging thrust sheets (Davis and Hyndman, 1989; Hyndman et al., 1990), which are cut by small submarine canyons and slump scars and associated deposits. The basin sediments consist of turbidites and interbedded hemipelagic deposits, which dip very shallowly to the west at the surface, although much of the column dips eastwardly as oceanic basement subsides toward the margin. Nitinat Fan is the dominant depositional feature in the northern Cascadia Basin, fed by turbidity currents moving down the Juan de Fuca and Nitinat canyons. Site 888 has probably received much of its sediment from this system, but it may also have received turbidite deposition derived from smaller canyons east and north of its present position as well. The drill site is located at the western edge of a small apron of sediment that extends from the base of the continental slope and probably reflects local deposition near canyon mouths.

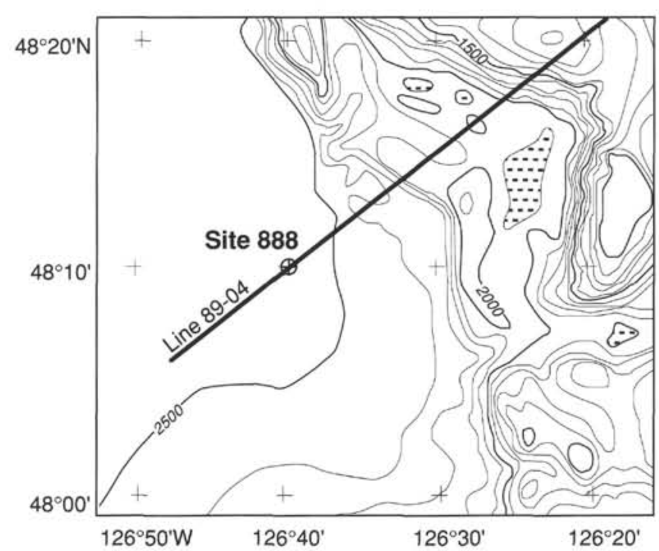

Figure 1. Location of Site 888 relative to the base of the continental slope, which is separated from Cascadia Basin by the marked increase in slope between about 2500 and 2100 m. The northern flank of Nitinat Fan lies just south of Site 888. Contour interval: 100 m. Horizontal dashed lines indicate bathymetric lows. Track of seismic line 89-04 is indicated.

The objectives of drilling Site 888 were to delineate the chemical, thermal, physical, lithologic, chronostratigraphic, and hydrologic characteristics of an undeformed sedimentary section in Cascadia Basin, near the toe of the accretionary wedge. Although the basic stratigraphy of Cascadia Basin was described at Site 174 (of Deep Sea Drilling Project (DSDP) Leg 18), that section was located on a distal portion of Astoria Fan off Oregon; it was not logged, and many of the geochemical (particularly the isotopic) determinations necessary to understand the evolution of the pore fluids were not made. Operations at Site 888 were designed to remedy those deficiencies and included a comprehensive program of in-situ measurements and core analyses to define the inorganic and organic chemistry of fluids and solids, the resident bacterial mass and its activity, as well as the thermal gradient, lithologic composition, biostratigraphy, magnetostratigraphy, and physical properties of the sediment column.

SEISMIC STRATIGRAPHY

Site 888 is situated about 100 m southeast of shotpoint 343 of multichannel seismic line 89-04, near its southwestern end (Fig. 2). The line is from a survey acquired for the Pacific Geoscience Centre of the Geological Survey of Canada by Digicon Geophysical Corp. in September 1989 (Spence et al., 1991). It is flanked by line 89-05 to the northwest and line 89-03 to the southeast, from the same survey, and by line LP85-01 to the southeast, from a survey run for the Pacific Geoscience Center in May 1985 by Geophysical Service Inc. as part of the Lithoprobe project (Yorath et al., 1987; Hyndman et al., 1990). The site lies near the southwestern border of a grid of single-channel seismic-reflection lines run in 1987. Line 16 is the closest of these lines to the site (Fig. 3).

Site 888 lies 7 km seaward of the outermost of three thrust anticlines that form the frontal part of the accretionary wedge, and incorporate nearly the whole thickness of the sedimentary section (Fig. 4). At the site, the thickness of the sedimentary column is 2500 m, equivalent to 2.0 s two-way traveltime (TWT) (Fig. 5). Sediment thickness decreases westward, and it increases eastward up to the toe of the accretionary wedge. This change in thickness is predominantly a response of sedimentation to the subsidence of the cooling oceanic lithosphere; approaching the margin, however, further subsidence has been produced by the lithosphere beginning to subduct beneath North America. The section below a depth of about 1 km (1.0 s TWT) is generally well bedded. The reflectors show extensive lateral continuity, and many closely spaced reflectors can be observed. The intervals are of uniform thickness or thicken gradually and consistently to the east. An exception is the interval between 4.8 and 4.9 s TWT, which shows considerable disturbance. This may be an effect of extensive channel development or possibly deformation associated with catastrophic fluid escape during the early stages of sediment compaction. The sections immediately above and below this interval are unaffected. Between 4.5 s TWT and the seabed, the reflectors show considerable variation, many lacking extensive lateral continuity and exhibiting terminations. The intervals between them thicken both westward and eastward and are locally irregular. The style of this sequence of reflectors is characteristic of the lower to mid-fan regions of a submarine fan.

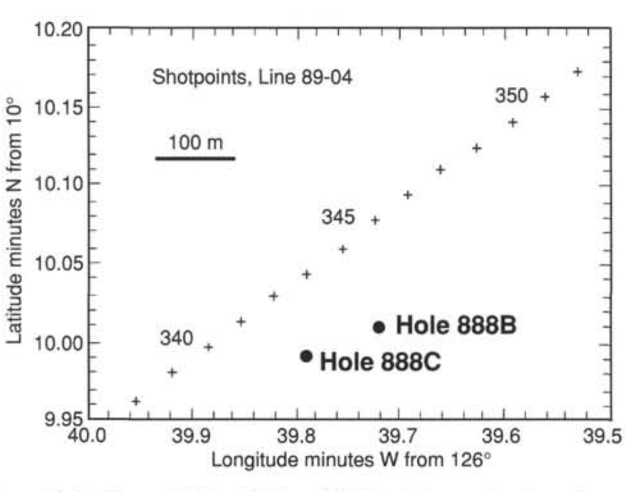

Figure 2. Positions of Holes 888B and 888C relative to the shotpoints on seismic line 89-04.

In the vicinity of the site, there are several channels in the interval 3.6–3.9 s TWT. The hole penetrates one at 3.63 s TWT and the edge of another at 3.68 s TWT (Fig. 6). Between 3.56 and 3.62 s TWT, there is a sequence that thickens to the west. Its top surface shows the erosional truncation of reflectors and is overlain by a sequence of strongly layered reflectors that dip eastward and are themselves truncated by a horizontal reflector at 3.5 s TWT. The westward-thickening unit has the appearance of a fan lobe. The interval between 3.83 and 3.92 s TWT has a highly disturbed internal structure. Although this may be result of the vigorous development of channels, it appears that the interval may have undergone synsedimentary deformation, possibly caused by catastrophic dewatering. The interval between 4.13 and 4.20 s TWT shows an eastward-prograding sequence of inclined beds.

Many of the reflectors penetrated at Site 888 are laterally impersistent, but those at 3.53, 3.7, 3.73, 3.80, 3.83, and 3.97 s TWT extend to the accretionary wedge. During the period of time that it took for the sediments at Site 888 to be deposited, which is less than 780,000 yr (see "Paleomagnetism" section, this chapter), the position of the site traversed much of the region occupied by the Nitinat Fan, if the fan was in the same relative position to the continental margin that it occupies now. The distance moved by the site relative to the foot of the margin (toe of the accretionary wedge) could have been 41 km (assuming an age of 780,000 yr, during which 32.4 km of plate motion and 8.3 km of outbuilding of the toe of the accretionary wedge occurred (see Westbrook, this volume). At 0.78 Ma, the site would have lain just west of the central part of mid-fan (just to the southwest of a northwestward-trending fan lobe), if the form of the fan was as it is now. The northeasterly sense of progradation in the intervals immediately beneath the holes (4.05–4.20 s TWT), however, indicates that at the time of their deposition, the site already lay to the north and/or east of major depositional components of the fan. The deeper, and more northeasterly, part of the section should contain horizons formed when the site was southwest of the fan, but little evidence of the proximity of the fan is present in the section beneath 4.5 s TWT. There is a northeastwardly thickening unit at about 4.1 s TWT, and a suggestion of southwestward progradation in the unit just beneath 4.4 s TWT, between Shotpoints 370 and 410. In general, however, it seems that the Nitinat Fan did not exist in the region intersected by the section before the deposition of beds lying deeper than 4.5 s TWT, which may be about the Pliocene/Pleistocene boundary, and that in mid-Pleistocene times the fan lay south of its present position. These ages probably err on the side of being too old.

The deeper part of the section shows reflectors that are far more regularly and finely spaced than in the upper section. They show greater lateral continuity and few have high amplitude. The only reflector with an amplitude comparable with those in the upper section lies at 4.7 s TWT. The character of these reflectors and comparison with reflectors in the lower sequence drilled at Site 174 (Shipboard Scientific Party, 1973) indicate that they are predominantly fine-grained distal turbidites. It is probable that pelagic or hemipelagic deposits form only a minor component of the sequence. The oceanic magnetic anomaly sequence (Riddihough, 1977) places the age of the underlying lithosphere, and hence the oldest sediment, at about 6 Ma.

OPERATIONS

Leg 146 began at 1730 hr Universal Time Coordinated (UTC), 20 September 1992, with the first mooring line at Ogden Point Docks, Victoria, British Columbia, Canada. The vessel departed Victoria at

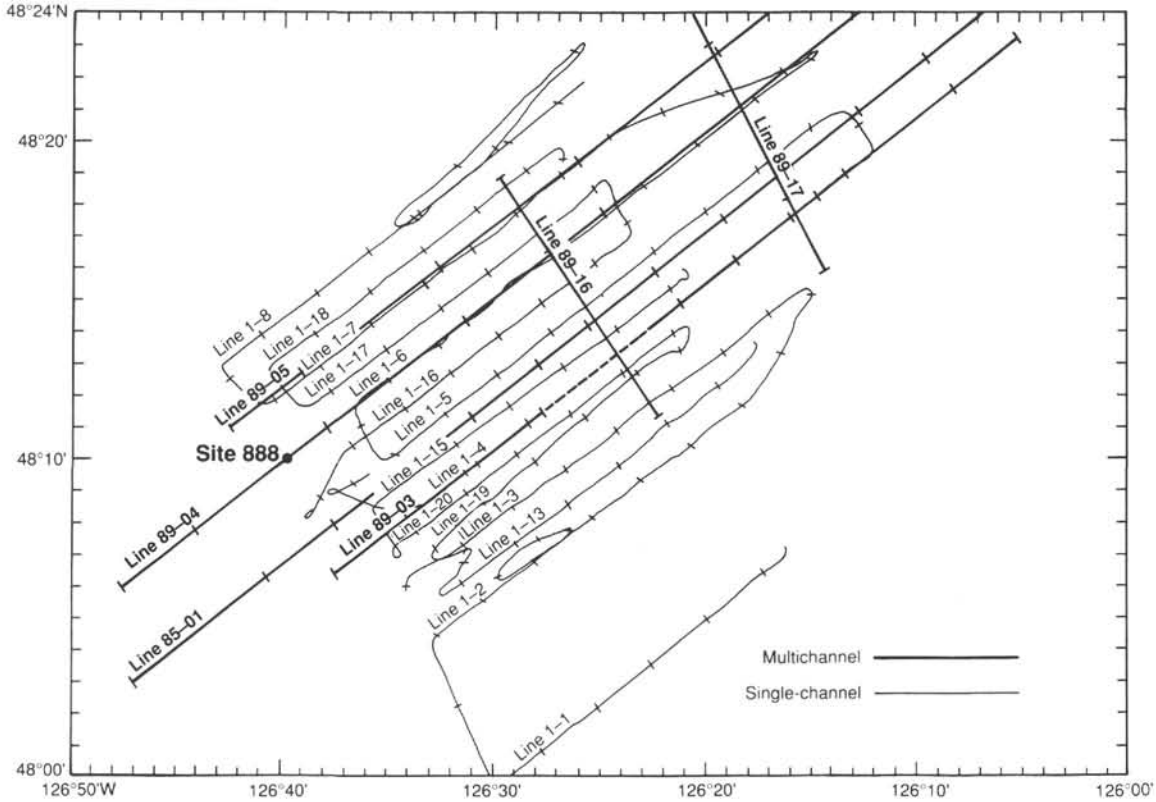

Figure 3. Multichannel and single-channel seismic-reflection lines in the vicinity of Site 888.

1600 UTC, 25 September. Despite opposing winds that held the ship's speed to about 10.5 kt, only 13 hr were required to transit the Straits of Juan de Fuca and reach the Vancouver Island Margin operating area. No seismic profiling was performed; the vessel was navigated to the geographic coordinates of the first site before thrusters and hydrophones were lowered and final positioning was achieved in dynamic positioning (DP) mode. A positioning beacon was launched at proposed Site VI-1 at 0800 UTC, 26 September.

Site 888(VI-1)—Cascadia Basin

Hole 888A

Hole 888A was spudded with an advanced piston corer (APC) core at 1600 UTC, 26 September. Because of sample requests that required the dedication of a large proportion of the first core as whole-round samples, the operating plan called for dual APC mud-line cores at Site 888. The first core (Table 1) was "shot" from 2516 m below sea level (mbsl).

Hole 888B

The bit was raised 4 m above the previous core depth and the second APC core was attempted. The recovered core was almost exactly 4 m shorter than Core 146-888A-1H, confirming that the bit had been placed just at the seafloor for the core in Hole 888A and that seafloor depth was 2516 mbsl.

Coring with the APC then continued, with magnetic orientation and temperature shoe measurements beginning with Core 146-888B-3H. Runs of the water-sampling temperature probe (WSTP) were made following Cores 146-888B-5H, -8H, -11H, -12H, and -17H. Core 146-888B-12H, in sand, gave an indication of incomplete stroke. Full-stroke indication returned for Cores 146-888B-13H through -17H; temperature shoes were discontinued after Core 146-888B-11H owing to overpull in excess of 60,000 lb. Overpull exceeded 110,000 lb on Core 146-888B-17H (to 151 mbsf) and APC refusal was indicated.

Three extended core barrel (XCB) cores then were taken with fairly good recovery as clay gave way to sand with depth. Three further XCB cores followed with only a few centimeters of recovery; a WSTP run also was unsuccessful in the soft sand.

The coring mode was changed back to APC in an attempt to recover the loose sand. Coring with the APC continued in the advance-by-recovery mode with consistent incomplete-stroke indications. The core barrels recovered a considerable amount of sand, but much of it was flow-in material resulting from the "hypodermic" action of APC withdrawal. Two WSTP attempts were unsuccessful in obtaining water samples or valid temperature data, but an APC shoe recorded good temperature data on Core 146-888B-33H at 292 mbsf. Core 146-888B-37H became stuck at the outer core barrel. Two XCB cores followed, recovering a total of 90 cm of core, so the APC again was deployed.

Coring with the XCB then continued in alternating clay and sand units, with fairly good coring results in clay but little or no recovery in sand. One additional WSTP probe run was attempted at 405 mbsf, but it was unsuccessful in sand. The clays and silts became increasingly indurated with depth and induced various mechanical failures of the XCB system.

Vessel heave to 3 m and rolls to 10° on 29 and 30 September reached the operational limits of the rig and a shutdown was narrowly avoided.

Low recovery in unconsolidated sand prompted a trial run of the vibrapercussive corer (VPC) at 452 mbsf. The attempt was unsuccessful because circulation could not be established through the corer to actuate the hydraulic hammer. At 514 mbsf, the pressure core sampler (PCS) was deployed. The PCS became stuck at the bit and its ball valve remained open, so that pressure was not held.

Coring operations were terminated at 567 mbsf with Core 146-888B-65X. Most of the scientific objectives had been realized and the operations schedule allowed no more time to be spent in reaching the original 600-m penetration objective.

Table 1. Coring summary, Site 888.

Core no.	Date (1992)	Time (UTC)	Depth (mbsf)	Cored (m)	Recovered (m)	Recovery (%)
146-888A-						
1H	Sept. 26	1620	0.0–9.5	9.5	9.75	102.0
Coring totals				9.5	9.75	102.0
146-888B-						
1H	Sept. 26	1705	0.0–5.5	5.5	5.39	98.0
2H	Sept. 26	1805	5.5–15.0	9.5	9.64	101.0
3H	Sept. 26	1930	15.0–24.5	9.5	10.28	108.2
4H	Sept. 26	2040	24.5–34.0	9.5	10.28	108.2
5H	Sept. 26	2200	34.0–43.5	9.5	10.05	105.8
6H	Sept. 27	0140	43.5–53.0	9.5	9.98	105.0
7H	Sept. 27	0245	53.0–62.5	9.5	10.14	106.7
8H	Sept. 27	0340	62.5–72.0	9.5	9.19	96.7
9H	Sept. 27	0630	72.0–81.5	9.5	9.52	100.0
10H	Sept. 27	0750	81.5–91.0	9.5	10.01	105.3
11H	Sept. 27	0920	91.0–100.5	9.5	10.04	105.7
12H	Sept. 27	1150	100.5–108.6	8.1	8.13	100.0
13H	Sept. 27	1305	108.6–118.1	9.5	9.92	104.0
14H	Sept. 27	1350	118.1–127.6	9.5	9.77	103.0
15H	Sept. 27	1625	127.6–137.1	9.5	10.04	105.7
16H	Sept. 27	1750	137.1–146.6	9.5	9.85	103.0
17H	Sept. 27	1830	146.6–156.1	9.5	9.17	96.5
18X	Sept. 27	2130	156.1–165.6	9.5	6.35	66.8
19X	Sept. 27	2220	165.6–175.1	9.5	6.39	67.2
20X	Sept. 27	2310	175.1–184.6	9.5	0.94	9.9
21X	Sept. 28	0240	184.6–194.1	9.5	0.50	5.3
22X	Sept. 28	0525	194.1–203.6	9.5	0.13	1.4
23X	Sept. 28	0655	203.6–212.9	9.3	0.00	0.0
24H	Sept. 28	0750	212.9–217.4	4.5	4.56	101.0
25H	Sept. 28	0840	217.4–226.9	9.5	9.10	95.8
26H	Sept. 28	0930	226.9–234.2	7.3	7.23	99.0
27H	Sept. 28	1235	234.2–243.3	9.1	9.17	101.0
28H	Sept. 28	1315	243.3–251.8	8.5	8.47	99.6
29H	Sept. 28	1400	251.8–260.8	9.0	9.32	103.0
30H	Sept. 28	1440	260.8–267.8	7.0	6.93	99.0
31H	Sept. 28	1710	267.8–276.8	9.0	9.05	100.0
32H	Sept. 28	1750	276.8–282.8	6.0	5.89	98.1
33H	Sept. 28	1840	282.8–292.3	9.5	9.69	102.0
34H	Sept. 28	2030	292.3–300.5	8.2	8.18	99.7
35H	Sept. 28	2145	300.5–310.0	9.5	10.64	112.0
36H	Sept. 28	2250	310.0–319.5	9.5	9.79	103.0
37H	Sept. 29	0635	319.5–329.0	9.5	10.17	107.0
38X	Sept. 29	0850	329.0–338.5	9.5	0.90	9.5
39X	Sept. 29	0950	338.5–348.0	9.5	0.00	0.0
40H	Sept. 29	1235	348.0–357.0	9.0	9.07	101.0
41X	Sept. 29	1415	357.0–366.5	9.5	0.94	9.9
42X	Sept. 29	1555	366.5–376.0	9.5	0.74	7.8
43X	Sept. 29	1740	376.0–385.5	9.5	0.03	0.3
44X	Sept. 29	1935	385.5–395.0	9.5	8.23	86.6
45X	Sept. 29	2125	395.0–404.5	9.5	3.65	38.4
46X	Sept. 30	0120	404.5–414.0	9.5	0.00	0.0
47X	Sept. 30	0245	414.0–423.5	9.5	0.07	0.7
48X	Sept. 30	0430	423.5–433.0	9.5	0.28	3.0
49X	Sept. 30	0555	433.0–442.5	9.5	0.00	0.0
50X	Sept. 30	0740	442.5–452.0	9.5	0.27	2.8
51V	Sept. 30	1000	452.0–452.1	0.1	0.10	100.0
52X	Sept. 30	1125	452.1–460.5	8.4	0.35	4.2
53X	Sept. 30	1250	460.5–469.4	8.9	0.64	7.2
54X	Sept. 30	1435	469.4–478.4	9.0	2.11	23.4
55X	Sept. 30	1620	478.4–487.3	8.9	0.28	3.1
56X	Sept. 30	1810	487.3–496.2	8.9	0.84	9.4
57X	Sept. 30	2055	496.2–505.1	8.9	5.12	57.5
58X	Sept. 30	2255	505.1–514.0	8.9	5.63	63.2
59P	Oct. 1	0125	514.0–515.0	1.0	0.48	48.0
60X	Oct. 1	0420	515.0–522.8	7.8	0.78	10.0
61X	Oct. 1	0615	522.8–531.7	8.9	4.08	45.8
62X	Oct. 1	0815	531.7–540.4	8.7	4.44	51.0
63X	Oct. 1	1025	540.4–549.2	8.8	6.23	70.8
64X	Oct. 1	1225	549.2–558.1	8.9	7.45	83.7
65X	Oct. 1	1520	558.1–566.9	8.8	8.24	93.6
Coring totals				566.9	364.85	64.4

A wiper trip then was made to 73 mbsf in preparation for logging operations. When the drill string was again lowered to within 22 m of total depth, it began "taking weight." The string was raised immediately and the pump was started. At that point, the pipe was found to be firmly stuck. Attempts to back the string off failed; severing charges were detonated at 367 mbsf (above a likely bridging zone) and 187 mbsf (near the top of the sand section). The string finally came free after two stands of pipe had been pulled, indicating that the top of the sticking zone had been at about 130 mbsf.

When the pipe had been freed, the upper portion of the hole was filled with weighted drilling mud.

Hole 888C

Hole 888C was drilled to provide a dedicated hole for logging. The drill ship was offset about 73 m southwest of Hole 888B during the pipe trip. Hole 888C was spudded with a tri-cone drill bit at 1315 UTC on 3 October and was drilled to 600 mbsf with interruptions only for mud sweeps at 200 and 400 mbsf. After a 50-bbl mud sweep at total depth, two wireline runs were made to release the bit and to downshift the mechanical bit release (MBR) sleeve. The end of the pipe then was pulled to 102 mbsf for logging.

To minimize mechanical disruption of the borehole and/or degradation of the hole wall with time, logging commenced immediately without a wiper trip or rigging of the side-entry sub. Tests had shown only minimal clay instability in seawater, so the hole was not filled with fluid that would inhibit clay swelling.

The first logging run was with the heavy geophysical tool string. The tool reached 513 mbsf before coming to rest on a bridge (or fill) in the hole. The log was recorded up to 73 mbsf, as the drill string was raised ahead of the logging tool by one stand as it ascended. As expected, the caliper log showed the hole wall to be irregular, with sand zones washed out and some clay intervals actually less than bit diameter. Little of the hole was enlarged beyond the range of the caliper, however, and log quality was good.

An initial run of the Schlumberger well seismic tool (WST) was unsuccessful because of obstructions in the hole and a power failure to the tool. The tool was recovered and the electronic equipment was found to be flooded.

Because of the difficulty in lowering the WST, the drill string was run back into the hole to clean the hole out while another WST was readied. The open-ended pipe was circulated to 358 mbsf where it met a solid obstruction. As the open-hole interval was too short to satisfy the VSP objectives and because the operation was falling behind schedule, logging operations were terminated.

Before recovery of the drill string began, the hole was filled with heavy drilling mud and plugged with cement. The bottom-hole assembly was recovered at 1245 UTC, 5 October, ending operations at Site 888.

LITHOSTRATIGRAPHY

Introduction

At Site 888 two holes were cored. One core was recovered in Hole 888A with 9.5 m penetration and 100% recovery. Hole 888B provided excellent recovery in the upper 156 m (down to Core 146-888B-17H) and in the interval 212–329 mbsf (Cores 146-888B-24H to -37H). Variable recovery was obtained in XCB cores from 156 to 212 mbsf and from 329 to 567 mbsf (Cores 146-888B-18X to -23X and 146-888B-38X to -65X, respectively).

Three lithostratigraphic units have been distinguished at Site 888 on the basis of the visual description of cores, smear slide and thin section analysis, grain-size analysis, and results of X-ray-diffraction (XRD) analysis.

Unit I consists of alternating clayey silt and very fine to fine sand beds. Sand beds make up 10%–20% of the sediment. A higher proportion of sand (40%–80%) occurs in Cores 146-888B-2H, 146-888B-7H through -9H, and 146-888B-12H and -13H. The thickness of the sand beds also increases in these intervals, where some exceptionally thick sand beds (up to 2 m) are found. In Core 146-888B-14H the percentage of sand is about 10% and gradually increases downhole to about 20% at the base of the unit. Thinner sand beds in this unit show parallel lamination and normally graded transitions to clayey silt above.

A transitional boundary between Units I and II is placed between 175.1 mbsf (Cores 146-888B-19X and -20X) and 193 mbsf (within

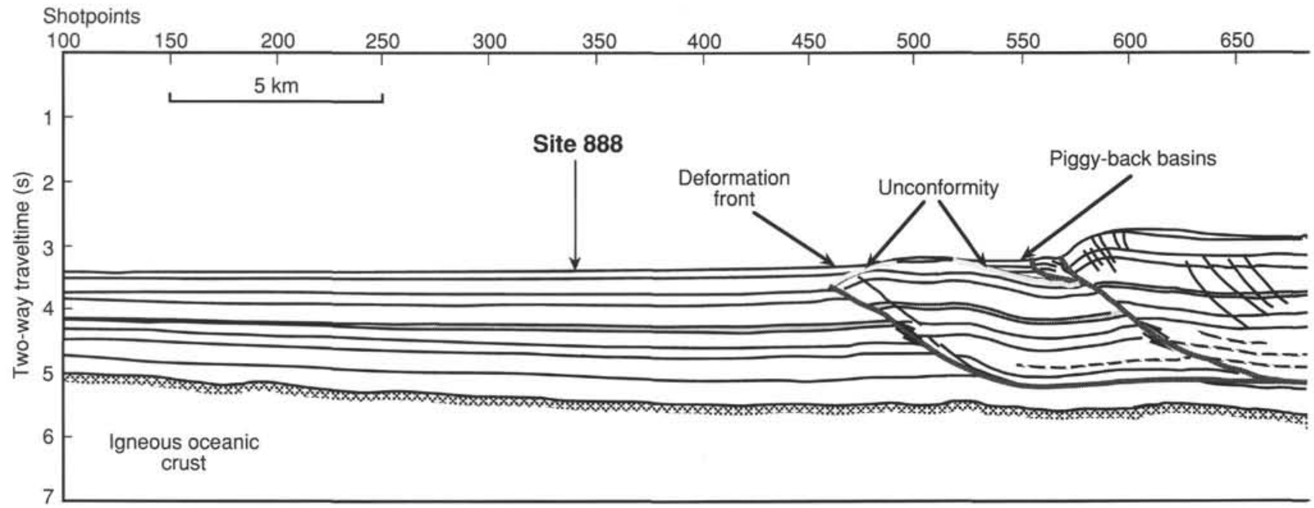

Figure 4. Interpretive line drawing of migrated seismic reflection section 89-04, on which Site 888 is situated. The first three thrust slices of the accretionary wedge are rooted in a décollement that lies only a little above the base of the incoming sediment sequence in the Cascadia basin. The wedge landward of these first three thrust slices appears to have been accreted above a shallower décollement, lying at a stratigraphic position close the base of the well-layered sequence in the first three thrust slices. The style of the older accreted section is one of shorter wavelength, more intensely deformed structures. This is overlain by a slope-cover sequence that is only mildly deformed.

Core 146-888B-21X). A gradual increase of massive sand is inferred from the progressive decrease of recovery and the dominance of sand in Cores 146-888B-24H through -29H. Results from natural gamma ray and caliper logs support this lithologic change (see "Downhole Logging" section, this chapter).

Unit II is composed of massive, thick (>1 m) beds of fine sand and clayey silt. The soupy drilling disturbance in the sand has wiped out any original sedimentary structures. Interbeds of clayey silt occur in some cores. In the upper part of Unit II (Core 146-888B-20X to -35H) intervals of several meters of silty sand occur, whereas the lower part of the unit is mainly composed of sand.

The boundary between Units II and III is placed at 452.1 mbsf, at the top of Core 146-888B-52X. Because recovery of core in this section of the hole was poor, this boundary was chosen where geochemical anomalies (e.g., an increase in pore-water chlorinity and organic carbon) and logging results suggest the presence of a physical-chemical discontinuity (see "Inorganic Geochemistry," "Organic Geochemistry," and "Downhole Logging" sections, this chapter). From the recovered cores, a gradual increase in the silty fraction of the sediment is observed beginning with Core 146-888B-52X and continuing to Core 146-888B-56X. In addition, the clayey silt recovered in Unit III is more compacted and in some intervals more brittle and fractured than in Units I and II.

Unit III has been divided into two subunits. Subunit IIIA is composed of faintly laminated firm clayey silt interbedded with thin (3–10 cm) to thick (30–100 cm) sand beds and isolated pebbles. The recovery of this subunit is extremely poor. The boundary between Subunits IIIA and IIIB is placed at the base of a layer of sand with pebbles, which lies upon a layer of clayey silt with sand at Section 146-888B-57X-1, 30 cm (496.5 mbsf). This boundary was chosen because of a significant increase in the recovery below this depth resulting from decreasing amounts of sand. Subunit IIIB is composed of faintly laminated, firm clayey silt interbedded with lesser amounts of thin to thick sand beds and isolated pebbles. In Unit III recovery was variable, and the sediment was heavily disturbed by the formation of drilling biscuits.

Lithostratigraphic Units

Unit I

Intervals: Core 146-888A-1H, and Cores 146-888B-1H through -19X
Depth: Hole 888A, 0–9.5 mbsf; Hole 888B, 0–175.1 mbsf
Age: late Pleistocene to Holocene

Lithostratigraphic Unit I consists of dark gray (N4 to 5YR 4/1), very dark gray (N3 to 2.5YR 4/1), and dark greenish gray (5Y 4/1) clayey silt interbedded with gray to dark greenish gray fine to medium siliciclastic sand.

In the upper two cores of the unit (from 0 to 15 mbsf) the color is dark olive gray (5Y 4/2) and about 30% of the components are biogenic (mostly diatoms [Fig. 7], and broken foraminifers, with some radiolarians and sponge spicules). There is a rapid decrease in the biogenic component with increasing depth in Unit I. Biogenic silica makes up 30% of some intervals in the top 15 m; below this level it rarely accounts for more than 3% of the sediment.

The grain composition of Unit I estimated from smear slides depends on the grain size of the material examined. The silt-size component contains feldspar, pyroxene, volcanic glass, rock fragments, hornblende, opaque minerals, and a diverse suite of other heavy minerals (notably zircon, tourmaline, and apatite). The rock fragments are generally larger than the other grains, and nearly opaque, which makes identification difficult. Identifiable rock fragments include plagioclase basalt and chert in subsidiary quantities. The suite of silt-sized material observed in the smear slides suggests that the dominant lithologies from which the silt is derived could be basalts, basaltic andesites, and/or andesites.

The clayey silt is homogeneous throughout almost all of Unit I, faintly parallel-laminated in a few intervals within Cores 146-888B-7H, -9H, -10H, and-14H, and typically lacks bioturbation.

Rock fragments, quartz, and feldspar are the major components of the siliciclastic sand, although heavy minerals occur in major proportions in many sands in Unit I (see the following). The rock fragments are mainly basic or intermediate volcanic rocks, with some coarser igneous rocks (granitoids) and chert occurring in lesser amounts. The feldspars are dominantly plagioclases of intermediate to basic composition, although many are altered. A small amount of altered potassium feldspar is thought to be present in the sands, although this has not been checked by staining techniques. A remarkable feature of the sand in Unit I is the proportion of "accessory" minerals, which commonly comprise up to 30% of the sediment. Hornblende is the most abundant of these minerals. The dominant variety of hornblende is relatively fresh and shows greenish brown to green–bluish green

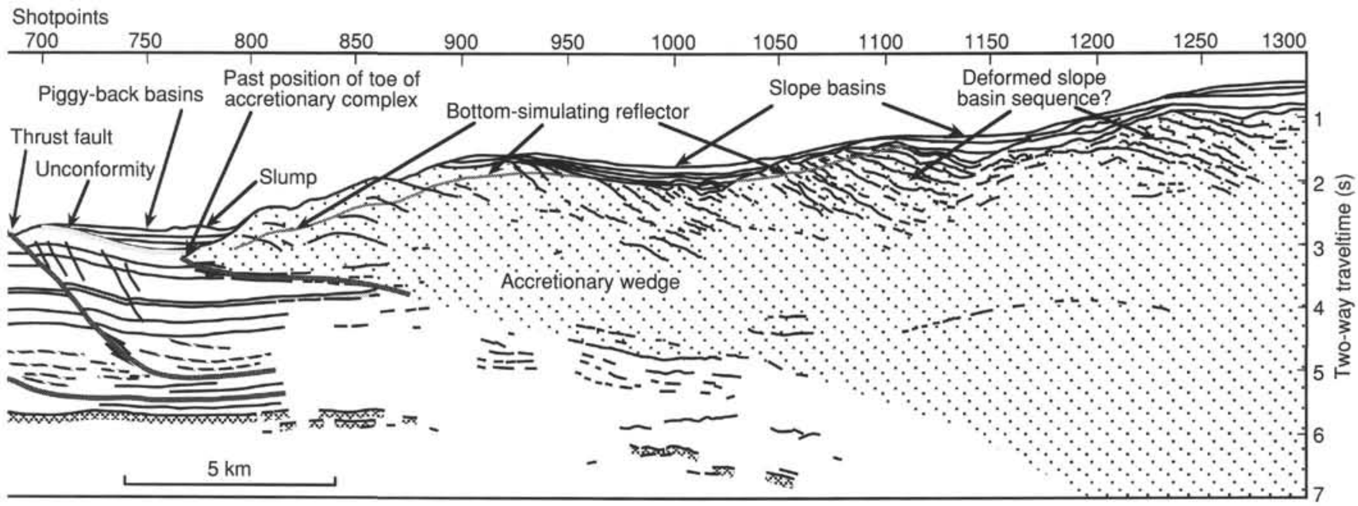

Figure 4 (continued).

pleochroism. Pyroxenes, both ortho- and clinopyroxene, are the second most abundant ferromagnesian mineral. Almost all of the pyroxenes are altered, at least in part. The other common heavy mineral is magnetite, occurring as discrete euhedral grains, abraded single grains, and granular aggregates. Magnetite grains can also be seen as inclusions in quartz. The abundance of magnetite is consistent with the relatively high magnetic susceptibility (average about 2×10^{-3} SI) and remanence (10–100 mA/m) observed in Unit I (see "Paleomagnetism" section, this chapter). Three main orthosilicates occur relatively abundantly in the heavy mineral fraction: zircon (Fig. 8), apatite, and tourmaline. Other constituents occurring in minor proportions are, in order of decreasing abundance, micas, volcanic glass, epidote, garnet, rutile, shell fragments, olivine, barite, and sulfides.

The siliciclastic sand occurs rhythmically, in beds varying in thickness from 1 cm to more than 100 cm. The bedding is mostly medium (10–30 cm), with some thin (3–10 cm; Cores 146-888B-14H, -17H, and -19X) and thick (30–100 cm; Cores 146-888B-13H and -15H) occurrences. The basal contact of the sand beds is usually sharp, commonly erosional, and sporadically scoured. Usually, the thickest sand beds (10 cm or more thick) are very dark gray in color, soupy, and well sorted (Fig. 9), range from fine to medium sand, and show fining-upward gradation and sharp upper contacts (Fig. 10). In contrast, the thinner sand beds (generally less than 10 cm thick) are dark gray, parallel laminated, less sorted, and finer grained. These also show transitional upper contacts, with upward gradation to clayey silt (Figs. 11–13).

Coarse sand and matrix-supported pebbly sand occur at the base of some sand beds in layers 30–50 cm thick (Sections 146-888B-3H-3 and -7H-3; Fig. 14). Some subrounded pebbles reach 3 cm across, but most are smaller than 1 cm. They are identified as lithic clasts, mainly of basic igneous rock, with rarer granitoids and schists. Subangular shell fragments (bivalves and echinoderm plates) 1–2 cm across occur in the pebbly layers. Isolated subrounded pebbles (rock fragments) are present in Core 146-888B-4H.

Very dark gray to black layers about 1 cm thick occur at the top of thin sand beds in Cores 146-888B-9H, -10H, -11H, and -13H. The dark color of these thin layers is probably caused by the presence of sulfides (most likely pyrite), and opaque minerals in greater proportion than in the adjacent sediments. It is also possible that the dark color is caused by finely divided manganese oxides or very fine organic matter.

Wood fragments and bioclasts in Unit I are small and largely restricted to the sand beds at the base of Unit I. The XRD data from the wood fragments are equivocal: pyrite, if present, is not in sufficient proportion or crystallized well enough to yield distinct reflection peaks.

Transition between Units I and II

Interval: Cores 146-888B-19X to -21X
Depth: 175.1–193 mbsf
Age: Pleistocene

A gradual increase of massive sand is inferred from the progressive decrease of recovery and the dominance of sand in what was recovered in this interval. Results from natural gamma ray and caliper logs suggest the transitional nature of the lithologic change (see "Downhole Logging" section, this chapter).

Unit II

Interval: Cores 146-888B-21X to -52X
Depth: 193–452.1 mbsf
Age: Pleistocene

Lithostratigraphic Unit II consists of dark gray (N4 to 5YR 4/1), very dark gray (N3 to 2.5YR 4/1) and dark greenish gray (5Y 4/1) very fine to medium siliciclastic sand and silty sand, with intervals of coarse sand and clayey silt.

The sand is composed mainly of quartz, feldspar, rock fragments, mica, and heavy minerals. The rock fragments are relatively less abundant than in the sand of Unit I, although again the proportion of lithics is greater in coarser sediment. The main lithic grains that were identified are altered igneous rocks (green in color and banded) and chert (of various colors and veined by quartz). These two components are relatively more abundant in Unit II than in Unit I. Pyroxene is less abundant than in Unit I, but the other principal ferromagnesian grains—amphiboles and micas—are particularly abundant. The amphiboles are mainly common hornblende of the same pleochroism as in Unit I, but actinolitic hornblende and glaucophane are also found in trace amounts.

The micas are particularly abundant in some intervals. In Cores 146-888B-24H to -31H, up to 10% mica, occurring as brown, green, and colorless varieties, is found in the smear slides. We think that this high incidence of mica is partly a sampling effect: the mica segregating to the top of the soupy sediment in the split half cores. Volcanic glass, which is green or brown and relatively fresh, occurs sporadically throughout Unit II. It is likely that some of the volcanic glass has been counted as mica, as it has a similar reflectivity and body color.

Opaque minerals—again, mainly magnetite, with some sulfides and possibly ilmenite and manganese oxides—are quite abundant (up to 10%) in the sands of Unit II. These constituents, along with the rock fragments and amphiboles, give the sands their very dark gray

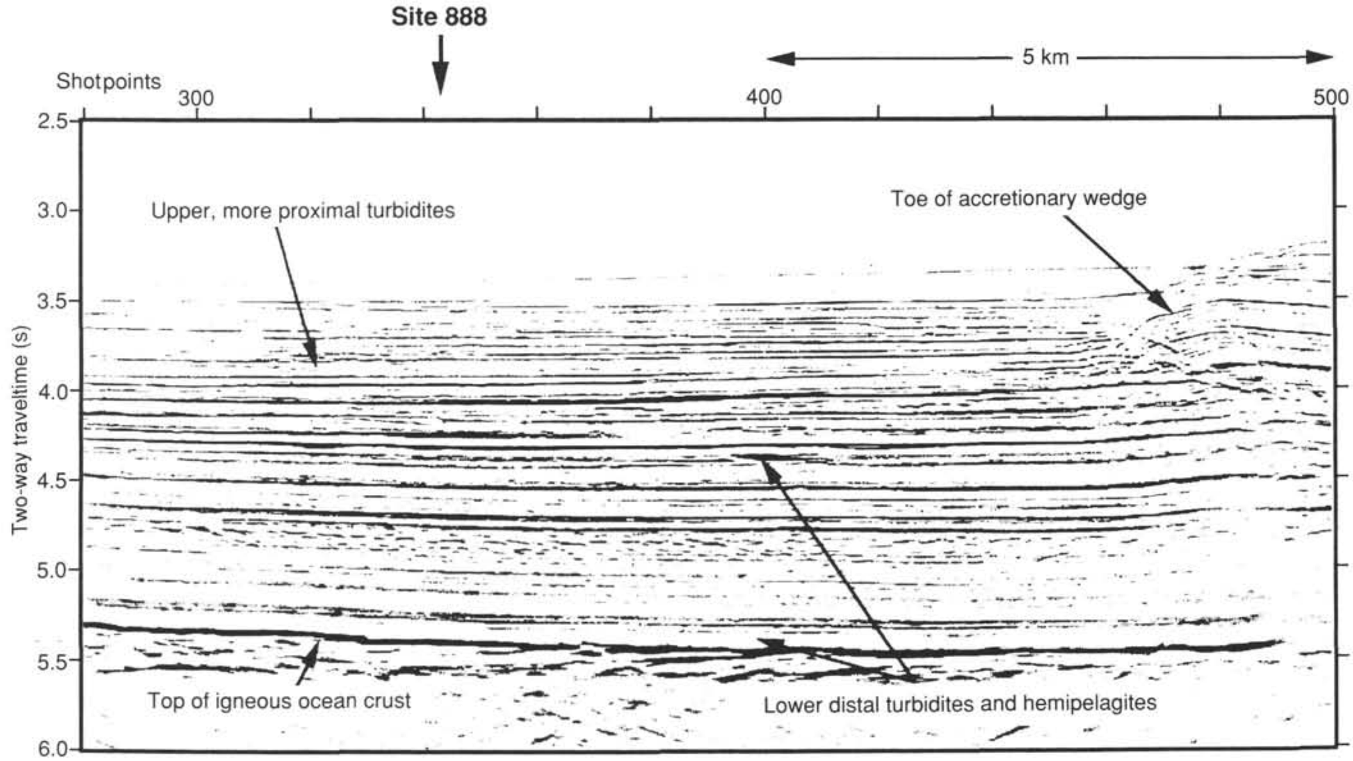

Figure 5. Part of seismic line 89-04 showing the region of the Cascadia abyssal plain, at the toe of the accretionary wedge in which Site 888 is situated. The section is migrated and is plotted in variable density form with positive grays and black, negative white.

color. Other accessory minerals in Unit II include, in decreasing proportion, tourmaline, epidote, zircon, apatite, rutile, chlorite, and garnet. Very sporadic staurolite, topaz, sillimanite, and kyanite were found. The lithostratigraphic significance of these heavy minerals (see Scheidegger et al., 1973) is limited: neither their relative proportion nor their incidence with depth was determined accurately from the smear slides. No minerals or mineral–lithic clast associations could be identified which characterized particular lithofacies or depth intervals.

Cores of lithostratigraphic Unit II are characterized by either extremely poor recovery (XCB cores) or by extremely heavy drilling disturbance (APC cores). The sand layers are on the order of tens of meters thick and are almost everywhere soupy (i.e., completely reworked during coring). Intense bubbling of the sand-size sediment as a result of gas expulsion, possibly causing additional disturbance, was noted during splitting of some sections of Core 146-888B-40H.

From Core 146-888B-40H downward small sand-grain clusters, which could be disaggregated by the addition of hydrochloric acid, were noted. However, such evidence of cementation was limited: most of the sand was completely incohesive.

No sedimentary structures can be identified except for a general upward-fining of grain size in each sand interval. The variable sorting by grain size recorded (from poorly sorted to well sorted) also probably depends upon drilling disturbance. Grain shape varies from subangular to subrounded in all size fractions, though there is a tendency (common in siliclastics generally) for larger grains to be better rounded. Clayey silt beds are less disturbed by drilling and often show faint parallel lamination. The lower and upper contacts between sand layers and silt are always sharp.

Two thick intervals of clayey silt interbedded with thin sand layers occur in Cores 146-888B-26H (226.9–233.2 mbsf) and 146-888B-44X and -45X (385.5–397.3 mbsf). In such intervals the sands grade upward to clayey silt, and the sedimentologic characteristics are similar to those of lithostratigraphic Unit I.

Rounded rock fragments (up to 2 cm diameter), mud clasts, and abraded shell fragments occur in Cores 146-888B-44X and -45X. Very dark gray to black layers about 1 cm thick are found in Core 146-888B-26H. Their composition resembles that of the thin layers found in lithostratigraphic Unit I. They probably reflect the presence of sulfides, magnesian oxides, and/or possibly organic matter. Wood fragments are present throughout the sand layers, and reach about 5 cm in size in Core 146-888B-28H.

Unit III

Interval: Cores 146-888B-52X to -65X
Depth: 452.1–566.9 mbsf
Age: Pleistocene

Lithostratigraphic Unit III consists of dark gray (N4) firm clayey silt with sand and pebbles. It has been divided into two subunits based on correlation with logging and geochemical data (see "Inorganic Geochemistry," "Organic Geochemistry," and "Downhole Logging" sections, this chapter).

Subunit IIIA

Interval: Core 146-888B-52X to Section 146-888B-57X-1, 30 cm
Depth: 452.1–496.5 mbsf
Age: Pleistocene

The sediment recovered in Subunit IIIA shows the first evidence of incipient lithification. Thin sand layers interbedded with the clayey, usually laminated, silt (Fig. 15) are partly indurated by the presence of weak carbonate cementation (reaction to HCl). Discrete crystals of carbonate (probably dolomite, which may have been detrital), although rare, were recorded in the sands of Subunit IIIA. Recovery of Subunit IIIA was extremely poor.

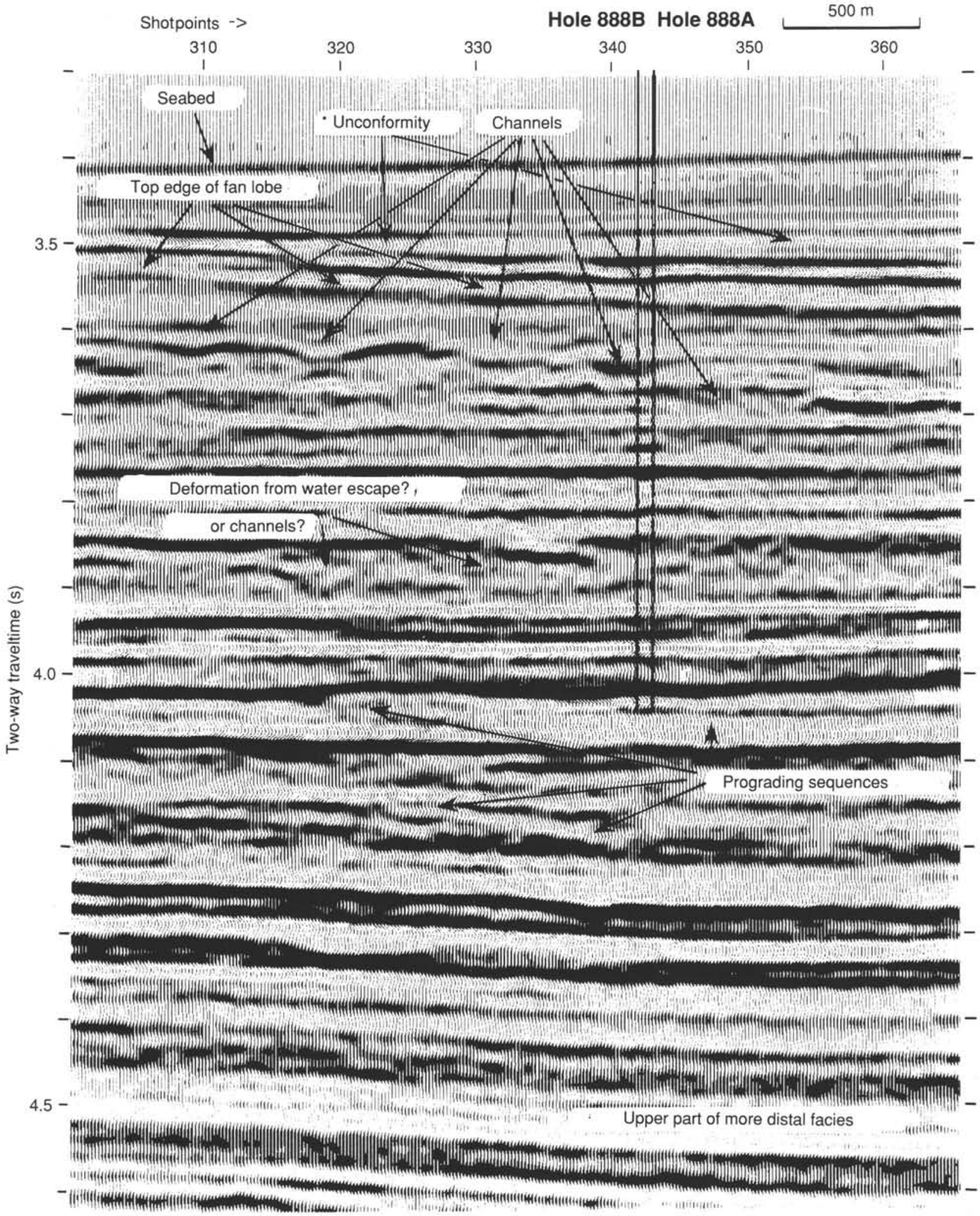

Figure 6. Seismic section 89-04 in the immediate vicinity of Site 888. The section is migrated, with the area under the positive-trending lobes filled. The drilled trace of Hole 888A is marked to show depth, changing to white or black every 100 m, with intermediate marks every 20 m.

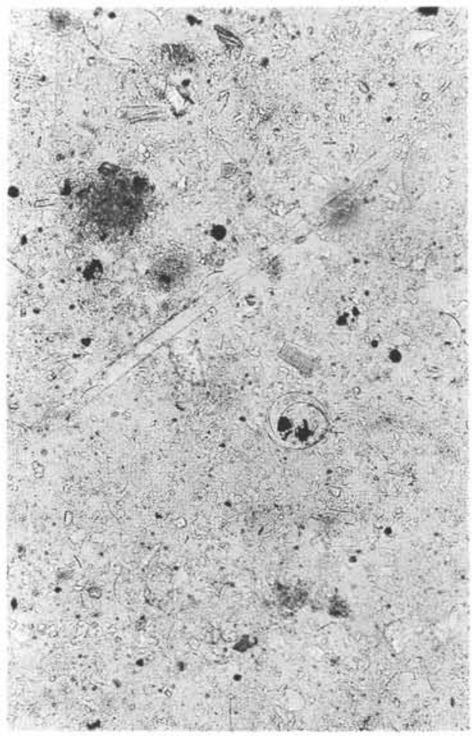

Figure 7. Clayey silt with diatoms in smear slide from Sample 146-888B-1H-2, 102 cm, in lithostratigraphic Unit I.

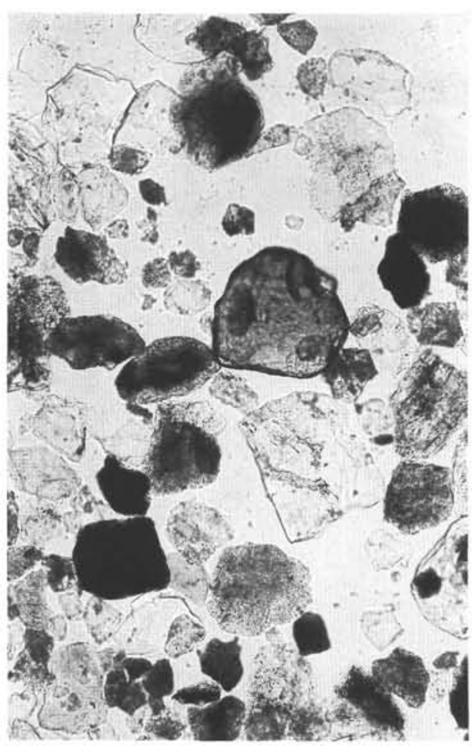

Figure 8. Medium- to fine-grained sand with conspicuous zircon in smear slide from Sample 146-888B-3H-4, 58 cm, in lithostratigraphic Unit I.

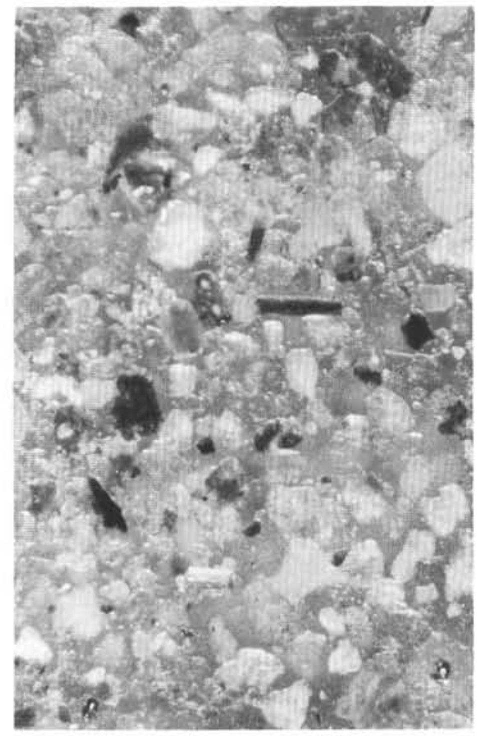

Figure 9. Subangular, well-sorted medium sand under binocular microscope in Sample 146-888B-13H-1, 65 cm, from lithostratigraphic Unit I.

Subunit IIIB

Interval: Section 146-888B-57X-1, 30 cm, to Core -65X
Depth: 496.5–566.9 mbsf
Age: Pleistocene

Lithostratigraphic Unit III is represented mainly by Subunit IIIB, which consists of dark gray (N4) firm clayey silt, with sand and pebbles.

The siliciclastic components of the silt and sand are similar to those in Units I and II. The finer lithologies are somewhat richer in quartz and feldspars: commonly these two minerals account for 40%–60% of the silts and silty sands. The smear slides contain quartz, feldspars, lithic fragments, and ferromagnesian minerals in major amounts. The same mica types and amphiboles were found in this interval as in Unit II, though in slightly lesser quantities. Volcanic glass was also found in small amounts throughout the recovered part of Unit III. The main accessory minerals—opaque minerals (largely magnetite), apatite, epidote, zircon, colorless garnet, and tourmaline—are the same as in the other two units. Trace amounts of glaucophane, rutile, and darker garnet were found. Up to 5% carbonate (probably dolomite) in the form of discrete rhomboidal grains was recorded in Sections 146-888B-58X-3, -62X-3, and -63X-1.

Rounded to subrounded pebbles were frequently found in Unit III (Figs. 16–17). Pebbles occur either as matrix-supported pebbly sand (Sections 146-888B-57X-3, -62X-CC, and -63-3) or as isolated clasts up to 3 cm in diameter (Sections 146-888B-58X-1, -60X-1, and -62X-1). The pebbles include granite, granodiorite, metaquartzite, and basalt.

Wood fragments (Section 146-888B-58X-3, 55–56 cm), pyrite micronodules, and bioclasts occur in the sand layers. Calcitic bioclasts, mostly echinoderm plates and broken foraminifers, were found sparsely throughout Subunit IIIB. Notably, diatomaceous silt was found in Section 146-888B-54X-1. Otherwise, biogenic silica is very rare.

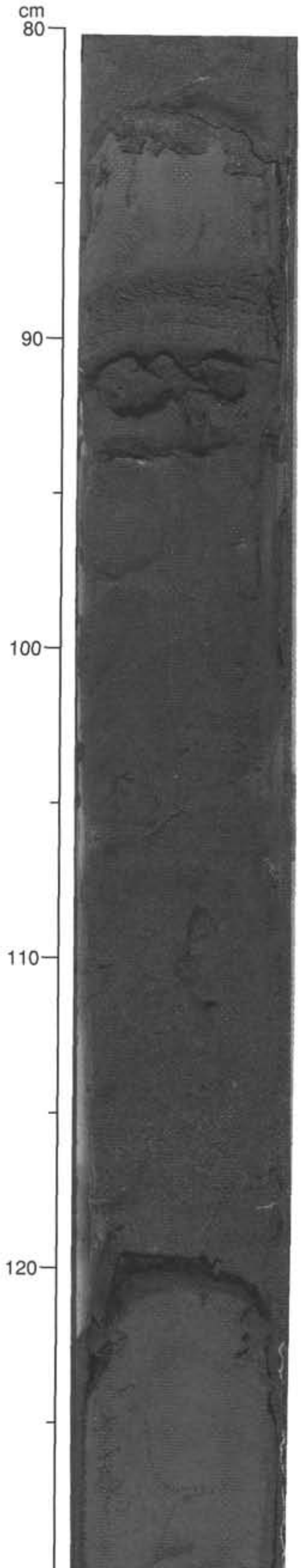

Figure 10. Example of the thicker dark gray turbidites in Section 146-888B-7H-5, 80–130 cm, from lithostratigraphic Unit I. Sharp upper and lower contacts are visible at 120 and 90.5 cm, respectively.

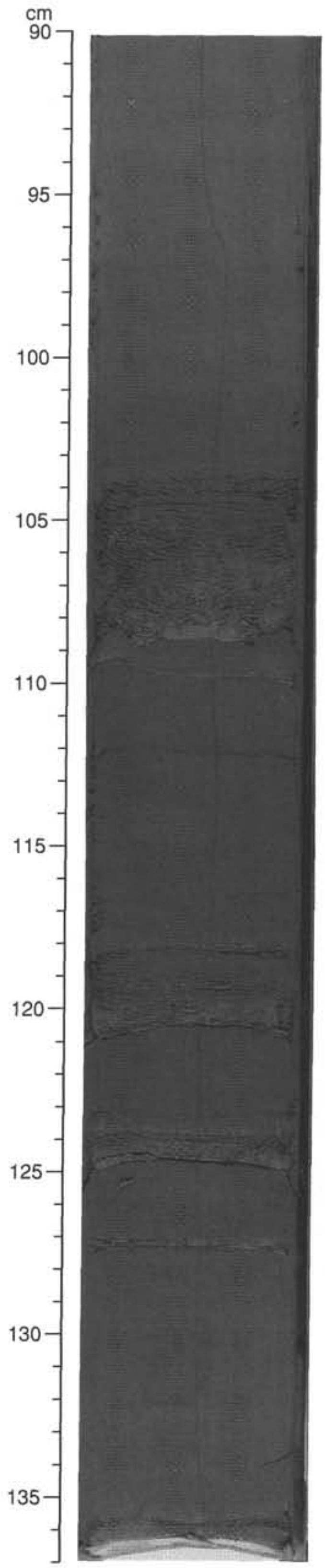

Figure 11. Example of thinner gray turbidites in Section 146-888B-18X-4, 90–137 cm, from lithostratigraphic Unit I. Note the sharp lower contact, transitional upper contact, and parallel lamination.

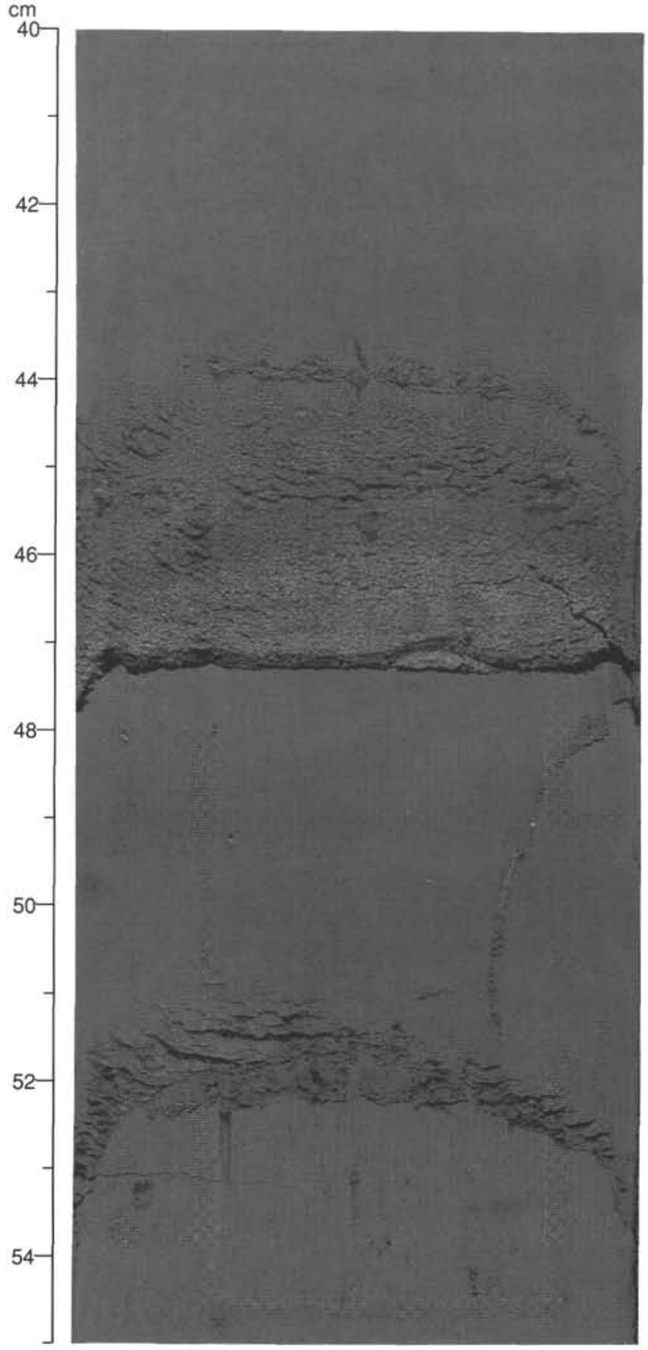

Figure 12. Detail of thinner gray turbidites in Section 146-888B-6H-6, 40–55 cm, from lithostratigraphic Unit I. Note the sharp lower contact, transitional upper contact, parallel lamination, and presence of a characteristic lighter colored layer at the base of the turbidite.

At a few intervals, sand layers of this subunit show incipient lithification by carbonate cement accompanied by the presence of minor amounts of gypsum. However, the gypsum is mostly a product of precipitation from the pore waters, along with halite, during slide preparation.

All cores from lithostratigraphic Unit III are heavily disturbed by the formation of drilling biscuits (Fig. 17). Cores are broken up into discrete 2- to 5-cm-thick biscuits, which are healed together by muddy drill-induced fluidization zones. Some of the biscuits are tilted or rotated on a horizontal axis through as much as 60°–90°. Nevertheless, some faint parallel lamination and mottling caused by bioturba-

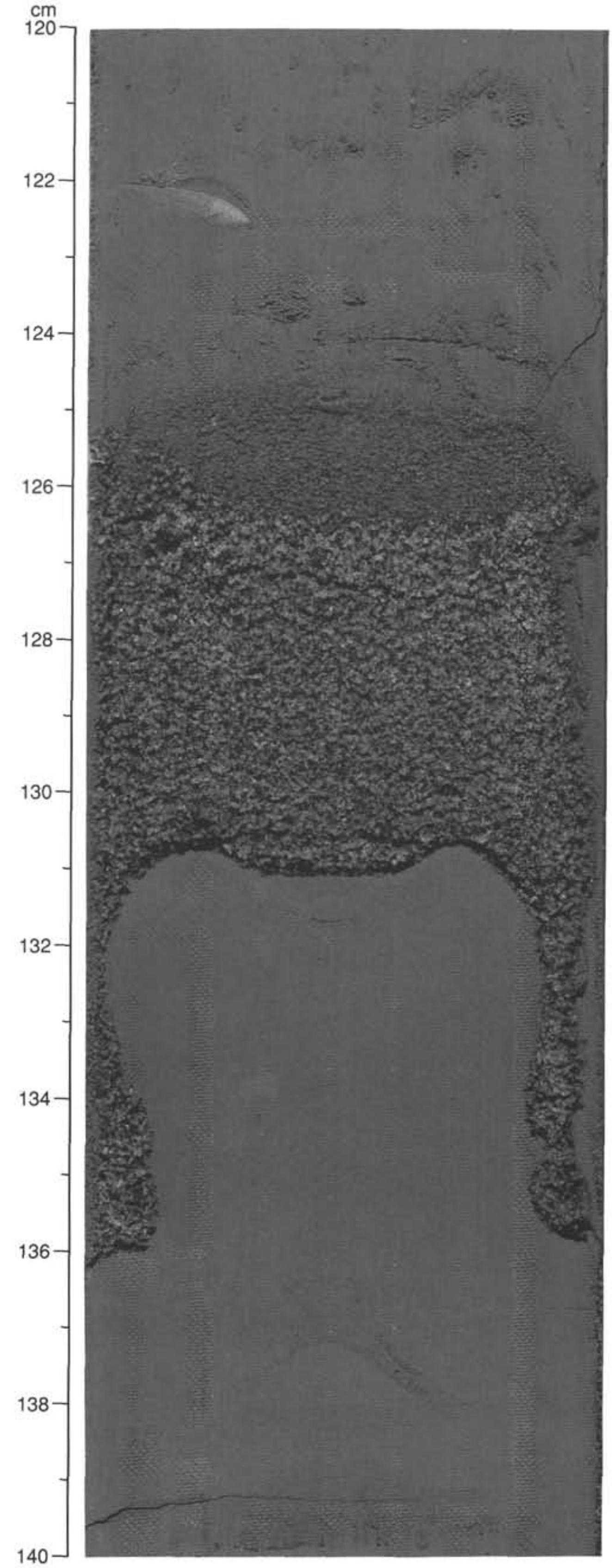

Figure 13. Dark gray turbidite (131.0–126.5 cm) truncated by a thin gray turbidite (126.5–125.0 cm) in Section 146-888B-7H-2, 120–140 cm, from lithostratigraphic Unit I.

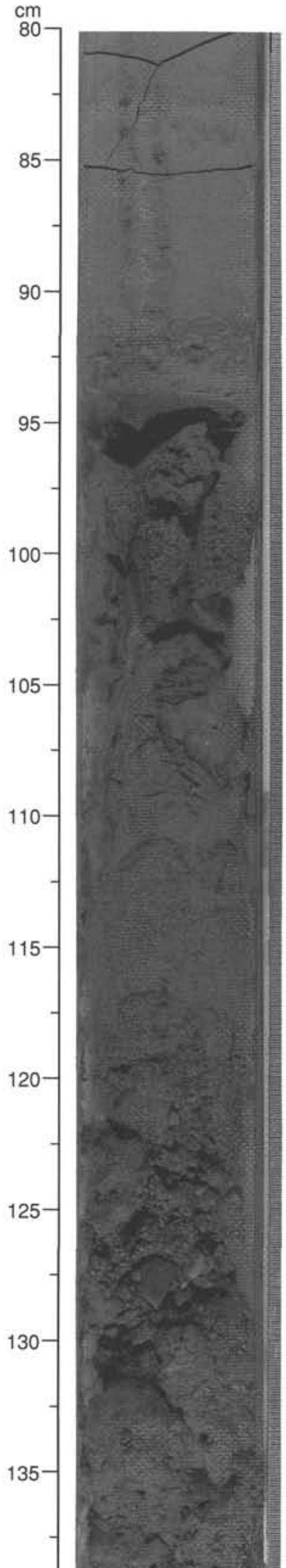

Figure 14. Subangular and subrounded clasts at the base of a dark gray turbidite in Section 146-888B-7H-3, from lithostratigraphic Unit I.

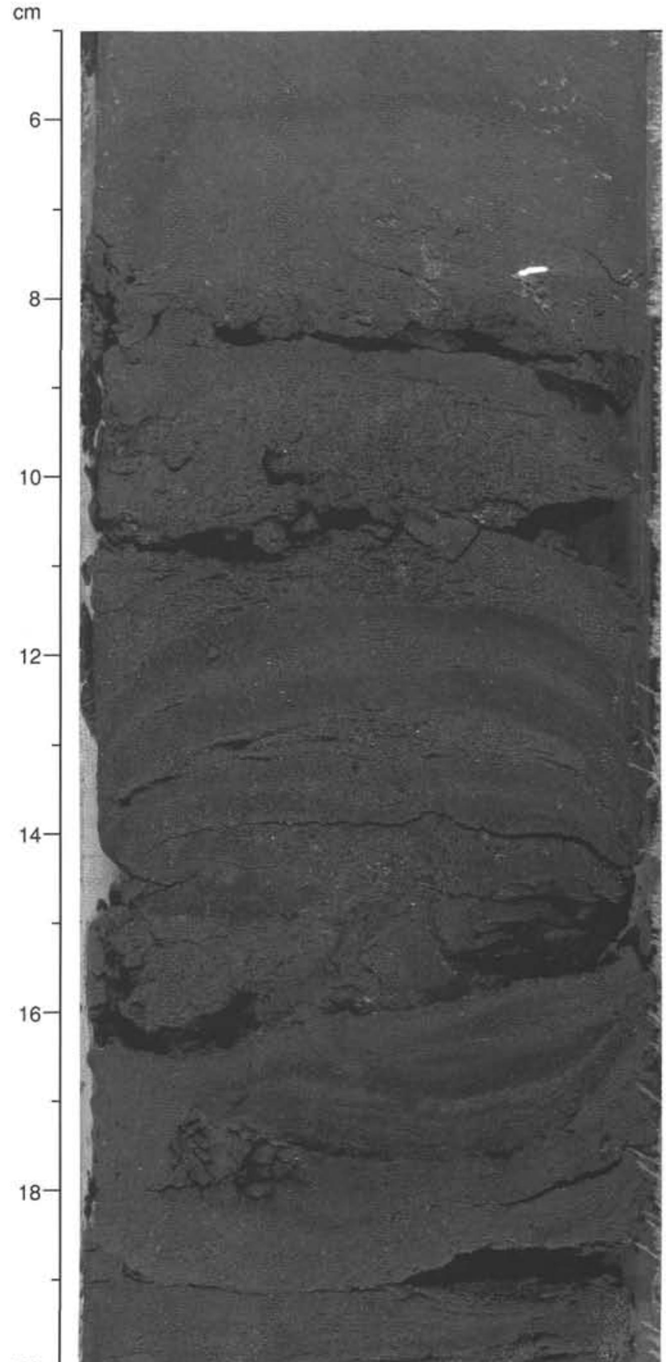

Figure 15. Fine parallel lamination in sand and clayey silt (Section 146-888B-56X-CC, 5–20 cm) from lithostratigraphic Subunit IIIA.

tion can be seen within individual biscuits, and gradational contacts between clayey silt and more sand-rich silt or sand are present. In some cases the sediment is homogenized by drilling.

Grain Size

Fifty-five samples of the clayey silt lithology from the three lithostratigraphic units were analyzed on board for grain-size distribution with the Lasentec LAB-TEC 100 device (Figs. 18–19; see also "Explanatory Notes" section, this volume).

The mean size of the fine sediments of the three lithostratigraphic units ranges between very fine silt and fine silt (and in exceptional

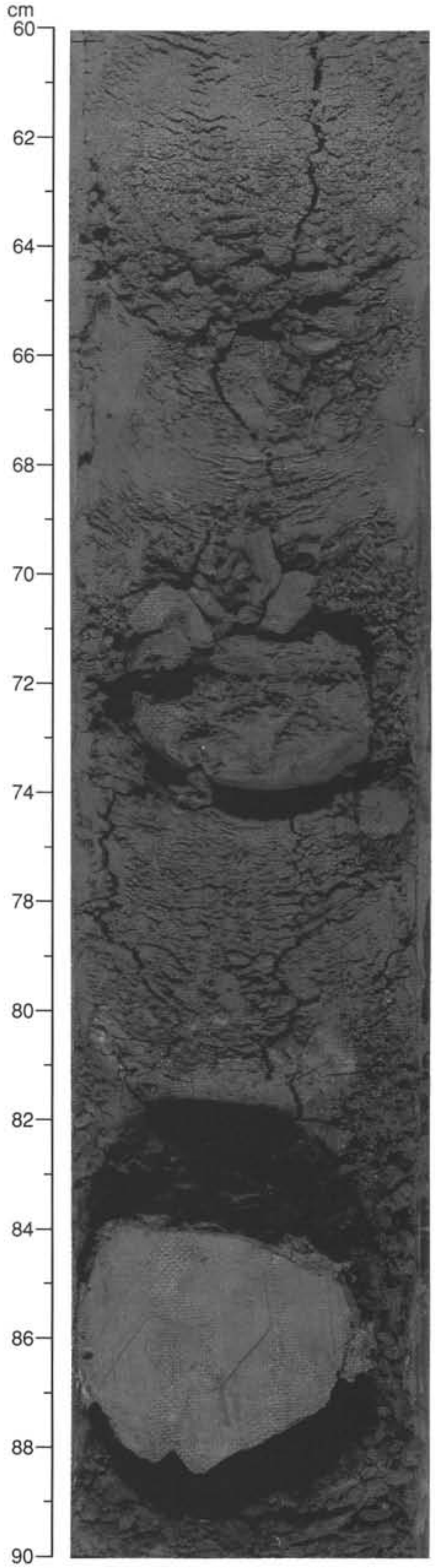

Figure 16. Isolated pebbles in Section 146-888B-54X-1, 60–90 cm, from lithostratigraphic Subunit IIIB. The pebble at about 73 cm is composed of indurated clayey silt. The pebble at about 86 cm is composed of carbonate precipitates. The rounded shape of both clasts was produced by drilling.

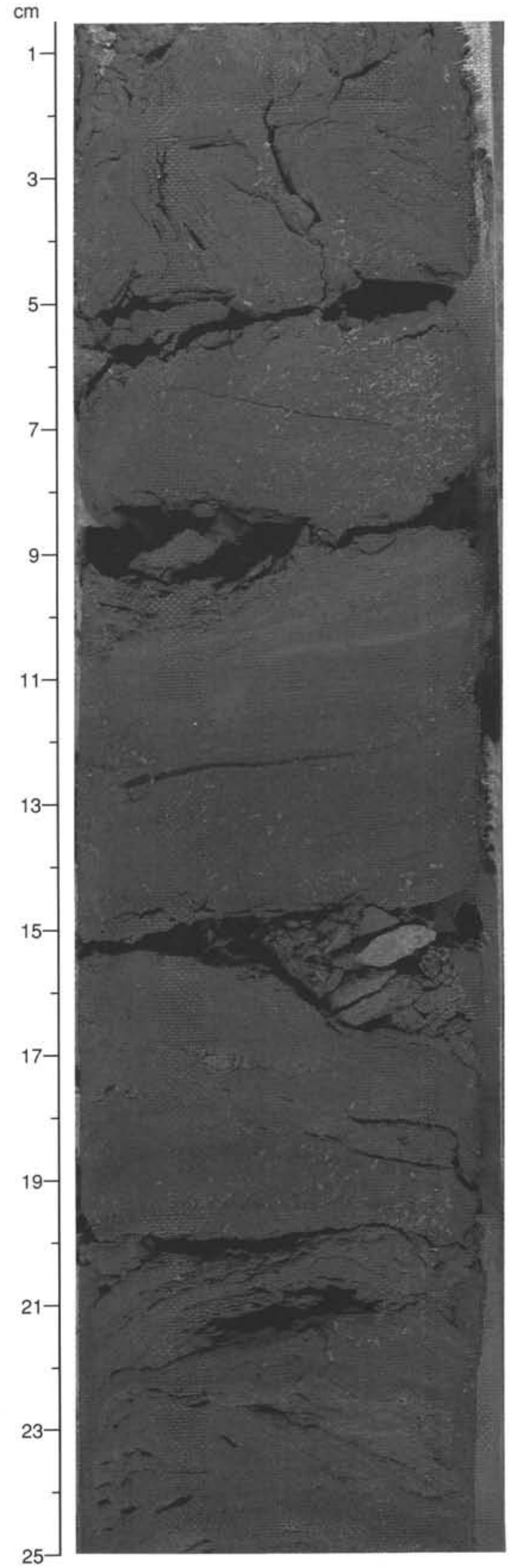

Figure 17. Isolated pebble (at 15–16 cm) composed of carbonate precipitates was broken by drilling in Section 146-888B-65X-CC, 0–25 cm, from lithostratigraphic Subunit IIIB.

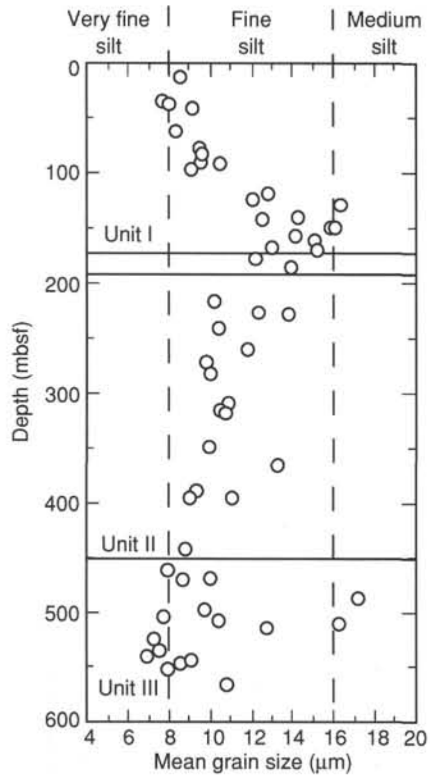

Figure 18. Downhole mean grain-size distribution of the fine-grained sediments of Hole 888B.

cases to medium silt). Although the absolute values of the size may be biased by the instrument, it is important to note that the grain size of the fine sediments is extremely homogeneous throughout the section. The mean size begins to increase uphole at the base of Unit II with a low gradient, for a total increase of about 8 µm. A maximum in the profile is reached at the base of lithostratigraphic Unit I (Cores 146-888B-14H to -19H) with the mean size in the medium silt range. The uphole decrease above the maximum within Unit I is sharp between the base of the unit and about 100 mbsf, and becomes gentler in the uppermost section of the unit.

A possible implication of the grain-size profile is that the change in gradient at about 100 mbsf is related to a major discontinuity within lithostratigraphic Unit I evidenced by physical properties, geochemistry, seismic stratigraphy, and logging results (see respective sections, this chapter). Such a discontinuity could be an erosional truncation (very low angle unconformity or paraconformity) that interrupts the trend of decreasing grain size in time.

X-ray Diffraction Data

X-ray diffraction (XRD) analyses were conducted on more than 30 samples of fine sediments from Hole 888B. The clay mineral reflections are weak relative to those of quartz and feldspars because the samples were analyzed as random mounts of the whole rock that include silt-sized fragments of these two components. Follow-up studies using oriented mounts of the <2µm size range are planned to determine the clay mineral abundances semiquantitatively. Figure 20 shows representative samples of silts and clays from the cored interval of Hole 888B. The data are plotted in a qualitative way only, showing relative increases and decreases in the abundances of the minerals, calculated from the square of their characteristic peak intensities, and normalized to sum to 100%. In this way the main changes in composition are shown, without attaching unwarranted precision to the data.

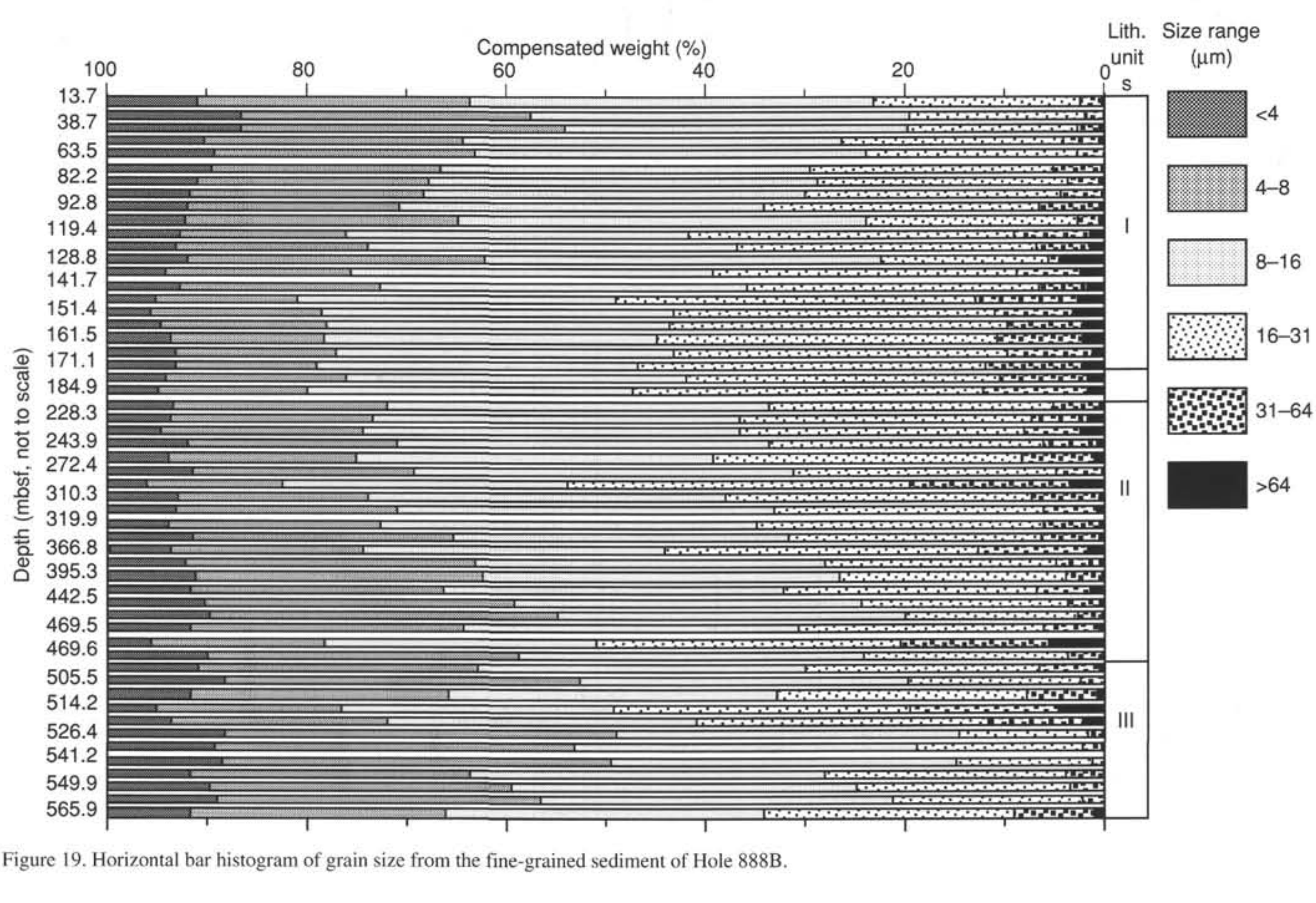

Figure 19. Horizontal bar histogram of grain size from the fine-grained sediment of Hole 888B.

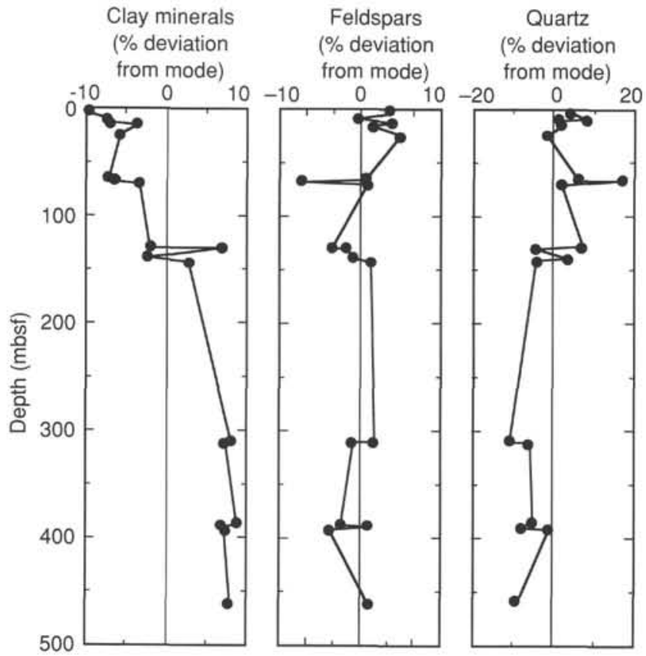

Figure 20. Changes in mineralogy with depth in Hole 888B as determined qualitatively from X-ray diffraction data. The proportions plotted were calculated from the square of the peak height (which is proportional to reflection intensity). The proportions from each phase are shown as a percentage deviation from the modal proportion for the hole. The 3.34 Å intensity of quartz and the 3.20 Å intensity of feldspar were compared with the average intensity of three clay minerals (4.55, 4.70, and 4.46 Å reflections of micas, chlorite/kaolinite, and smectite, respectively). The intensities for each sample were normalized to sum to 100%, irrespective of other components.

Table 2. Sedimentary facies scheme adopted for Leg 146 (after Mutti and Ricci Lucchi, 1972, *in* Siemers et al., 1981).

TURBIDITE FACIES TYPES

Facies A. Massive, graded to nongraded, poorly sorted, coarse–grained sandstones, conglomeratic sandstones, and conglomerates in thick, irregular (channeled) and amalgamated units that formed from locally downcutting, to highly erosive, mass-flow and grain-flow mechanisms.

Facies B. Predominantly horizontally laminated to massive-appearing, fine- to medium-grained, well-sorted sandstones in relatively laterally continuous thick beds that are thought to be the product of turbidity currents and upper flow regime tractive currents. Locally Facies B may include cross-bedding and fluid-escape structures. Bottom markings are rare.

Facies C. "Classical," relatively thick (50–150 cm), complete Bouma "a-e" sequence turbidites composed mainly of fine- to medium-grained sandstone and interbedded with minor amounts of shale; inferred to be the product of turbidity currents.

Facies D. Relatively thin (3–40 cm), incomplete Bouma sequence (commonly "c-e") turbidites composed mainly of fine- to very fine-grained sandstone and interbedded with relatively thick shale intervals (sand/shale ratios of 1:2 to 1:9); this facies is inferred to be the product of low-density turbidity currents.

Facies E. Commonly observed as isolated lenses of sandstones in shale. Sandstones are coarser and more poorly sorted than any other local sand facies. Stratification surfaces show marked irregularity with pitch-and-swell structures and lenticular bedding. Top and basal contacts are sharp; tops are commonly ripple formed. High-angle traction cross-bedding is common. Grading is common. Sand/shale ratio commonly exceeds 1:4. Sandstones assigned to this facies are inferred to be the product of local processes related to overbank deposition along generally confined channels or to "bypass" at the ends of mid-fan distributary channels.

ASSOCIATED NONTURBIDITE FACIES TYPES

Facies F. Chaotic soft-sediment-deformed deposits composed of various types of sediments that were deformed by the mass movement (e.g., slumping, flowing and sliding) of unconsolidated sediment. When composed mainly of shale, Facies F may be part of a slope deposit.

Facies G. Thick intervals of hemipelagic and pelagic silty shales, marls, and carbonates that formed from "normal" suspension sedimentation and dilute turbidity currents.

FACIES ASSOCIATION

1. Slope Association. Sedimentary sequence dominated by the fine-grained sediments of Facies G and with significant development of the chaotic deposits of Facies F and possible presence of channel-fill deposits of Facies A.

2. Submarine Fan Association.

(a) Inner Fan Subassociation. Characterized by submarine channels filled by Facies A and B (±F) and surrounded by Facies C and G and, possibly, some intervals of Facies D and E.

(b) Middle Fan Subassociation. Broadly lenticular channel sandstone bodies dominated by Facies A and B (±F) and displaying cycles with a general upward decrease in grain size and bed thickness. Vertical and lateral interfingering locally with Facies C and D.

(c) Outer Fan Subassociation. Composed of Facies C to D sediments. An upward increase in grain size and bed thickness to form lobes is common. Intervals of Facies G may also be observed.

3. Basin Plain Association. Composed of Facies D and G sediments including hemipelagic deposits.

Sedimentary Processes

In spite of drilling disturbance, it was usually possible to recognize the character of bedding, the presence of repeated gradational transitions from coarse to fine sediments, and the presence of fining-upward sandy layers. From this evidence we interpret the sediments recovered at Site 888 as of turbiditic origin. The main sedimentary processes were thus transport and deposition of unconsolidated sediments by gravity flows. The absence of hemipelagic sediments or contourites may be either caused by erosion from turbidity flows or homogenization of these extremely delicate layers from drilling.

In the recognition and interpretation of these depositional environments, we followed three steps: (1) visual core description (completing the VCD forms and drawing the graphic lithology column; Fig. 21), (2) recognition of elementary sedimentary units diagnostic of facies or genetic types, and (3) modelling of possible sedimentary environments on the basis of facies associations. The model of facies associations is that of Mutti and Ricci Lucchi (1972) (Table 2).

Three facies types (B, C, and D) were identified according to Table 2. Grain size does not seem to be the dominant parameter, because it is dependent not only on transport processes and proximity of deposition, but also on the composition of the original mass involved in the gravity flow. The sand/mud ratio seems more informative.

The facies pattern at Site 888 is rather monotonous and belongs to the "submarine fan association" (Table 2, facies association 2). Nevertheless, differences among the lithostratigraphic units can be delineated.

Lithostratigraphic Unit I is represented by Facies C and D, inferred to be formed by normal- and low-density turbidity currents. Facies D is evidently dominant, whereas Facies C reflects local occurrence or comparatively short active periods. Such facies association is indicative of the outer submarine fan subassociation (Table 2, facies association 2c), where sediments were deposited by low-energy, low-density turbidity currents in a sedimentary environment on the boundary between fan and abyssal plain.

Lithostratigraphic Unit II contains the three facies types, but sediments of Facies B prevail. Isolated, thin instances of Facies D (e.g., Core 146-888B-26H) may have formed in depressions between active distributary channels, or they may reflect pauses in migration cycles of the channel. Typical "fan-lobe" Facies C sequences can be traced throughout Unit II. Nevertheless, the limited recurrence of this facies supports other evidence for migrating distributary systems. In general, the observed facies association reflects the "middle fan subassociation," where processes of discharge and bypassing of sediments take place simultaneously. We suppose that the observed facies pattern is characteristic for the entire sequence of Unit II; although the recovery was low, well-log data support this interpretation (see "Downhole Logging" section, this chapter).

Lithostratigraphic Unit III is represented by Facies C and D ("outer fan subassociation") and is sedimentologically similar to Unit I. Turbidites of Unit III seem to be more distal than in Unit I (there are fewer sandy layers, and a lower sand/mud ratio) and appear to be more restricted to an abyssal plain environment.

In the modern physiographic setting (Fig. 22) the depositional environment at Site 888 has been dominated by the presence of the adjacent Nitinat deep-sea fan. The sampled sedimentary section (dated to younger than 0.6 Ma, see "Biostratigraphy" and "Paleomagnetism" sections, this chapter) includes only one major high-energy depositional sequence (Unit II). We advance two possible explanations for this single interval over a time span as much as 0.6 Ma:

1. Temporary northward migration of the Nitinat Fan lobe that intersected the location of Site 888 (otherwise resting in the outer portion of the fan);
2. As a result of the 44 mm/yr northeasterly motion of the subducting Juan de Fuca Plate relative to North America, the location of Site 888 traveled as much as 26.4 km from the outer fan environment (Unit III) to the middle fan environment (the Nitinat Fan lobe, Unit II) and then to its present position to the northwest of the mouth of the deep-sea canyon of the Nitinat Fan (Unit I). The position of Site 888 during the deposition of Unit I is more proximal to the sediment source than was the case during the deposition of Units II and III, but it receives smaller amounts of coarse material because it lies outside the area of modern of high-energy deposition.

BIOSTRATIGRAPHY

An apparently continuous sequence of upper Pleistocene sediments was cored at Site 888. Planktonic and benthic foraminifers occur at many intervals and are rare to abundant in sediments from both Holes 888A and 888B. Radiolarians occur at only a few intervals and in very low abundance. Ten samples from Hole 888B (Samples 146-888B-1H-CC to -10H-CC, 5.4–91.5 mbsf) were examined for calcareous nannofossils. All ten samples are barren.

Hole 888A, represented by a single core, recovered uppermost Quaternary sediments. An upper Pleistocene record (less than 0.6 Ma) was recovered from Hole 888B.

Planktonic Foraminifers

Moderately to well-preserved Quaternary planktonic foraminifers are rare to abundant in 48 core-catcher samples from Holes 888A and 888B (Table 3). Thirteen samples are barren. The planktonic assemblages are dominated by *Globigerina bulloides, Neogloboquadrina pachyderma* (sinistral), *Globorotalia scitula,* and *Globigerina quinqueloba* with rare occurrences of the other taxa listed in Table 3.

Age determinations based on occurrences of planktonic foraminifers are difficult at Site 888, because no evolutionary datum was found. Application of the coiling zonation scheme of Lagoe and Thompson (1988) is tentative until more detailed analyses can be completed. *N. pachyderma* (dextral) are present above Sample 146-888B-19X-CC (172 mbsf) and in the interval from Samples 146-888B-51V-CC (452.1 mbsf) through -61X-CC (526.9 mbsf), but sinistrally coiled forms dominate many of these samples. The entire section is considered to be part of Zones CD1–8 of Lagoe and Thompson (1988) (see "Explanatory Notes" chapter, this volume) and cannot be further divided because no definite dextral coiling intervals are defined.

Most of the core-catcher samples contain only sinistrally coiled *N. pachyderma* assemblages, indicating cold surface waters for the entire section. In intervals containing both dextral and sinistral forms of *N. pachyderma* (Table 3), either sinistrally coiled forms are dominant or too few specimens of both forms are present to calculate a coiling ratio.

Table 3. Distribution and zonation of planktonic foraminifers in core-catcher samples from Site 888 and surface-water paleotemperature.

Core and section	Depth (mbsf)	Abundance	Preservation	*Globigerina bulloides*	*Globigerina quinqueloba*	*Globigerina umbilicata*	*Globigerinita glutinata*	*Globorotalia inflata* (modern form)	*Globorotalia scitula*	*Globorotalia tumida*	*Neogloboquadrina dutertrei*	*Neogloboquadrina pachyderma* (d)	*Neogloboquadrina pachyderma* (s)	*Orbulina universa*	Paleotemperature	Coiling dominance zone	Epoch
146-888A-															Cold surface waters	CD1 to CD8	Quaternary
1H-CC	9.5	A	G	F	F					R		R	R				
146-888B-																	
1H-CC	5.4	A	G	C					F				C				
2H-CC	15.1	F	G	R			R		R								
3H-CC	25.3	C	G	C		R	R		R			R	C				
4H-CC	34.8	R	G	R					R				R				
5H-CC	44.1	A	G	C	F				R			R	A				
6H-CC	53.5	C	G	C		R			R	R		F	C				
7H-CC	63.1	C	G	F					R				F				
8H-CC	71.7	C	G	F									F				
9H-CC	81.5	F	G	F	R							R	F				
10H-CC	91.5	F	G	R									F				
11H-CC	101.0	C	G	F			R					R	F				
13H-CC	118.5	A	G	C									C				
14H-CC	127.9	F	G	R					F			R	F				
15H-CC	137.6	F	G	F	R				R			R	R				
16H-CC	147.0	R	G	R	R								R				
17H-CC	155.8	R	G	R									R				
18X-CC	162.4	F	G	R					R		R	R	F				
19X-CC	172.0	R	G	R	R								R				
20X-CC	176.0	F	G	R									F				
22X-CC	194.2	R	M										R				
25H-CC	226.5	R	G	R									R				
26H-CC	234.1	A	G	C							R		C				
28H-CC	251.8	F	G	R	F								F				
31H-CC	276.9	R	G	R	R								R				
35H-CC	311.1	R	M										R				
36H-CC	319.8	R	M										R				
37H-CC	329.7	C	G	F									F				
41X-CC	357.9	C	M	F									R				
43X-CC	376.0	C	M	F			R		R				F				
44X-CC	393.7	C	G	F			R		R				C				
45X-CC	398.7	R	G										R				
48X-CC	423.8	F	G	R									F				
49X-CC	433.0	R	G	R									R				
50X-CC	442.8	R	M										R				
51V-CC	452.1	R	G	R								R	R				
52X-CC	452.5	R	M	R	R												
54X-CC	471.5	C	M	C			R					R	C	R			
55X-CC	478.7	C	G	C	R		R				R	R	C				
56X-CC	488.1	R	M		F							R	R				
57X-CC	501.3	F	G	F									F				
58X-CC	510.7	F	G	R	R								F				
60X-CC	515.8	A	G	C									A				
61X-CC	526.9	F	G	R	F	F	R		R			R	R				
62X-CC	536.1	R	G		R								R				
63X-CC	546.6	R	G	R									R				
64X-CC	556.3	R	G										R				
65X-CC	566.3	R	G										R				

Note: Dextral (d) and sinistral (s) *N. pachyderma* are listed separately. Abbreviations for abundance are as follows: A = abundant, C = common, F = few, and R = rare. Abbreviations for preservations are as follows: G = good, and M = moderate. See "Explanatory Notes" chapter (this volume) for an explanation of these categories.

Benthic Foraminifers

Benthic foraminifers are rare to common in 34 core-catcher samples from Hole 888B and are common in Sample 146-888A-1H-CC (9.8 mbsf). Thirteen samples containing planktonic foraminifers do not contain benthic foraminifers. Most specimens are moderately to well preserved. No sign of dissolution is present, but some specimens, especially thin-walled forms, are broken.

Six samples (146-888A-1H-CC (9.5 mbsf), 146-888B-31H-CC (276.9 mbsf), 146-888B-54X-CC (471.5 mbsf) through -56X-CC (488.1 mbsf), and 146-888B-60X-CC (515.8 mbsf)) contain lower bathyal faunas consisting of rare *Cibicidoides wuellerstorfi, Gyroidina soldanii, Melonis pompilioides, Pullenia bulloides,* and *Uvigerina senticosa.* The remainder of the samples contain mixed neritic through middle bathyal assemblages with common occurrences of *Bulimina striata, Buliminella exilis, B. subfusiformis, Cassidulina*

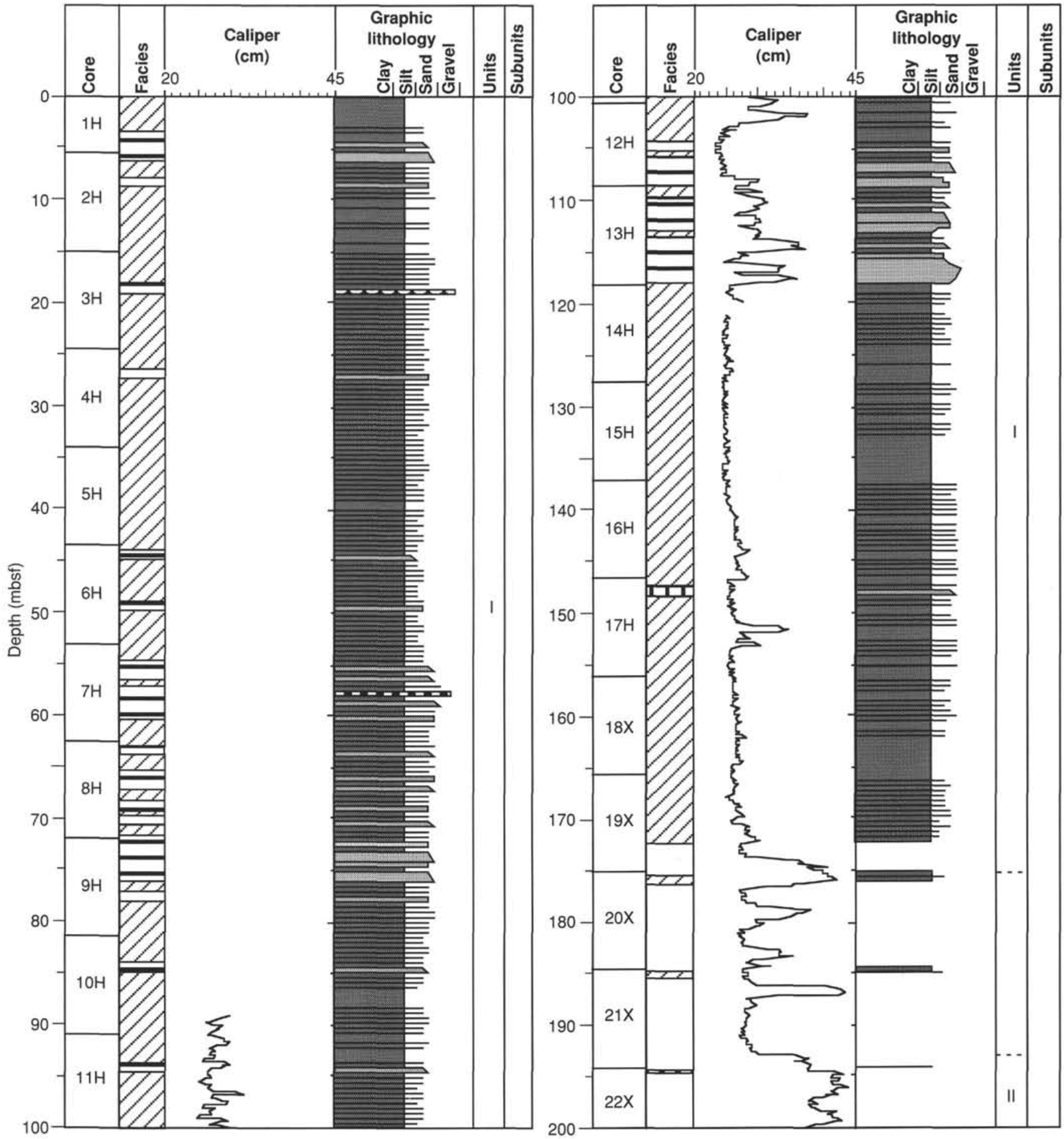

Figure 21. Graphic lithologic representation of Hole 888B. For explanation of the facies see text and Table 2. The caliper log column shows close correlation with the lithologic column (sand corresponding to large hole diameter, silt to small hole diameter).

limbata, C. minuta, Elphidium excavatum clavatum, Globobulimina spp., and *Uvigerina peregrina.* Table 4 contains a preliminary list of the benthic foraminifers present in Holes 888B and 888A.

Although middle bathyal and shallower faunas are common at this site, they occur in turbidites (see "Lithostratigraphy" section, this chapter) that were transported into deeper waters. The six samples containing lower bathyal faunas and the position of Site 888 on the abyssal plain of the Juan de Fuca Plate indicate that the sediments recovered at this site were all deposited in a lower bathyal environment.

Radiolarians

All core-catcher samples from Holes 888A and 888B were processed and examined for radiolarians. Rare and well-preserved radiolarians characteristic of the late Quaternary *Botryostrobus aquilonaris* Zone (Hays, 1970) were found in sediments near the top of the sequence from Hole 888A (Sample 146-888A-1H-CC at 9.5 mbsf) and in Samples 146-888B-1H-CC through -18X-CC (5.4–162.5 mbsf) from Hole 888B. In this interval, four samples of coarse

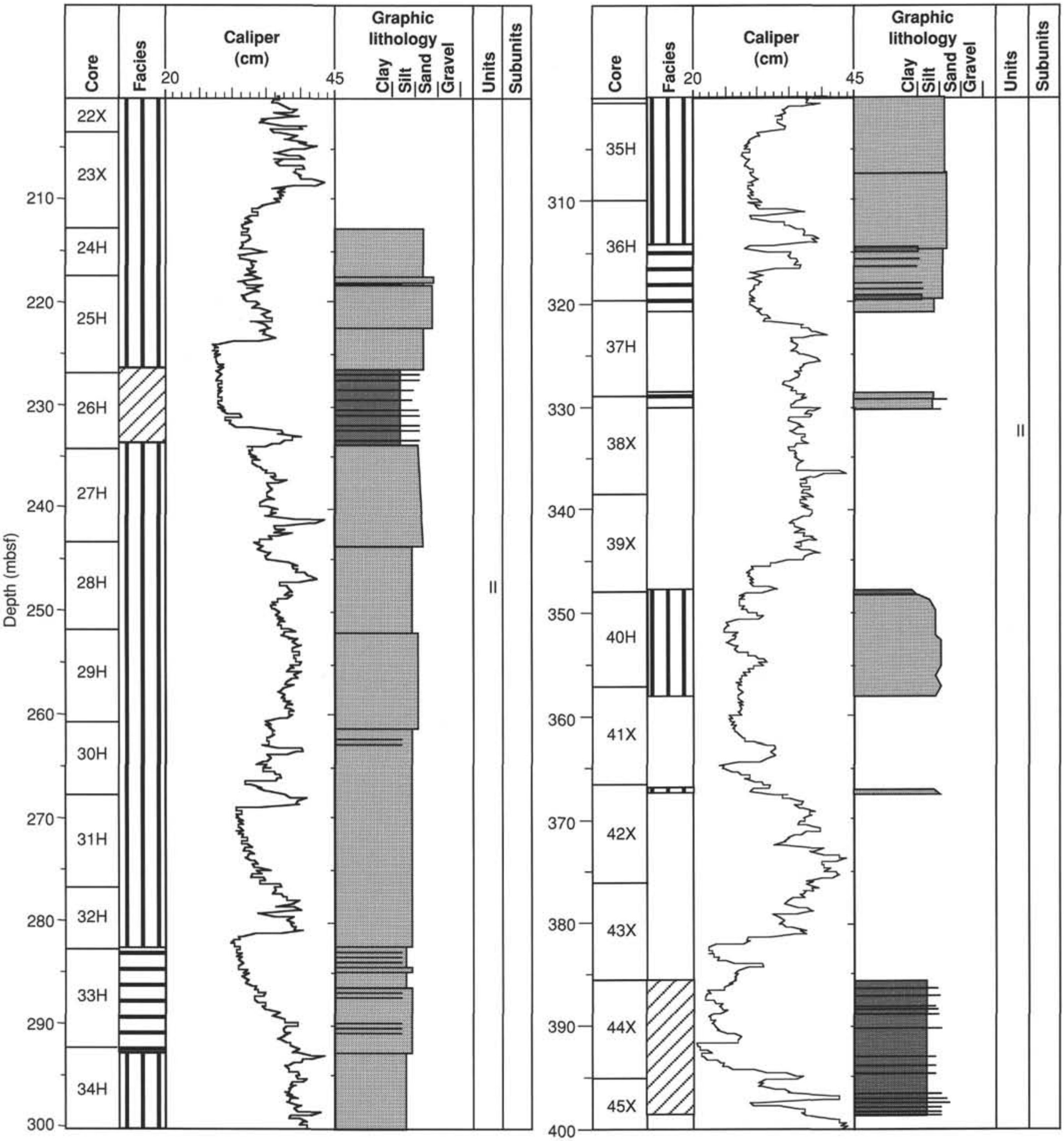

Figure 21 (continued).

sand (Samples 146-888B-8H-CC, -9H-CC, -12H-CC, and -13H-CC [72–118 mbsf]) appear to be barren. Samples 146-888B-19X-CC through -36H-CC (172–319.8 mbsf) are barren. Very rare and well-preserved Pleistocene radiolarians were found in Samples 146-888B-37H-CC through -41X-CC (329.7–357.9 mbsf). No stratigraphic marker was recognized. All core-catchers downhole are barren, with the exception of Sample 146-888B-54X-CC (471.5 mbsf), where rare Pleistocene radiolarians were observed.

All specimens are typical of the Arctic Pleistocene radiolarian assemblage. Rare species indicative of upwelling areas (Nigrini and Caulet, 1992) are present in Samples 146-888A-1H-CC (9.5 mbsf) and 146-888B-42X-CC (367.2 mbsf).

PALEOMAGNETISM

Paleomagnetic and rock-magnetic studies of undisturbed to moderately disturbed sections of core were conducted to determine the magnetostratigraphy and magnetic anisotropy in Holes 888A and 888B. A complete magnetic record was obtained from lithostratigraphic Unit I. The magnetostratigraphy of Units II and III is incom-

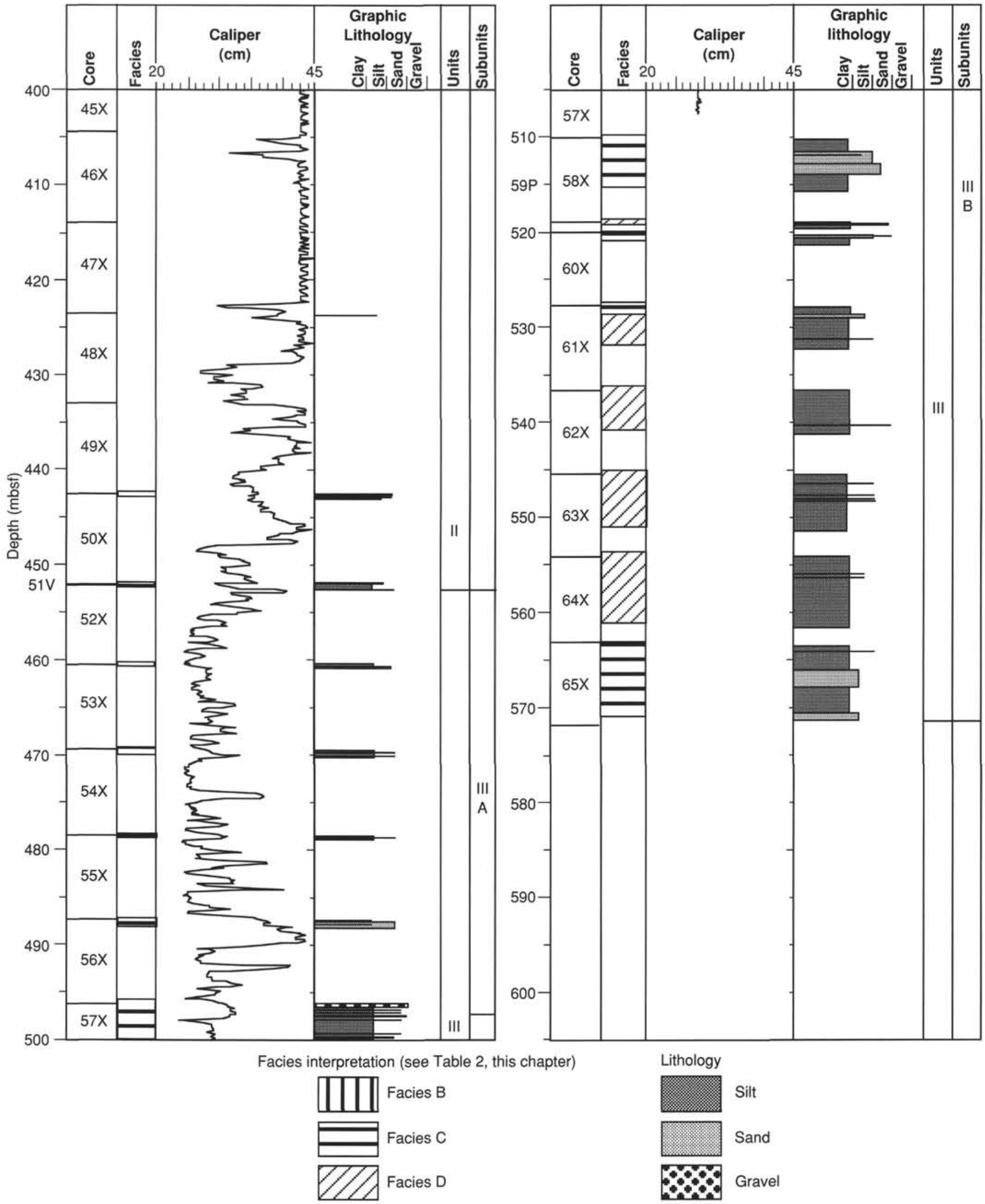

Figure 21 (continued).

Table 4. Preliminary list of benthic foraminifers recovered at Site 888.

Bolivina spp.
Bolivina interjuncta
Bolivina spissa
Buccella frigida
Buccella tenerrima
Bulimina sp.
Bulimina striata
Bulimina subacuminata
Buliminella curta
Buliminella exilis
Buliminella subfusiformis
Buliminella tenuata
Cassidulina californica
Cassidulina cushmani
Cassidulina limbata
Cassidulina minuta
Cassidulina spp.
Cassidulina translucens
Cibicides spp.
Cibicidoides spp.
Cibicidoides wuellerstorfi
Eggerella bradyi
Elphidiella hannai
Elphidiella oregonense
Elphidium excavatum clavatum
Elphidium spp.
Epistominella pacifica
Fissurina lucida
Globobulimina auriculata
Globobulimina pacifica
Globobulimina sp.
Globocassidulina subglobosa
Gyroidina soldanii
Hoeglundina elegans
Melonis pompilioides
Nonionella globosa
Nonionella miocenica
Nonionellina labradorica
Oridorsalis umbonatus
Plectofrondicularia advena
Pullenia bulloides
Pyrgo spp.
Quinqueloculina spp.
Saccammina sphaerica
Sigmoilina sp.
Trifarina fluens
Uvigerina dirupta
Uvigerina peregrina
Uvigerina senticosa
Valvulineria araucana

plete owing to a combination of poor core recovery and intense drilling deformation. The remanent magnetization of the archive half of relatively undisturbed cores was measured in the pass-through cryogenic magnetometer. Discrete samples were also taken from each core section to more completely characterize the remanence. Anisotropy of magnetic susceptibility (AMS) measurements were also conducted on these discrete samples, to serve as undeformed reference fabrics for the remaining sites on Leg 146.

Paleomagnetic Results

The natural remanent magnetization (NRM) of the cores was predominantly in a steeply inclined upward direction with an intensity of 100–1000 mA/m. Demagnetization of the cores with an alternating field (AF) of up to 15 mT removed this steep upward direction in the majority of the cores, leaving a stable, predominantly normal polarity (positive inclination) remanence throughout the hole. Summary declination, inclination, and intensity plots for Hole 888B are shown in Figure 23. The data for Unit I are well defined; for Units II and III the results are scattered as a result of drilling disturbance and a variably removed overprint. The discrete samples were AF demagnetized in 5- or 10-mT steps to 60–100 mT. The majority of the results from these samples show two components of magnetization. The first-removed component is the steep upward overprint direction, which is completely removed by 20 mT and probably was acquired during

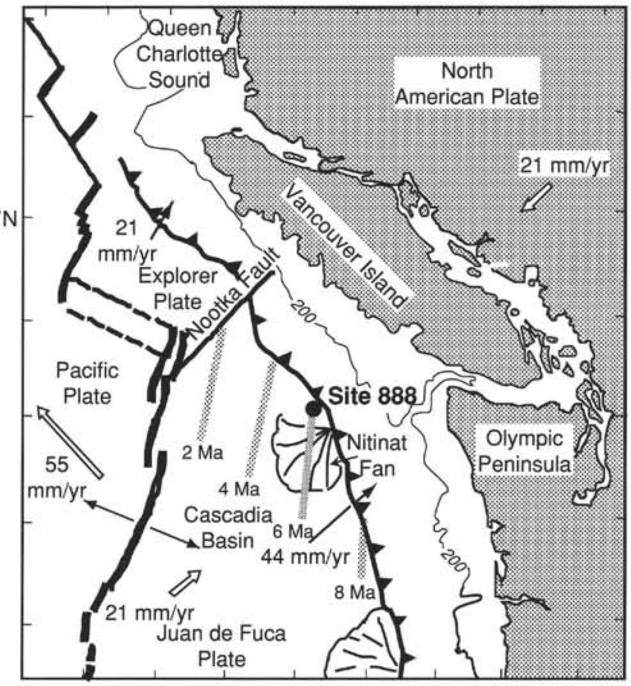

Figure 22. Location of Site 888 with respect to the main physiographic and tectonic features of the region. Seafloor ages on the Juan de Fuca Plate, and absolute (open arrows) and relative (filled arrows) rates of plate motion are indicated.

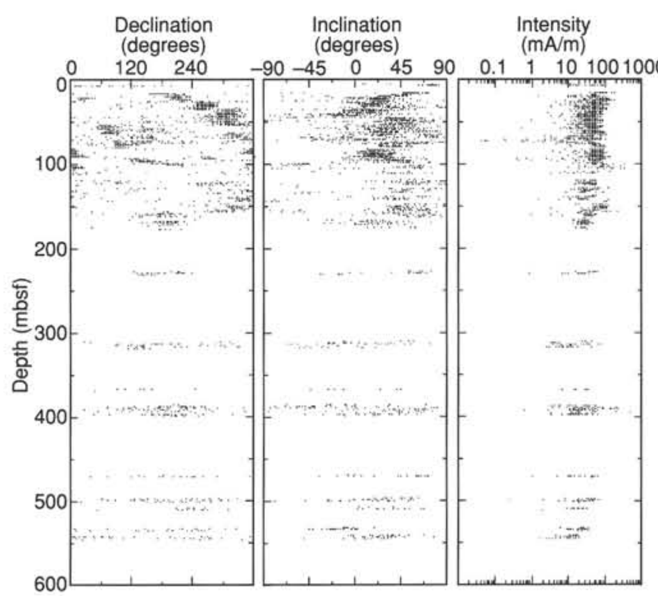

Figure 23. Summary declination, inclination, intensity plots for split-core sections from Hole 888B after 15-mT AF demagnetization. Declinations are oriented where possible.

drilling and core recovery. The second-removed component is a moderately inclined, downward direction, which is removed between 10 and 80 mT (Fig. 24).

Using the orientations provided by the Eastman-Whipstock multishot downhole tool for Cores 146-888B-6H to -17H, the characteristic remanence direction for discrete samples from this interval was plotted in geographic coordinates (Fig. 25). The mean direction from these samples is 236°/59° (declination/inclination), $\alpha_{95} = 20°$, k = 4.0.

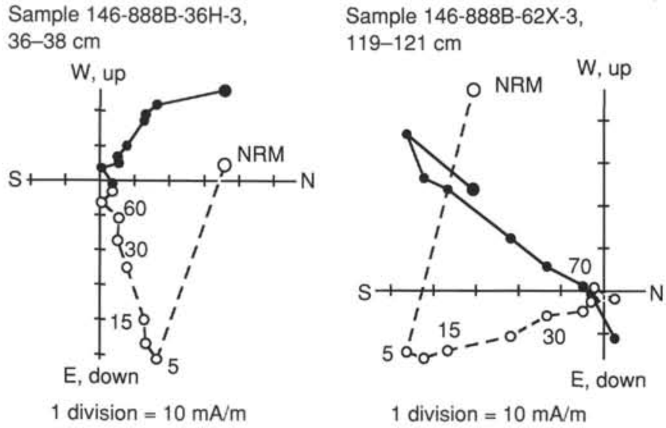

Figure 24. Zijderveld vector diagrams showing the typical AF demagnetization behavior of discrete samples. The solid symbols are projections of the horizontal (declination direction) component of magnetization, the open symbols are projections of the vertical (inclination) component of magnetization. Alternating-field levels (in mT) provided for several demagnetization steps are plotted adjacent to the corresponding vertical magnetization component. The orientations are uncorrected for core declination.

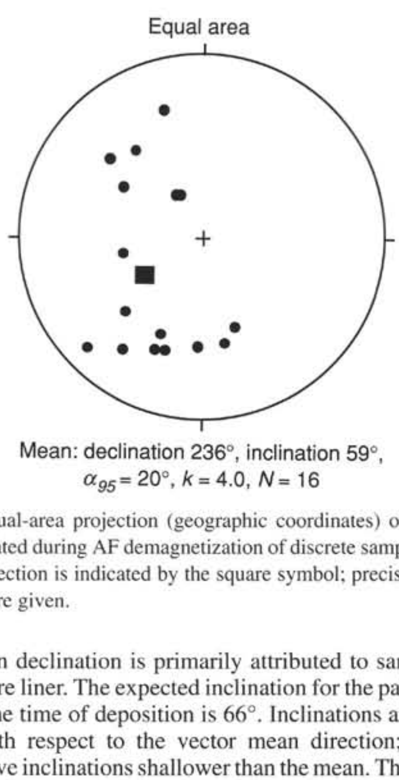

Figure 25. Equal-area projection (geographic coordinates) of characteristic directions isolated during AF demagnetization of discrete samples. The calculated mean direction is indicated by the square symbol; precision parameters for the mean are given.

The scatter in declination is primarily attributed to sample rotation within the core liner. The expected inclination for the paleolatitude of Site 888 at the time of deposition is 66°. Inclinations are distributed unevenly with respect to the vector mean direction; all but two directions have inclinations shallower than the mean. The distribution of the inclinations, as well as some of the declination variation, may be caused by inclination-shallowing during sedimentation and/or an incompletely removed overprint. We assign all of Hole 888B to the Brunhes (N) Chron, giving a maximum age of 0.780 Ma (Cande and Kent, 1992) for the bottom-hole sediments.

A short interval within Hole 888B shows a departure from normal-polarity behavior. Figure 26 shows the declination, inclination, and intensity plot for Cores 146-888B-11H to -12H. A consistent reversed polarity interval occurs between 98 and 101 mbsf in the whole-core remanence after 15-mT AF demagnetization. Detailed study of the remanence of this interval was conducted by means of demagnetization of 14 additional discrete samples taken from Cores 146-888B-11H and -12H, spanning the reversed polarity interval and

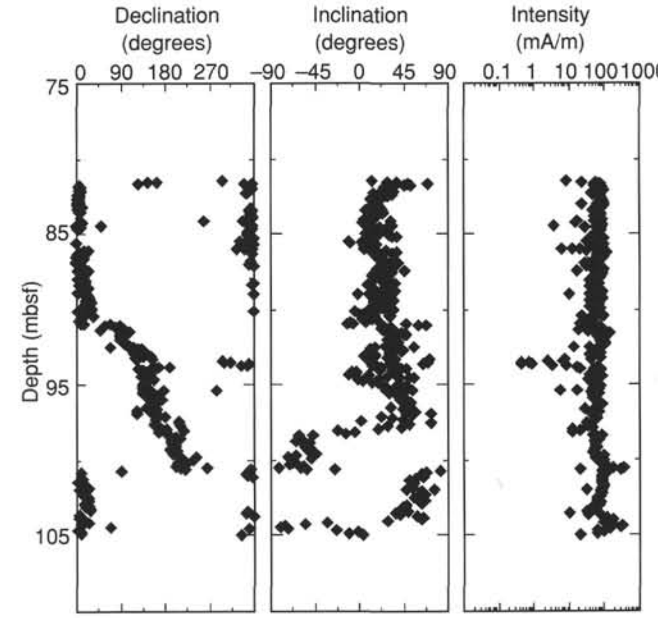

Figure 26. Declination, inclination, and intensity plots of split-core remanence data (after 15-mT AF demagnetization) for the interval from 90 to 105 mbsf, with orientations corrected using multishot data. Reversed-polarity (negative) inclinations between 98 and 101 mbsf may represent the 0.11-Ma Blake (R) Event in the Brunhes (N) Chron.

part of the normal polarity interval on either side. Alternating-field demagnetization of these samples in 5-mT steps from NRM to 75 mT revealed one of two second-removed components; either a shallowly inclined upward to downward direction or a steeply inclined downward direction after removal of the steep upward overprint (Fig. 27). After correction for orientation, the steep downward inclination directions are northerly, similar to the characteristic normal polarity remanence in the rest of the hole, although more scattered declinations occur in the samples near the reversed-polarity interval. The shallow-inclination components have a southerly declination consistent with the suggestion of a reversed-polarity remanence. However, the stepwise demagnetization behavior of these samples does not completely isolate a stable reversed characteristic direction, as shown by the curved trajectories of the Zijderveld diagrams in Figure 27.

Two possible explanations exist for the shallow-inclination, southerly directions. The first possibility is that the steep-upward overprint is not completely removed in these samples by 20-mT AF demagnetization. Simultaneous removal of this drilling-induced overprint and the characteristic normal polarity direction observed elsewhere in Hole 888B could produce the curved demagnetization trajectories and shallow inclinations observed in the remanence of this section. The second possibility is that this section represents a short-duration, reversed-polarity event (most likely the Blake Event of about 0.110 Ma) within the Brunhes (N) Chron. This event is suggested by the consistent pattern of anomalous inclinations in this interval and the southerly direction of the shallow upward directions. The inclinations (see Fig. 26) show two periods of reversed polarity separated by a short normal-polarity interval. This "double reversal" is characteristic of other paleomagnetic records of the Blake Event (Tric et al., 1991), and suggests that the interval from 98 to 101 mbsf contains a record of the Blake Event. In addition, discrete samples taken from other cores in which upward inclinations persisted in the whole-core measurements demagnetized to 15 mT (see Fig. 23) displayed complete removal of the drilling-induced overprint by 30 mT, with a stable, normal-polarity characteristic remanence isolated by higher demagnetization fields (see Fig. 24). The erratic behavior of the remanence at high (>50 mT) AF steps in the samples from Cores 146-888B-11H

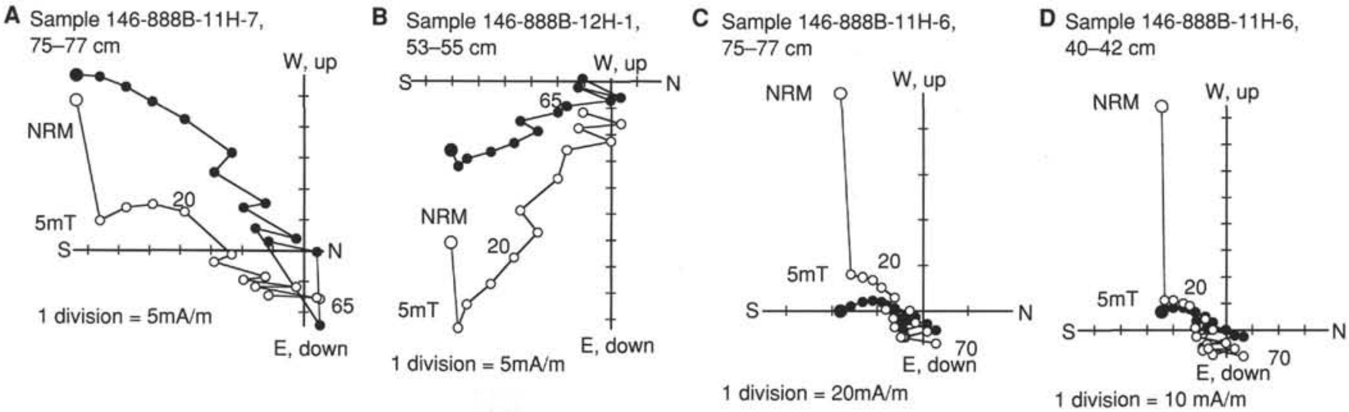

Figure 27. Zijderveld vector diagrams of AF demagnetization results for individual samples taken from the interval 90–105 mbsf plotted in Figure 26. The samples are corrected for orientation. Symbols as in Figure 24. Figures 27A, 27B, and 27D show shallow-upward to shallow-downward directions isolated after (partial?) removal of the steep-upward overprint direction. Figure 27B shows the steep-downward direction. This sample was taken less than 1 m below the interval of reversed polarity, and its declination remains southerly, despite its positive inclination. Compare with Figure 24.

and -12H is consistent with previous observations of the AF demagnetization behavior of greigite (Krs et al., 1990; Musgrave et al., 1993), and it may be that the higher coercivity remanence in these samples is carried by greigite. If this is the case, then the lower coercivity, apparently reversed-polarity component may be carried by magnetite. This would be consistent with a depositional or early postdepositional origin for the reversed-polarity component. The appearance of magnetic sulfides in this interval is also consistent with the observations of sulfate reduction (see "Inorganic Geochemistry" section, this chapter) in this interval. Although further rock-magnetic and mineralogic studies are needed to characterize the remanence of this interval, we have tentatively included the Blake Event in the magnetostratigraphy of Hole 888B (see Fig. 77). This places a maximum age of 0.11 Ma for the sediment at 101 mbsf, and, if correct, yields a sedimentation rate of 0.9 m/1000 yr.

Rock-magnetic Results

Anhysteretic remanent magnetization (ARM) acquisition studies were conducted using the ring-core fluxgate spinner magnetometer (see "Explanatory Notes" chapter, this volume). All samples show a progressive increase in ARM from 0 to 24 mT (Fig. 28), indicating the presence of low-coercivity ferrimagnetic minerals; either coarse-grained magnetite (grain size > 5 μm; Jackson et al., 1986), greigite, or pyrrhotite (grain size > 20 μm; Dekkers, 1988).

Magnetic susceptibility and AMS (see "Structural Geology" section, this chapter, for AMS results) were measured on paleomagnetic samples from each intact core from Hole 888B. Mean susceptibility varied from 0.9×10^{-3} to 4.9×10^{-3} SI units (Fig. 29). The mean susceptibility of lithostratigraphic Units I and II averaged 2×10^{-3}, whereas Unit III was characterized by a higher susceptibility (3.5×10^{-3}). The relatively high mean susceptibility (Borradaile et al., 1987) and ARM results suggest that either magnetite, pyrrhotite, or greigite is the primary contributor to the measured susceptibility.

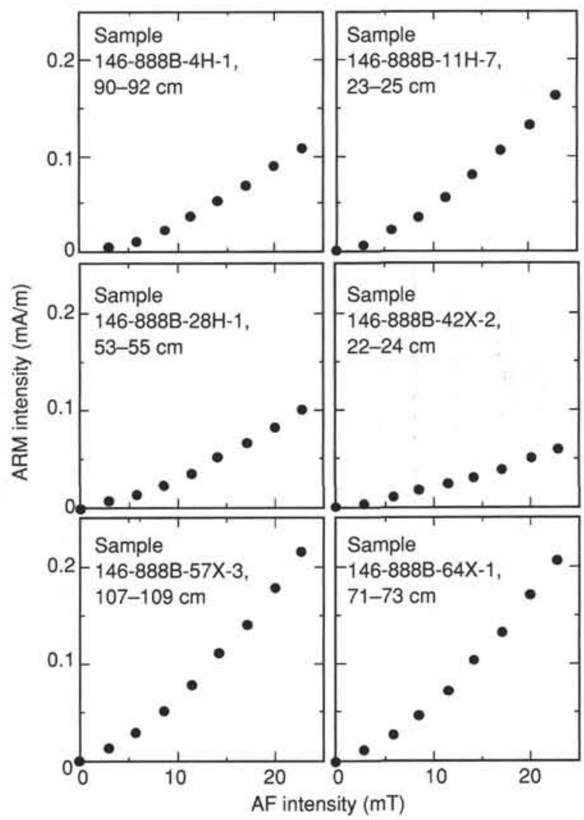

Figure 28. Plots of progressive ARM acquisition from 0- to 24-mT AF levels. The vertical axis is intensity, and the horizontal axis is AF level.

STRUCTURAL GEOLOGY

The interval drilled at Site 888 apparently consists of 567 m of flat-lying sediment undeformed by tectonic stresses. However, structural information is limited on account of the poor core recovery, drilling disturbance in the XCB cores that were recovered, and absence of lithification of the sediments.

In lithostratigraphic Unit I, from 0 to 175 mbsf (down to Core 146-888B-19X), recovery was excellent, and drilling disturbance was light to moderate. Bedding attitudes are consistently horizontal to subhorizontal. Deviations up to 20° from horizontal are present sporadically; however, they are never consistent for more than 1 m and are attributable to drilling-related deformation. Alternatively, they could be explained by gravitational sediment slumping. No indication of core-scale slump folding or extension (such as vein structure) was noted, nor is there any indication of the existence of a significant paleoslope. The present seafloor slopes 0.3° to 1.5° (Davis et al., 1987).

Poor recovery and fluidization of sandy intervals hampered structural evaluation of the transition zone, from 175 to 193 mbsf, and Unit II, from 193 to 457 mbsf (Cores 146-888B-20X to -52X). Where

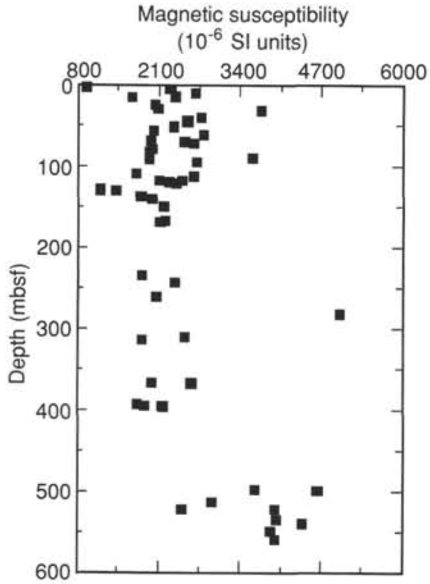

Figure 29. Plot of mean susceptibility vs. depth (mbsf) for Hole 888B.

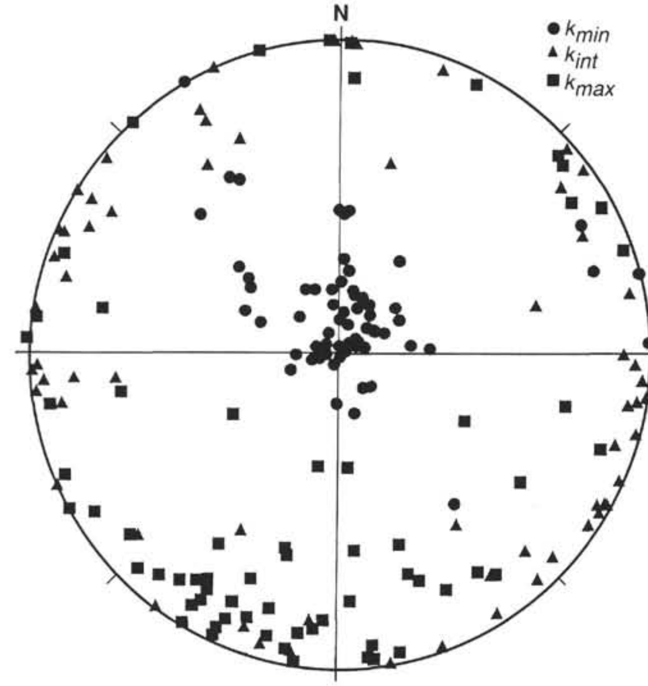

Figure 30. Equal-area, lower hemisphere projection of AMS axis orientations from Hole 888B. The circles represent the minimum susceptibility axis, the triangles the intermediate axis, and the squares the maximum axis. The AMS orientations correspond to a subhorizontal, planar-preferred orientation of magnetite in these samples.

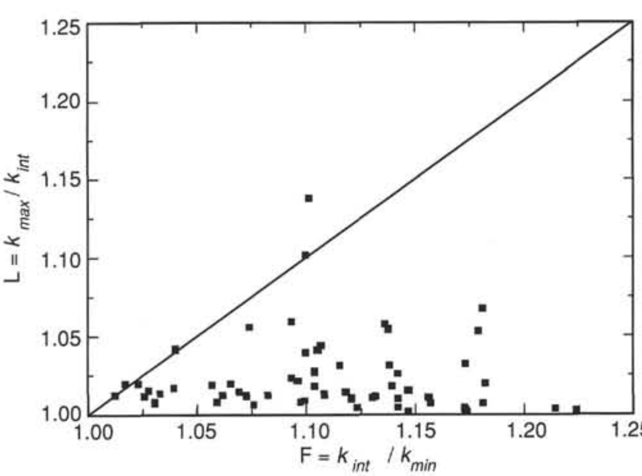

Figure 31. Flinn-type diagram of the AMS ellipsoid shape. The vertical axis is the magnetic lineation, the horizontal axis is the magnetic foliation. Results plotting in the upper-left portion of the diagram have prolate susceptibility ellipsoids; results plotting in the lower-right portion of the diagram have oblate susceptibility ellipsoids. Almost all of the Hole 888B samples have oblate ellipsoid shapes, indicating a predominantly planar-preferred orientation for magnetite in these rocks.

discernible, bedding attitudes were subhorizontal, deviating less than 10° from horizontal in all cases (see Fig. 77). Most of the recovered material preserved no internal structure.

Although recovery improved in Unit III, from 452 to 567 mbsf (Cores 146-888B-52X to -65X), and especially in Subunit IIIB, the cores continued to be subjected to severe drill disturbance, including fluidization, flow of sediment into the core barrel (flow-in), and drill biscuiting, which destroyed most of the original structure in the sediments. Subhorizontal to shallowly dipping bedding was observed, with dips up to 20° and no consistent orientation. Attitudes that did deviate from horizontal were not clearly attributable to tectonic deformation and occurred in intervals with significant drilling disturbance. Core-scale (<5 cm limb-to-limb) tight recumbent to inclined folds were observed in Sections 146-888B-62X-CC and -65X-CC; it is unclear whether these represent drilling deformation or slump folding, but they do not appear to be evidence of tectonic contraction, based on their isolation and the nonfolded nature of adjacent bedding. Cores of Subunit IIIB exhibit an incipient fissility in the clayey silts, which we interpret as a gravitational compaction fabric (Lundberg and Moore, 1986), but which also may have been produced or enhanced by drilling-induced vertical stress cycling.

Anisotropy of magnetic susceptibility (AMS) measurements of the preferred orientation of magnetite (see "Paleomagnetism" section, this chapter) were made on discrete paleomagnetic samples taken from intact, undisturbed intervals of Hole 888B. The orientations of the principal susceptibility axes (Fig. 30) are consistent with the horizontal to subhorizontal bedding structures observed in the Hole 888B cores. The shape of the susceptibility ellipsoid is oblate (Fig. 31), with a nonsystematic downhole variation in degree of fabric anisotropy. These oblate, subhorizontal fabrics are most likely the product of gravity settling and/or sediment compaction, with possible drill-fabric overprints, as described previously.

In summary, no unequivocal evidence for tectonic deformation was found at Site 888. Drilling disturbance apparently accounts for all deviations from horizontal bedding. From the structural point of view, Site 888 does indeed represent a true reference site.

ORGANIC GEOCHEMISTRY

Overview

The turbidite sequences cored at Site 888 have interbeds of sand and clay that are relatively low in organic carbon (0.2%–0.4%) and in extractable bitumen or pyrolyzable kerogen. However, sufficient labile material was available to permit the exhaustion of dissolved sulfate by 200 mbsf. The predominantly methane hydrocarbon gas contents are in the 0–5 ppmv level in the sulfate reduction zone, but rise steadily to moderate levels in the lower half of the hole. Considerable scatter exists in the gas data on account of the poor core recovery, particularly in Units II and III. Higher hydrocarbon gases (ethane, propane, butane) are present in only trace amounts ($C_1/C_2 > 10^3$), indicating that the methane is of bacterial origin.

Two interesting anomalies of methane gas are recorded at Site 888. The first, at 94 mbsf, is a local (about 10 m thick) occurrence of bacterial methane that corresponds to a local sulfate depletion and total bicarbonate increase. This is an active methanogenic/methylotrophic microsystem that maintains non-steady-state dissolved-nutrient profiles (see "Inorganic Geochemistry" section, this chapter). The second anomaly of higher methane gas contents (68,000 ppmv) at 351 mbsf is in a high-porosity and high-permeability sand layer. This zone may act as a conduit for the lateral transport of gas into Site 888.

Organic Carbon

Organic carbon contents (C_{org}) are relatively low at Site 888 (Table 5). In Unit I (i.e., <175 mbsf), C_{org} fluctuates at about 0.4 wt%, except in the sample closest to the surface (Sample 146-888B-1H-2), which has 0.99 wt% (Fig. 32). In Unit II, C_{org} drops steadily to less than 0.2 wt% by 200 mbsf and remains low to 400 mbsf. Across the Unit II/III boundary, C_{org} increases up to about 0.4 wt% at the base of Subunit IIIA. Organic carbon values of 0.4–0.6 wt% were recorded in Subunit IIIB.

The C_{org} values are typical of those for the surface sediments of Cascadia Basin and are consistent with rapid turbidite-hemipelagite deposition. Wood fragments (see "Lithostratigraphy" section, this chapter) were reported in several cores. Lithostratigraphic unit boundaries correspond to boundaries between the low and moderate carbon environments, as illustrated in Figure 32.

The carbonate contents at Site 888 vary from 0.25 to 4.58 wt% (Fig. 32 and Table 5). There is no apparent correlation between the organic and inorganic carbon.

Total Nitrogen

The total nitrogen (N_{tot}) varies in sympathy with the organic carbon contents in Hole 888B (Table 5). The lowest values of N_{tot} were recorded in Unit II (below the detection limit), whereas Units I and III have values around 0.04 wt% (Fig. 32). Similar to C_{org}, a higher N_{tot} content (0.08 wt%) was recorded at the surface of Hole 888B. The highest value was 0.09 wt% at 470.7 mbsf, which is also a C_{org} maximum. The correspondence of N_{tot} with C_{org} contents is illustrated in Figure 33. The regression gives a C/N ratio of about 10:1, which is indicative of a mixed marine/terrestrial organic source, the former richer in nitrogen. The considerable degree of scatter observed in the C/N ratio in Figure 33 is a result of the variation in the lithologies drilled.

Total Sulfur

Total sulfur (S_{tot}) in Site 888 is consistently less than 0.4 wt% (Table 5). The S_{tot} decreases steadily from near 0.4 wt% at the surface to values less than 0.1 wt% by 100 mbsf (Fig. 32). Below 200 mbsf, the S_{tot} varies at about 0.1 wt% to total depth.

Headspace Hydrocarbon Gases

Concentrations of hydrocarbon gases in the headspace at Site 888 are relatively low except for a single high value of 27,698 ppmv at 351 mbsf (Table 6). Generally, the methane distribution can be separated into two or perhaps three major depth zonations (Fig. 34). Except for three samples between 87.5 and 94 mbsf, the methane contents in Unit I and the uppermost portion of Unit II from Hole 888B are at background levels (i.e., <5 ppmv). Below 185 mbsf the methane content increases irregularly down to approximately 440 mbsf, then appears to decrease somewhat with further depth. Poor sample recovery in Units II and III significantly influenced the quality of the headspace measurements, but the general trends can be recognized.

Higher hydrocarbon gases are present in only trace amounts for most of Hole 888B (i.e., <1 ppmv) (Table 6). At total depth the amount of ethane has risen to only 2.2 ppmv. The methane/ethane (C_1/C_2) ratios calculated for the lowermost six cores (Samples 146-888B-60X-1 through -65X-4) fall from 8369 to 815 (Fig. 35).

Vacutainer Gas

Five vacutainer samples taken at Site 888 show a trend similar to that seen in the headspace gas analyses. The uppermost two samples at 271.82 and 319.01 mbsf (Table 7) are in the zone with lower methane contents. The lower three samples, at 398.89, 401.44, and 535.79 mbsf, all have higher methane contents (up to 59 vol%). The C_1/C_2 ratio reflects the increase in methane in the lower part of Hole 888B.

Kerogen Analysis

The Geofina hydrocarbon meter (GHM) pyrolysis returned low S_1 and S_2 counts (Table 8). This result is consistent with the low organic carbon contents and indicates that the organic matter is

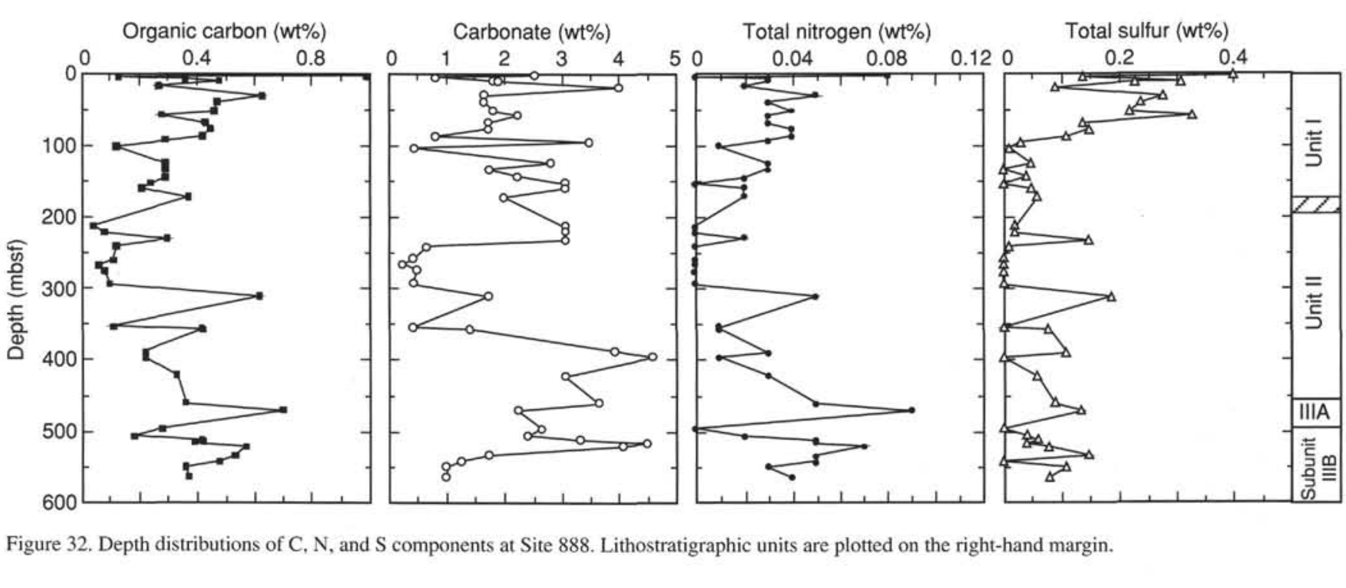

Figure 32. Depth distributions of C, N, and S components at Site 888. Lithostratigraphic units are plotted on the right-hand margin.

Table 5. Carbon, nitrogen, and sulfur sediment data (based on total dry sediment), Site 888.

Core, section, interval (cm)	Depth (mbsf)	Inorganic carbon (wt %)	$CaCO_3$ (wt%)	Total carbon (wt%)	Organic carbon (wt%)	Total nitrogen (wt%)	Total sulfur (wt%)
146-888B-							
1H-2, 143–145	2.9	0.31	2.58	1.30	0.99	0.080	0.399
1H-3, 105–110	4.0	0.10	0.83	0.23	0.13	0.002	0.137
2H-2, 145–150	8.5	0.23	1.92	0.59	0.36	0.025	0.306
2H-2, 53– 58	9.1	0.22	1.83	0.70	0.48	0.034	0.229
3H-3, 145–150	18.0	0.48	4.00	0.75	0.27	0.022	0.085
4H-4, 145–150	30.4	0.20	1.67	0.83	0.63	0.047	0.276
5H-4, 143–150	39.9	0.20	1.67	0.67	0.47	0.028	0.239
6H-5, 140–150	50.9	0.22	1.83	0.68	0.46	0.037	0.221
7H-3, 140–150	57.4	0.27	2.25	0.55	0.28	0.033	0.326
8H-4 140–150	68.4	0.21	1.75	0.64	0.43	0.030	0.144
9H-3, 140–150	76.4	0.21	1.75	0.66	0.45	0.035	0.154
10H-4, 140–150	87.4	0.10	0.83	0.52	0.42	0.035	0.113
11H-3, 142–152	95.3	0.42	3.50	0.71	0.29	0.027	0.031
12H-2, 139–149	103.4	0.05	0.42	0.17	0.12	0.007	0.010
14H-4, 138–150	124.0	0.34	2.83	0.63	0.29	0.026	0.049
15H-4, 138–150	133.5	0.21	1.75	0.50	0.29	0.030	0.000
16H-5, 138–150	144.5	0.27	2.25	0.56	0.29	0.022	0.040
17H-4, 140–150	152.5	0.37	3.08	0.61	0.24	0.000	0.000
18X-2, 135–150	159.0	0.37	3.08	0.59	0.22	0.015	0.048
19X-5, 0–15	171.6	0.24	2.00	0.61	0.37	0.018	0.059
24H-1 135–150	214.3	0.37	3.08	0.41	0.04	0.000	0.024
25H-3, 135–150	221.8	0.37	3.08	0.45	0.08	0.000	0.023
26H-3, 135–150	231.3	0.37	3.08	0.67	0.30	0.021	0.153
27H-5, 140–150	241.6	0.08	0.67	0.20	0.12	0.000	0.005
29H-5, 130–150	259.1	0.05	0.42	0.16	0.11	0.002	0.000
30H-4, 130–150	266.6	0.03	0.25	0.09	0.06	0.001	0.000
31H-5, 130–150	275.1	0.06	0.50	0.15	0.09	0.004	0.000
34H-1, 130–150	293.7	0.05	0.42	0.15	0.10	0.001	0.000
36H-2, 70–80	312.2	0.21	1.75	0.83	0.62	0.050	0.187
40H-5, 130–150	355.3	0.05	0.42	0.16	0.11	0.005	0.000
41X-1, 54–74	357.5	0.17	1.42	0.59	0.42	0.011	0.080
44X- 0-4–15	389.5	0.47	3.92	0.69	0.22	0.029	0.107
45X- 135-1–150	396.4	0.55	4.58	0.77	0.22	0.014	0.000
48X-CC, 0–5	423.5	0.37	3.08	0.70	0.33	0.029	0.055
53X-CC, 3–18	460.5	0.44	3.67	0.80	0.36	0.052	0.093
54X-1, 130–150	470.7	0.27	2.25	0.97	0.70	0.091	0.137
57X-1, 135–150	497.5	0.32	2.67	0.60	0.28	0.000	0.003
58X-3, 0–20	508.1	0.29	2.42	0.47	0.18	0.018	0.042
59P-1, 2–14	514.0	0.40	3.33	0.82	0.42	0.050	0.055
60X-1, 30–40	516.3	0.54	4.50	0.93	0.39	0.048	0.041
61X-1, 1–10	522.8	0.49	4.08	1.06	0.57	0.065	0.078
62X-2, 130–150	534.5	0.21	1.75	0.74	0.53	0.052	0.154
63X-2, 130–150	543.2	0.15	1.25	0.63	0.48	0.052	0.000
64X-1, 130–140	550.5	0.12	1.00	0.48	0.36	0.034	0.105
65X-5, 0–25	564.1	0.12	1.00	0.49	0.37	0.038	0.079

refractory and reflects the terrigenous input. Examples of pyrolysis runs (Fig. 36) show the low hydrocarbon recovery and the difficulty in estimating the T_{max} value. There appears to be a general depth trend to lower S_1 and S_2, and perhaps a slight shift in T_{max} to higher values at greater depth.

Bitumen Analysis

Sixteen samples were extracted as described in the "Explanatory Notes" chapter (this volume). No fluorescence was visible in any of the samples. This indicates that the samples are of low rank and dominated by more refractory material, in agreement with the kerogen analyses.

The high-resolution C_{11}–C_{40} gas chromatography of the hexane-soluble fraction revealed that most of the original labile hydrocarbons in the organic matter, such as the *n*-alkanes and isoprenes, had been lost, probably through biodegradation. The more prominent peaks do not correspond to common alkanes, and shore-based gas chromatography-mass spectrometry is required for compound identification. The residual bitumen present is an unresolved complex mixture (UCM) of extractable material. Maturation of the organic matter has been insufficient to generate significant amounts of thermogenic products. Examples of typical C_{11}–C_{40} gas chromatograms in Figure 37 illustrate the highly degraded nature of the hydrocarbons in the extracts. The prominence of the UCM between C_{17} and C_{23} compounds is typical for alteration products of marine microbial lipids (Simoneit, 1977, 1978). Some of the higher molecular weight compounds (>C_{24}) could reflect the waxy, terrigenous input. The C_{37}–C_{39} alkenones (Fig. 38) were poorly resolved and determination of U^{k}_{37} (e.g., Volkman et al., 1980; Marlowe et al., 1984) was not made, nor could reliable carbon preference indices or pristane/phytane ratios be calculated.

Preliminary Interpretation

Some interesting geochemical features are present in Hole 888B. The hydrocarbons present are most certainly of bacterial origin, which is consistent with surficial cores analyzed by Whiticar (1990) at the Cascadia Margin. Several lines of evidence for the bacterial gas interpretation are available, but final confirmation awaits shore-based stable isotope measurements of the hydrocarbons and dissolved bicarbonate. Dry gases in this geologic setting (i.e., gases with essentially only methane present) are typically the result of methanogenesis (Claypool and Kaplan, 1974; Suess and Whiticar, 1989; Whiticar and Suess, 1989). Coal gases, which are also methane rich, are unlikely here, and no compelling evidence exists for abiogenic gases at this site. The strongest evidence for methanogenesis comes from the intimate, diagenetic relationship between dissolved sulfate and methane. Figure 39 illustrates the well-established principles of diagenetic succession in marine sediments. Available free oxygen and reducible nitrogen, iron, and manganese oxides are consumed in the uppermost

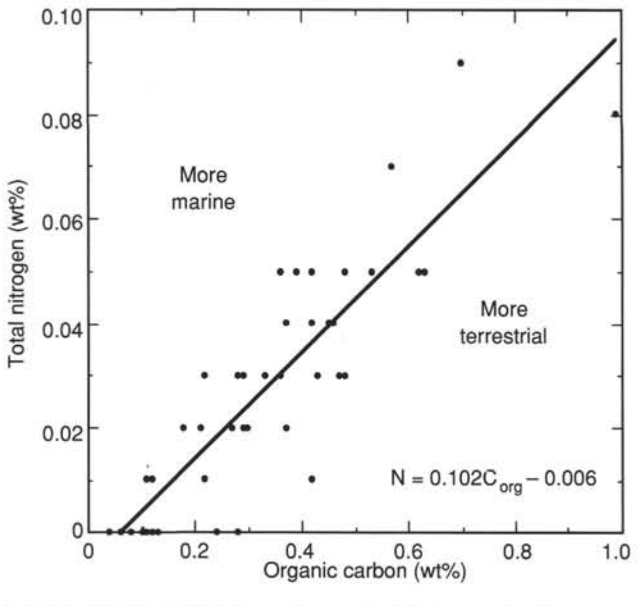

Figure 33. Cross plot of organic carbon and total nitrogen showing a strong terrestrial-hemipelagic influence at Site 888.

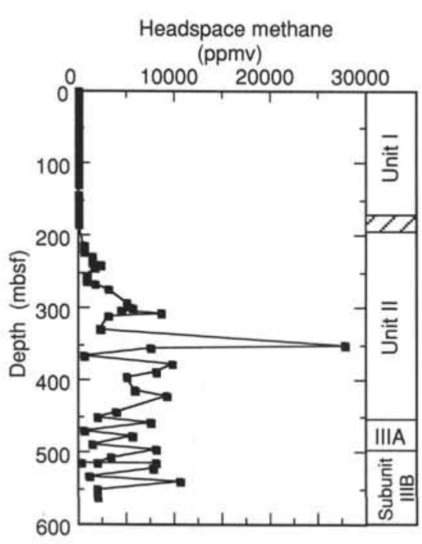

Figure 34. Depth distribution of total headspace methane at Site 888.

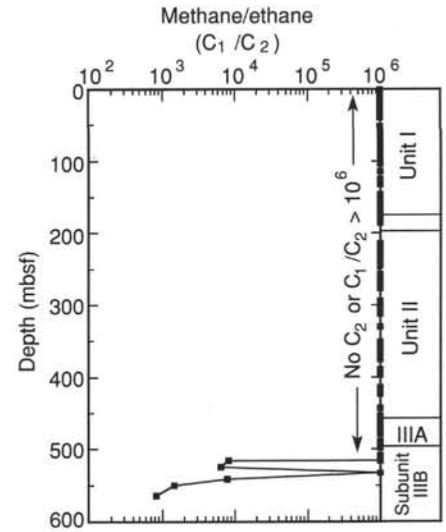

Figure 35. Depth distribution of total headspace methane/ethane (C_1/C_2) at Site 888.

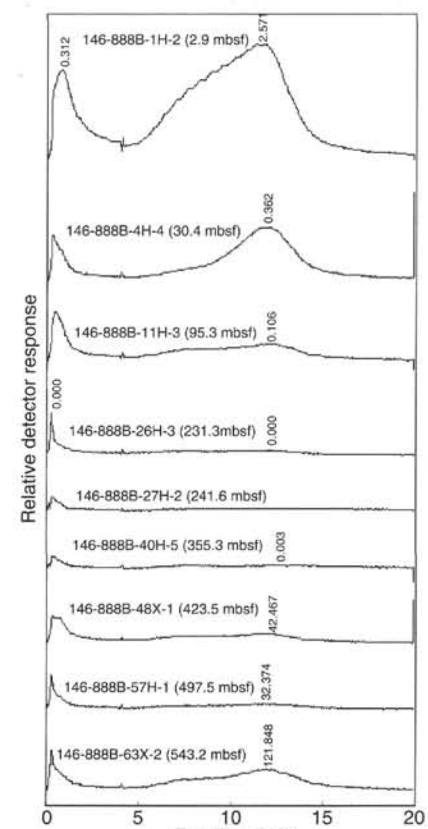

Figure 36. Examples of GHM pyrograms at Site 888.

meters of sediment by bacteria to oxidize labile organic matter. Bacterial sulfate reduction follows immediately and at Site 888 is under way in the first core processed. Sulfate exhaustion is recorded at about 210 mbsf and sulfate remains absent down to the bottom of the hole (see "Inorganic Geochemistry" section, this chapter). Corresponding to the complete removal of sulfate is the appearance of significant amounts of methane. This spatial separation, between the sulfate-reducing bacteria (SRB) and the methanogens, occurs because the SRBs effectively outcompete the methanogens in the presence of dissolved sulfate for the available hydrogen (Daniels et al., 1980). Methane transported upward by advection or diffusion into the sulfate zone is anaerobically consumed, maintaining the low methane levels above 210 mbsf. Some minor methanogenesis can occur in the sulfate zone by noncompetitive substrates (Oremland et al., 1988; Zehnder, 1988), but this is quickly recycled by bacterial consumption.

The primary pathway of methanogenesis in marine sediments is CO_2 reduction (Claypool and Kaplan, 1974; Whiticar et al., 1986), and this is perhaps expressed by the general decrease in total dissolved CO_2 (ΣCO_2) below 210 mbsf, as shown in Figure 39. In the lower cores of Unit II and in Unit III, both ammonia and phosphate also decrease (see "Inorganic Geochemistry" section, this chapter), so that the lowering of alkalinity may also be the result of a decrease in useable organic matter and not solely the result of methanogenesis. Shore-based stable carbon isotopes of dissolved ΣCO_2 should be able to resolve this point.

The first of the two intriguing anomalies in Hole 888B occurs in Samples 146-888B-10H-5 through -11H-3 (87.5–94 mbsf). In an other-

Table 6. Molecular composition of headspace gases at Site 888.

Core, section, interval (cm)	Depth (mbsf)	C_1	CO_2	C_2	C_3	C_1/C_2
146-888B-						
1H-1, 5–55	0.30	8.5	373.0			U/D
1H-1, 58–108	0.83	1.0	158.0			U/D
1H-1, 111–161	1.36	6.5	433.0			U/D
1H-2, 164–214	3.39	1.0	2.1			U/D
1H-3, 0–5	3.03	3.2	4954.0			U/D
1H-3, 50–53	3.52	3.8				U/D
2H-4, 50–53	10.52	5.0	3733.0			U/D
2H-6, 0–5	13.03	10.0	94.7			U/D
3H-5, 0–5	21.03	3.0	1385.0			U/D
4H-5, 0–5	30.53	3.9	96.4			U/D
5H-5, 0–5	40.03	2.5	3.4			U/D
6H-6, 0–5	51.03	1.8	8.5			U/D
7H-5, 0–5	59.03	4.3	51.7			U/D
8H-5, 0–5	68.53	4.0				U/D
9H-4, 0–5	76.53	1.0	2473.0			U/D
9H-4, 147–150	77.99	1.0	5.3			U/D
10H-5, 0–5	87.53	82.8	4795.0			U/D
11H-2, 0–5	92.53	116.3	1384.0			U/D
11H-3, 0–5	94.03	91.2	5156.0			U/D
12H-3, 0–5	103.53	4.3	9014.0			U/D
13H-4, 0–5	113.13	1.0	81.6			U/D
14H-5, 0–5	124.13	1.0	4744.0			U/D
15H-3, 0–5	130.63	1.0	77.0			U/D
16H-6, 0–5	144.63	1.0	1279.0			U/D
17H-5, 0–5	152.63	1.8	63.2			U/D
18X-5, 0–5	162.13	1.0				U/D
19X-5, 0–5	171.63	1.0	493.0			U/D
20X-1, 0–5	175.13	3.6	190.0			U/D
21X-1, 0–2	184.61	28.7				U/D
24H-2, 0–5	214.43	438.4	419.0			U/D
25H-4, 0–5	221.93	444.0	3640.0			U/D
26H-2, 0–5	228.43	1466.0	48.8			U/D
26H-4, 0–5	235.93	1333.7	1025.0			U/D
27H-5, 0–5	240.23	2341.5	76.5			U/D
28H-2, 0–5	244.83	1640.7	3327.0			U/D
29H-4, 0–5	256.33	921.8	941.0			U/D
30H-1, 145–150	262.28	4093.0				U/D
30H-5, 0–5	266.83	1737.0	4062.0			U/D
31H-6, 0–5	275.33	2957.4	3667.0			U/D
34H-1, 127–130	293.59	5023.0	1107.0			U/D
34H-5, 0–5	298.33	5690.0	1236.0			U/D
35H-4, 0–5	305.03	4422.0	2129.0			U/D
35H-5, 0–5	306.53	8488.0	2955.0			U/D
36H-2, 65–70	312.18	3108.0	51.0			U/D
37H-7, 36–40	328.88	2132.0	3070.0			U/D
40H-3, 0–5	351.03	27698.0	2331.0			U/D
41X-1, 0–5	357.03	7365.0	56.0			U/D
42X-1, 2–3	366.53	675.0	1581.0			U/D
43X-1, 0–5	376.03	9737.0	1058.0			U/D
44X-3, 145–150	389.98	5381.0				U/D
45X-2, 0–5	396.53	1129.0				U/D
47X-1, 0–2	414.01	4012.0				U/D
48X-1, 0–5	423.53	6002.0				U/D
50X-1, 20–24	442.72	80.0				U/D
52X-1, 20–25	452.33	1901.0	68.0			U/D
53X-1, 48–53	461.01	7366.0	6.0			U/D
54X-2, 0–5	470.93	619.0				U/D
55X-1, 0–5	478.43	5490.0	1888.0			U/D
56X-1, 40–45	487.73	1278.0				U/D
57X-1, 137–140	497.59	7919.0	62.1			U/D
58X-2, 145–150	508.08	3215.0	1.5			U/D
59P-1, 0–5	514.03	1923.0				U/D
59P-1, 47–48	514.48	415.0	155.0			U/D
60X-1, 0– 5	515.03	7959.0		1.0		8369
61X-1, 145–150	523.98	7854.0		1.2		6518
62X-2, 0–5	533.23	1162.0	37.0			U/D
63X-2, 0–5	541.93	10685.0	2616.0	1.4		7839
64X-2, 0–5	550.73	1824.0		1.3		1436
65X-4, 145–150	564.08	1825.0		2.2	1	815

Note: C_X = *n*-alkanes, iC_X = iso-alkanes, nC_X = normal alkanes, and U/D = $C_1/C_2 > 10^6$. Values reported as a relative volume (ppmv) of total gas present in headspace vial.

wise methane-barren Unit I, methane rises sharply in this interval to 116 ppmv, as shown in Figure 40. Maintenance of this steep methane gradient mandates that locally active methanogenesis be present. This methane formation is strongly restricted to this zone. The sulfate-methanogenic relationship, discussed in the preceding, is not violated by this anomaly. In fact, sulfate is also locally exhausted in this interval (Fig. 40). Methane transported away from this interval is

Table 7. Molecular composition of vacutainer gases at Site 888.

Core, section, interval (cm)	Depth (mbsf)	C_1	CO_2	C_2	C_3	nC_4	nC_5	nC_6	C_1/C_2
146-888B-									
31H-3, 100–103	271.82	66	55.1	2	1	10	2	1	39.7
36H-7, 0–1	319.01	50	373.0						U/D
44H-3, 38–39	398.89	586879	95.0	15	3				40005.4
44H-4, 143–144	401.44	173705	1600.0	3					51089.7
62H-3, 108–109	535.79	450158	9.1	24	1				19098.8

Note: C_X = *n*-alkanes, iC_X = iso-alkanes, nC_X = normal alkanes, and U/D = $C_1/C_2 > 10^6$. Values reported as a relative volume (ppmv) of total gas present in the vacutainer.

rapidly consumed by anaerobic oxidation. Sulfate reduction adjacent to this interval is sufficiently intense to ensure the low-sulfate conditions. Any explanation for this local, non-steady-state condition involves bacterial activity. Two possibilities for the diagenetic aberration at this point are (1) the lateral influx of methane and (2) local methanogenesis.

The lateral influx of methane could lead to a substantial removal of sulfate as a result of methane oxidation. Once the available sulfate is removed, then in-situ methanogenesis can continue. The methane influx could trigger the sulfate depression in what would otherwise be a continual sulfate removal profile from the surface to 210 mbsf. Support for this possibility comes from the sharp increase in alkalinity up to 33 mM in this interval (Fig. 40; see also "Inorganic Geochemistry" section, this chapter). Downward and upward diffusion of sulfate into the methane zone creates the "valley-type" sulfate distribution. An argument against the possibility of lateral methane migration is that in this interval the lithology of the sediment is more clay rich than in the adjacent sections (see "Lithostratigraphy" section, this chapter).

Local methane formation also would be a reasonable explanation for the methane anomaly between 87.5 and 94 mbsf. However, this scenario would require an (organic carbon) accumulation discontinuity at about 90 mbsf. Without this discontinuity, there is no particular reason for the exhaustion of sulfate at this depth, followed by its recurrence farther downhole. Similarly, without an accumulation discontinuity no particular, compelling reason exists for a triggering of methanogenesis. In this accumulation discontinuity scenario, normal diagenesis with sulfate reduction was proceeding at the time that the interval represented by Core 146-888B-12H was at or near the surface. A sudden event, in which the deposition of more labile organic matter was followed by rapid burial, could have led to an isolated sediment package that would have locally enhanced reducing conditions and therefore produced "premature" methanogenesis. The methane gradient would be maintained by continued methanogenesis coupled with sulfate reduction to consume the methane. As would be the case also with the lateral influx of methane, the sulfate and alkalinity profiles would be generated by diffusion and regenerated bicarbonate, respectively. Arguments for the accumulation discontinuity scenario include the elevated ammonia and phosphate levels in this interval (see "Inorganic Geochemistry" section, this chapter), whereas a strong counter argument is that the organic carbon contents of this section (Fig. 32) are not distinctive. Some wood fragments were recovered, but their substrate potential is poor. A higher hexane-extractable bitumen recovery was seen at Sample 146-888B-11H-3 (95.3 mbsf), but this is probably indicative of the active microbial communities in this interval, not enhanced substrate content.

Shore-based microbiological and stable isotope measurements may help to resolve which of these two possible mechanisms accounts for the methane/sulfate anomaly.

The second of the two intriguing anomalies in Hole 888B is the methane peak of 27,698 ppmv at 351 mbsf (Fig. 34). In this instance, a stronger possibility exists for lateral influx of methane into the section. The lithology is a high-porosity, permeable coarse sand that expelled gas and sediment as the core was split. Little organic matter is present in the section (0.11 wt%), so there would not be much substrate potential for methanogens and in-situ methanogenesis. Fur-

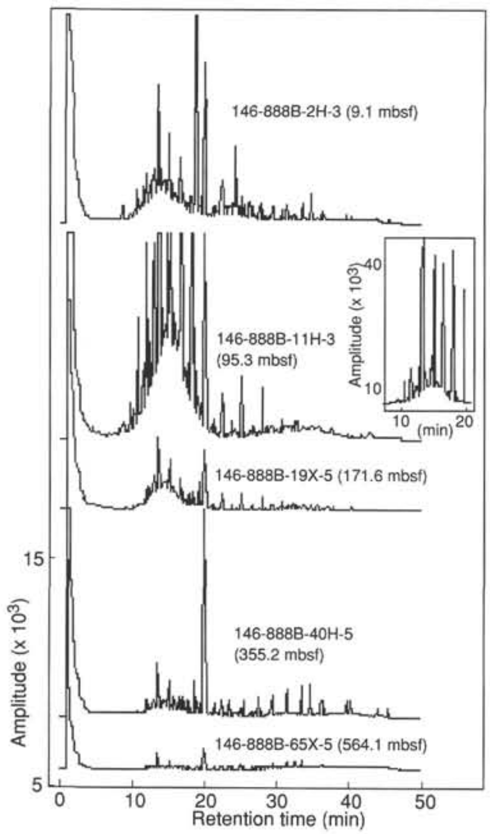

Figure 37. Examples of typical C_{11}–C_{40} gas chromatograms at Site 888.

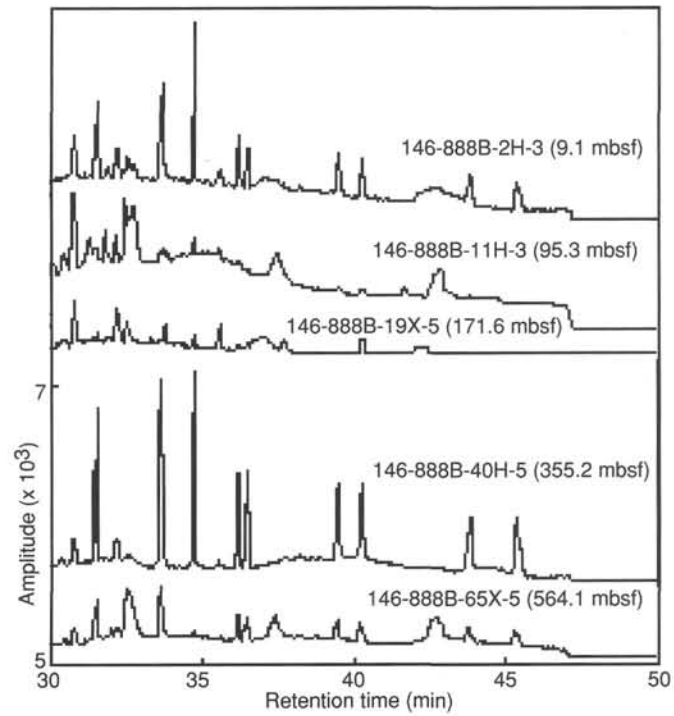

Figure 38. Examples of typical C_{23}–C_{40} gas chromatograms ("alkenone fraction") at Site 888.

thermore, the steep methane-content gradient across this interval would be difficult to maintain if an active influx of gas was not available. It is uncertain what the bounding lithologies are, because of the poor core recovery both above and below the gassy interval, but they are probably intercalated clays and sands. A tentative sulfate value in Sample 146-888B-40H-5 of 4.1 mM (see "Inorganic Geochemistry" section, this chapter) is unusual for this reducing environment. This sulfate value may be caused by the mixing of seawater—the core recovery was poor and this finding is not supported by the other dissolved interstitial-fluid constituents—but if it is not caused by mixing, then it could be additional evidence of lateral fluid flow in this reference site on the Cascadia Margin.

INORGANIC GEOCHEMISTRY

Introduction

A primary goal at Site 888 was to acquire a complete reference data set of the fluid geochemistry away from influences of the accretionary wedge. However, many "unusual" characteristics of interstitial-fluid chemistry exist in Hole 888B, which may reflect fluid flow within the section or from the adjacent Nitinat Fan deposits or the accretionary wedge. Hole 888B may have been drilled too close to the accretionary wedge to serve as a true reference site, but it does give insights into the possible relations between fluid flow and lithology.

The constituents analyzed on-board ship are shown in Table 9. Some constituents show clear trends in concentration with increasing depth, with important local maxima or minima superimposed (Fig. 41). Chloride concentrations show a rapid downhole increase near the surface, then a broad minimum zone centered near 250 mbsf, and higher values in Subunits IIIA and IIIB, with one distinct minimum at 514 mbsf. Sulfate is present in the upper 210 mbsf, but it is completely reduced below this depth. Alkalinity increases sharply to 100 mbsf, but generally shows higher concentrations in Unit II than in Unit III or in the top part of Unit I. Ammonium and phosphate concentrations generally exhibit the highest values in Unit II (Fig. 41). Calcium concentrations generally decrease to a broad minimum near 300 mbsf, then abruptly increase to the bottom of the hole. Magnesium concentrations generally decrease with depth, but the Mg/Ca ratio first increases and below 300 mbsf decreases with depth. Potassium concentrations decrease to about 150 mbsf, then increase to a broad maximum near 350 mbsf, and decrease to the bottom of the hole (Fig. 41). Silica concentrations show high variability that is probably dependent on changes in lithology, but silica concentrations generally decrease to 100 mbsf, then increase to about 400 mbsf. Below this depth, more irregular fluctuations in silica concentration exist that may reflect local diagenetic reactions.

Important Features of the Profiles

Although details of the concentration profiles are described subsequently, some important features are summarized here. Chloride concentrations rapidly increase from 543 mM near the surface to 571 mM at 70 mbsf (Fig. 41 and Table 9). The low values just below the

Table 8. Results of Geofina hydrocarbon meter pyrolysis at Site 888.

Core and section	S_1 (mgC/g)	S_2 (mgC/g)	T_{max} (°C)
146-888B-			
1H-1	0.32	1.43	495
4H-4	0.08	0.50	498
11H-3	0.09	0.18	504
26H-3	0.03	0.03	496
27H-5	0.01	0.02	532
40H-5	0.01	0.02	?
48X-CC	0.05	0.08	499
57X-1	0.03	0.04	487
63X-2	0.06	0.27	495

Table 9. Interstitial-water chemical data, Hole 888B.

Core, section, interval (cm)	Depth (mbsf)	Water (mL)	pH	Alkalinity (mM)	Salinity (g/kg)	Cl^- (mM)	Mg^{2+} (mM)	Ca^{2+} (mM)	Mg/Ca	SO_4^{2-} (mM)	PO_4^{3-} (μM)	NH_4^+ (μM)	SiO_2 (μM)	K^+ (mM)
146-888B-														
1H-2, 143–150	2.9	60	7.8	6.72	35.0	545	51.41	10.26	5.0	25.37	42.90	368	733	12.83
1H-3, 105–110	4.0	4			35.0	546	52.18	10.30	5.1	23.95	38.40	472	516	12.12
2H-2, 140–150	8.5	50	7.9	11.47	35.7	552	53.12	11.47	4.6	22.44	47.40	668	683	10.74
2H-3, 53–58	9.1	34	7.7	12.35	35.8	551	52.42	11.67	4.5	21.56	20.40	757	576	10.33
3H-2, 145–150	18.0	48	7.8	14.10	36.0	562	56.03	12.13	4.6	18.76	3.60	895	556	8.18
4H-4, 143–150	30.4	36	7.8	13.81	35.5	561	57.72	12.37	4.7	20.79	15.90	791	535	7.26
5H-4, 143–150	39.9	33	7.9	12.11	36.0	564	59.11	12.78	4.6	21.67	19.50	719	470	7.32
6H-5, 140–150	50.9	36	7.9	14.21	35.5	565	58.32	11.77	5.0	18.45	24.90	789	634	7.21
7H-3, 140–150	57.4	60	8.0	17.20	35.0	568	57.79	10.44	5.5	15.02	14.40	1087	546	7.78
8H-4, 140–150	68.4	36	7.7	22.87	35.0	571	54.47	9.75	5.6	8.39	21.90	1443	677	7.11
9H-3, 140–150	76.4	45	8.0	27.87	35.0	559	52.37	9.21	5.7	3.18	31.80	1469	728	7.47
10H-4, 140–150	87.4	50	8.1	32.19	34.0	560	49.07	9.49	5.2	0.00	32.40	2020	637	7.26
11H-3, 142–152	95.3	48	8.2	31.62	34.5	559	51.35	8.41	6.1	0.37	30.90	1678	589	7.37
12H-2, 140–150	103.4	18	8.1	33.24	34.5	558	53.57	7.31	7.3	0.00	77.30	1479	473	12.0
14H-4, 140–150	124.0	20	8.1	17.31	34.0	556	51.94	10.22	5.1	9.97	15.90	1293	294	4.96
15H-4, 138–150	133.5	18	8.0	20.24	34.5	554	53.59	10.88	4.9	10.56	15.90	936	323	3.89
16H-5, 138–150	144.5	30	8.4	23.09	34.0	554	53.56	9.61	5.6	9.56	24.90	1038	331	3.84
17H-4, 135–150	152.5	42	8.0	23.23	34.5	553	54.13	8.24	6.6	8.26	26.40	1045	312	3.53
18X-2, 135–150	159.0	33	7.9	23.18	34.0	545	54.14	7.61	7.1	7.79	26.40	980	356	4.19
19X-5, 1–15	171.6	46		23.18	33.0	543	52.69	8.44	6.2	5.70	21.90	1306	329	4.04
24H-1, 135–150	214.3	15	8.2	23.18	33.0	552	47.15	6.79	6.9	0.15	23.40	1387	450	6.55
25H-3, 135–150	221.8	10	8.3	24.48	33.5	552	46.28	6.72	6.9	0.00	20.40	1417	454	6.29
26H-3, 135–150	231.3	30	8.3	21.44	32.5	550	43.82	6.41	6.8	0.00	27.90	1407	361	6.70
27H-5, 135–150	241.6	11	8.0	16.72	32.5	546	39.13	5.94	6.6	0.00	47.40	1776	543	6.85
30H-4, 130–150	266.6	28	8.1	17.90	32.0	547	38.43	5.76	6.7	0.00	72.80	2512	622	8.13
31H-5, 130–150	275.1	28	8.1	16.80		554	37.95	5.67	6.7	0.00	30.90	3064	566	8.34
34H-1, 130–150	293.7	20		17.68		548	40.62	6.52	6.2	0.00	41.80	2728	516	8.75
36H-2, 70–80	312.2	42		20.94	32.0	550	38.85	5.66	6.9	0.00	74.60	4030	865	6.45
40H-5, 130–150	355.3	18	8.0	25.61	31.3	552	39.79	6.46	6.2	4.13	67.20	4281	923	12.07
44X-4, 1–15	389.5	29	7.8	13.80	32.0	556	36.82	8.03	4.6	0.96	32.90	2605	799	7.67
45X-1, 135–150	396.4	19	7.9	10.46	32.0	559	36.23	8.04	4.5	0.00	9.10	2267	402	6.85
48X-CC	423.5	7			32.0	563	37.58	6.93	5.4	0.23	10.60	1878	428	6.34
53X-1, 3–18	460.5	12	8.0	16.11	33.0	563	41.12	9.10	4.5	0.00	13.50	2536	428	7.42
54X-1, 130–150	470.7	14	8.1	20.60	33.5	563	40.42	9.61	4.2	0.56	16.60	3223	846	6.29
57X-1, 130–150	497.5	32		0.00		556	36.20	12.20	3.0	0.00	9.10	2003	274	4.25
58X-3, 1–20	508.1	2.5				551	34.47	13.35	2.6	0.20	10.60	1844	254	3.94
59P-1, 2–14	514.0	16	7.9	7.51	31.5	545	34.39	13.44	2.6	0.21	15.10	2001	605	4.35
60X-1, 130–140	516.3	2			33.0	563	35.48	13.48	2.6	0.22	12.10	1851	644	4.50
61X-1, 1–10	522.8	18	8.0	7.07	32.0	556	36.65	12.46	2.9	0.00	12.10	2101	783	6.19
62X-2, 130–150	534.5	10	8.0	4.27	33.0	564	34.02	15.00	2.3	1.09	12.10	1718	299	2.81
63X-2, 130–150	543.2	18	8.0	5.35	32.0	562	32.83	16.27	2.0	0.69	0.00	1077	362	2.81
64X-1, 130–150	550.5	5			32.0	562	31.13	17.26	1.8	0.23	9.10	1267	343	2.30
65X-5, 1–25	564.1	14	8.2	5.04	32.5	562	33.08	15.89	2.1	0.26	10.60	1587	252	2.86

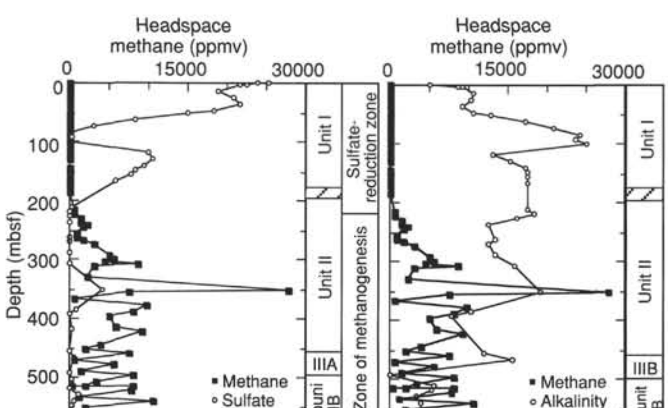

Figure 39. Depth comparison of headspace methane vs. dissolved sulfate and alkalinity at Site 888.

seafloor may be caused by low-chloride seawater in the region. Concentrations of chloride in surface seawater collected at Site 888 are 513 mM, which is significantly lower than standard seawater (IAPSO = 559 mM). Values of bottom-water chloride are not available, at this writing. The peak concentration of chloride in the upper part of the sediment (571 mM) is higher than that of average seawater. Because chloride diffuses rapidly in sediments with high pore volumes, the sharpness of the discontinuity suggests recent lateral input of high-chloride fluids at 70 mbsf. The origin of these fluids may reflect concentration of chloride resulting from hydration reactions involving volcanogenic sediments. A smaller chloride maximum occurs at 40 mbsf, which coincides with a conglomerate layer (see "Lithostratigraphy" section, this chapter) that may allow rapid flow of similar high-chloride fluids into the area of Hole 888B. Changes in other concentration profiles suggest that the origin of the high-chloride fluid is a zone of low sulfate and phosphate and high ammonium. The low sulfate suggests that the source must be deeper within the section below zones of high sulfate concentration. The origin of the fluid is probably lateral flow from out of or beneath the drilled section, because there are no sources of comparable high-chloride fluid deeper in the section (Fig. 41).

Below 70 mbsf, the changes in chloride concentrations suggest input of a different, low-chloride fluid. This is apparent in the broad chloride low that occurs within the sand-rich Unit II between about 200 and 400 mbsf (Fig. 41) (see "Lithostratigraphy" section, this chapter). Chloride concentrations reach high values (563 mM) near the top of Subunit IIIA, but a major well-developed chloride minimum occurs at 514 mbsf, which coincides with the top of a major seismic reflector (see "Seismic Stratigraphy" section, this chapter). Once again, the sharpness of this minimum indicates that flow of low-chloride fluids is active or has occurred recently. Both low-chloride intervals of the concentration profile suggest that Units I and II are affected by fluid flow from a low-chloride reservoir, which could

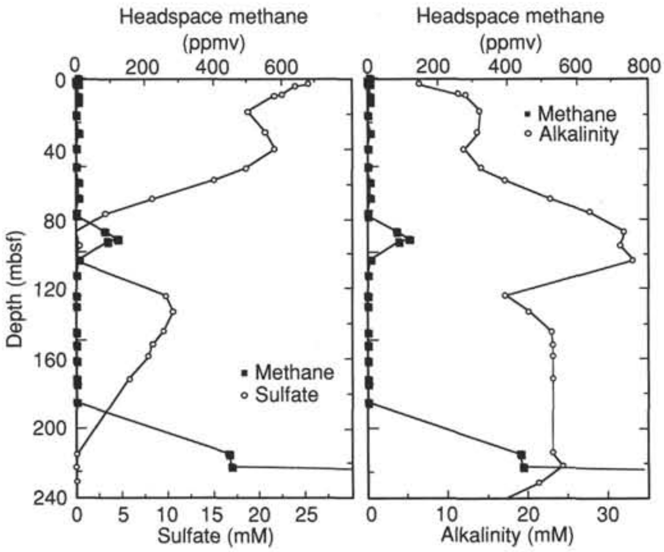

Figure 40. Comparison of headspace methane vs. sulfate and alkalinity on an expanded depth scale at Site 888.

be laterally removed from the site or located deeper within the section than that drilled at Hole 888B.

A notable feature of the interstitial-fluid chemistry is the presence of two sulfate-reduction zones, one extending from the surface to 87 mbsf and the other extending from 113 to 214 mbsf (Fig. 41). The zones are separated by a sulfate-free zone that shows a small methane peak (see "Organic Geochemistry" section, this chapter) and highs in alkalinity, ammonium, and phosphate. In the sulfate-free zone, zero sulfate concentration corresponds exactly with alkalinity and ammonium highs, whereas the methane peak coincides with a small quantity of sulfate; the presence of sulfate may represent slight contamination of the sample with seawater because methane and sulfate are incompatible in a steady-state system. This interval (87–113 mbsf) must have an active population of sulfate-reducing bacteria at its base to keep sulfate below from diffusing into the sulfate zone above and at its top to maintain the overlying sulfate-reduction profile.

In the lower part of Hole 888B (about 250 mbsf to total depth) calcium concentrations increase by over 200% whereas magnesium concentrations decrease by 30%. These changes may, in part, reflect the dolomitization of calcite, but some other process such as the alteration of volcanic matter lower in the section must be active as well.

Depth Profiles of Chemical Data

18 mbsf

At a depth of 18 mbsf chloride shows a small 1-mM maximum in a profile that otherwise steadily increases to 68.4 mbsf (Fig. 41). The chloride maximum correlates with clear maxima in alkalinity and ammonium and minima in sulfate and phosphate. These chemical features occur within a thin conglomerate layer and may suggest flow along a permeable layer. Flow may also be responsible for the rapid drop in potassium that occurs at this depth.

40 mbsf

The depth of 40 mbsf is marked by maxima in calcium, magnesium, and sulfate and minima in silica, alkalinity, and ammonium (Fig. 41). The Mg/Ca ratio shows a gradual decrease from the surface to this depth, whereas both calcium and magnesium show gradual increases. Decreases in calcium may suggest, in part, the precipitation of diagenetic carbonate at shallow levels, but such precipitation was not obvious from coulometric carbonate determinations or smear slide analyses. The silica minimum is not marked by any obvious change in lithology or biogenic silica content, but may be related to subtle changes in ash content.

70 mbsf

One of the most striking features of the concentration data at approximately 70 mbsf is the pronounced maximum in chloride content at this depth (Fig. 41). A similar but less abrupt peak was observed at shallow depths in the Nankai accretionary wedge (Shipboard Scientific Party, 1991). Fluids enriched in chloride may be derived from hydration reactions occurring in volcanic matter in the sediments. The base of the high-chloride zone is just above maxima in ammonium and silica concentrations and a minor minimum in calcium concentration. The sharp reduction in chloride concentration at greater depths suggests perturbation of the chloride profile by recent fluid influx, or by locally active hydration diagenesis. The chloride maximum coincides with two layers of thick sand (see "Lithostratigraphy" section, this chapter) that may have supported lateral fluid flow. The silica maximum may be related to a high ash content observed in samples from this depth (see "Lithostratigraphy" section, this chapter).

87–103 mbsf

The 87–103 mbsf interval is characterized by the base of the upper sulfate-reduction zone (Fig. 41), wherein sulfate is depleted and methane production begins (see "Organic Geochemistry" section, this chapter). The sulfate depletion is concomitant with a probable increase in the activity of methanogenic bacteria and an increase in alkalinity and ammonium concentration. The bottom of the interval coincides with a sharp maximum in phosphate concentration and the top of the lower sulfate-reduction zone. Potassium concentration decreases sharply across this interval. Magnesium concentration shows a small minimum at the top of the section and a maximum near the bottom, whereas calcium and silica concentrations show minima at the bottom. The Mg/Ca ratio exhibits a strong maximum in the interval as well.

The decrease in calcium concentration suggests precipitation of calcite, perhaps related to increased alkalinity. Phosphate, ammonium, and alkalinity are probably controlled by changes in the dominant active bacteria populations from sulfate-reducing to methanogenic. The lack of sulfate in this zone indicates that sulfate has not diffused from the high-sulfate zone below, suggesting that sulfate-reducing bacteria are active at the base of this interval.

103–214 mbsf

In interval 103–214 mbsf sulfate concentrations increase abruptly at the top and then gradually decrease to zero at the bottom. Phosphate and alkalinity also show marked increases in this zone, and ammonium shows only a minor increase downsection. This pattern is similar to what would be expected for near-surface zones of sulfate reduction, but it is unusual to find it repeated at a lower level.

100–420 mbsf

The interval 100–420 mbsf is notable because many constituents exhibit broad minima or maxima. Chloride shows anomalously low values at about 171 mbsf and then increases below 200 mbsf (Fig. 41). The low concentrations of chloride may correspond to movement of low-chloride fluids, but this interval does not correlate with significant changes in other chemical profiles. The very low chloride values may reflect contamination by drilling mud, but this was not recognized in other constituents. Calcium concentrations also show a broad minimum in this region, centered on about 280 mbsf. Dolomite formation could lead to the large decreases in magnesium and calcium observed. Although increases in carbonate were not observed by optical methods, additional samples have been collected for shore-

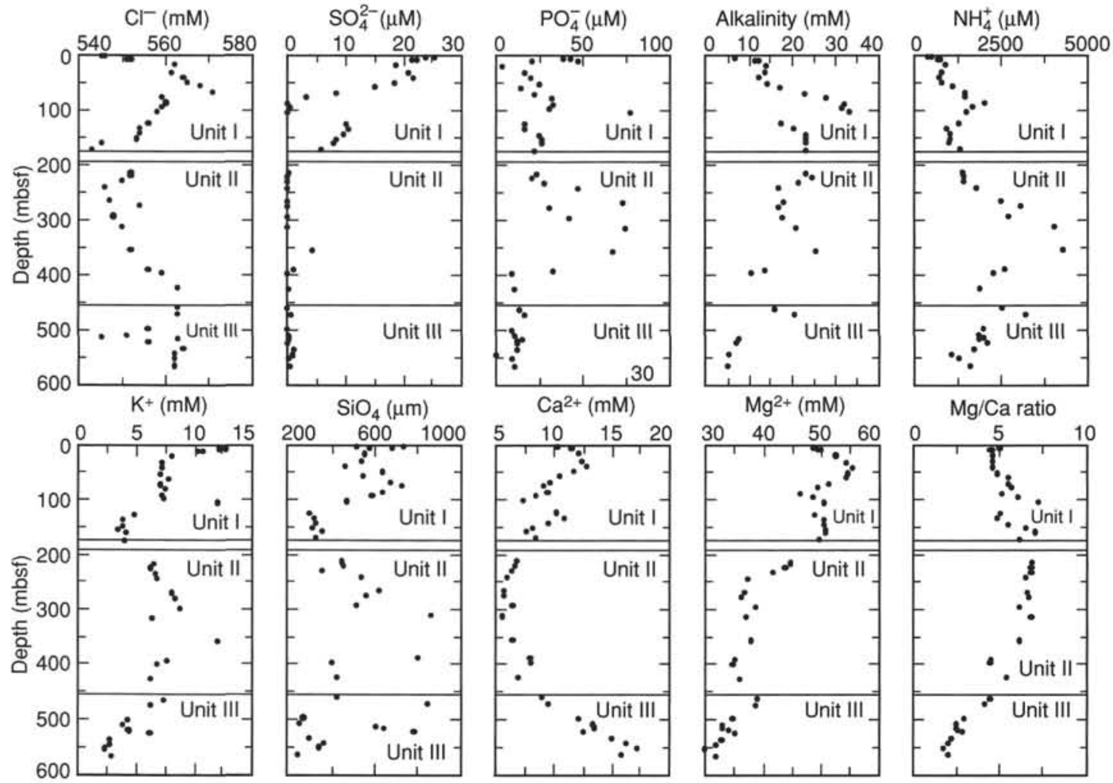

Figure 41. Concentration vs. depth profiles for chloride, sulfate, phosphate, alkalinity, ammonium, potassium, silica, calcium, and magnesium in Hole 888B. The magnesium to calcium ratio is also illustrated.

based analysis able to detect smaller diagenetic carbonate concentrations. Potassium, phosphate, and ammonium concentrations and the Mg/Ca ratio all show relative highs over this depth range (Fig. 41). Although the magnesium and calcium may reflect in large part diagenetic reactions, the low-chloride concentrations and high concentrations of the other species suggest that fluid movement may be occurring in this coarse sand interval.

450–564 mbsf

Over this interval a large decrease in magnesium and large increase in calcium were observed (Fig. 41). The Mg/Ca ratio also decreases steadily over this interval. This pattern may be characteristic of the dolomitization of calcite, but the ratio of magnesium decrease to calcium increase is not stoichiometrically correct for common dolomitization reactions, and dolomitization alone cannot account for the observed profiles. An added influence may be the low-temperature alteration of volcanic matter at depth, which typically removes magnesium from, and adds calcium to, pore fluids. Alternatively, the alteration of glass alone may account for the observed profiles. The source might be layers rich in volcanic material deeper in the sedimentary section or perhaps basaltic crust.

514 mbsf

At 514 mbsf chloride reaches a minimum of 545 mM, which is 18 mM lower than adjacent samples (Fig. 41). The minimum is abrupt and spans four interstitial-water samples, indicating that it represents a well-defined, young feature. This concentration pattern suggests recent addition of low-chloride fluid at this level. The shift is opposite to that of the chloride maximum at 70 mbsf. The chloride low corresponds to a prominent seismic reflector (see "Seismic Stratigraphy" section, this chapter), which may represent a permeable lithology.

Summary

The main processes possibly at work in Hole 888B as indicated by fluid geochemistry are:

1. Lateral influx of fluids along stratigraphic layers. The fluids at 70 mbsf are high in chloride, ammonium, and alkalinity and low in phosphate and sulfate. The fluid chemistry at 514 mbsf is more difficult to characterize because of drilling disturbance of the cores, but the fluids appear to be low in chloride and high in silica. Flow along these layers may be related to the proximity to the deformation front of the accretionary wedge, or to differential compaction associated with Nitinat Fan deposits.
2. Bacterial sulfate reduction, which leads to increased alkalinity and ammonium concentrations, and later bacterial methanogenesis, which leads to increases in methane concentrations and alkalinity.
3. Precipitation of carbonate, which leads to decreases in calcium and/or magnesium.
4. Dolomitization of calcite, which leads to increases in calcium and decreases in magnesium or only to decreases in magnesium.

PHYSICAL PROPERTIES

Introduction

The physical properties of sediments at Site 888 were measured on cores from Holes 888A and 888B. Sample recovery varied significantly throughout Hole 888B and sample quality was degraded by three coring artifacts: flow-in after partial penetration of the APC; liquefied sands; and severe shearing of XCB cores during the drilling process. Because of these factors, the physical property record is incomplete and biased toward fine-grained sediment.

Physical property variations define intervals that agree closely with the lithostratigraphic units (see "Lithostratigraphy" section, this chapter). However, finer scale variations define three zones within Unit I: Zone a (0–93.0 mbsf), Zone b (93–147 mbsf), and Zone c (147–175.1 mbsf).

Sediment physical properties measurements for Site 888 included index properties, electrical resistivity, acoustic velocity, shear strength, and thermal conductivity. The methods used for these measurements are described in the "Explanatory Notes" chapter (this volume). For Site 888, a limited subset of the multisensor track (MST) data was used for interpretation because of the poor quality of whole core collected. This section describes the variation of these physical properties within each unit and provides a preliminary comparison of three data sets: electrical resistivity to porosity, bulk density to acoustic velocity, and gamma-ray attenuation porosity evaluator (GRAPE) density to discrete bulk density.

Index Properties

Relatively high core recovery in the fine-grained sediments of Unit I (0–175.1 mbsf) allowed for measurement of a full suite of index properties within this unit. Zone a (0–93 mbsf) is dominated by thin interbedded silts, clays, and fine sand. Within this zone, water content and porosity decrease whereas bulk density increases as an exponential function of depth (Figs. 42–43 and Table 10) as expected for gravitationally compacting sediment (Athy, 1930). One interval within Zone a deviates from this trend. Between 5 and 8.5 mbsf, the porosity and water content sharply decrease with a large increase in bulk density. This deviation corresponds to a thick sandy turbidite interval.

Zone b (93.0–147.0 mbsf) within lithostratigraphic Unit I is characterized by high-amplitude variations in index properties. At the top of this interval, the bulk density is low (1.87 Mg/m^3). Over the next 11 m (to 104 mbsf), bulk density increases to 2.1 Mg/m^3. Two-and-a-half further cycles of peaks and troughs, of slightly smaller amplitude than the upper cycle, can be interpreted in the index property data to the base of this zone. These cycles of peaks and troughs in index data are associated with a series of thick deposits interpreted as turbidites.

Index property data within Zone c (147.0–175.1 mbsf) within lithostratigraphic Unit I show large variability with no clear trends. It is possible that this subunit is identical in character to Zone b, but the gravity-flow deposits are thinner and thus the resolution of index property measurement with depth does not define variations within these thinner deposits. In this zone, bulk density varies from 1.7 to 2.1 Mg/m^3, porosity from 43% to 64%, and water content, as a proportion of dry mass, from 29% to 62%. Sampling within the limited recovery of the transition zone from 175.1 to 193.0 mbsf was too sparse to define physical property trends.

Unit II (193.0–457.0 mbsf) is dominated by thick turbidite sands (see "Lithostratigraphy" section, this chapter). Only a limited amount of core was measured for physical properties in this unit because of the low recovery and highly disturbed state of the coarse-grained sediment. The general trend in this sparse data suggests a small, broad peak in porosity and water content (with an associated reduction in bulk density) centered near 310 mbsf (Fig. 42). The average porosity of Unit II sediment is 49%.

Thin interbedded fine-grained turbidites become increasingly dominant toward the bottom of Unit III (457.0–566.9 mbsf). Similar to Zone a in Unit I, the index properties follow a pattern normally associated with gravitational compaction; i.e., decreasing porosity and water content and increasing bulk density with depth (Figs. 42–43 and Table 10). The mean porosity through Unit III is 43%.

The MST-measured GRAPE data were collected routinely in the top 200-m section of Site 888 (Fig. 44). Measurements in the deeper cores were poor because the samples are badly disturbed. Selected cores from deeper intervals (those that appeared to fill the liner) were run through the MST, resulting in GRAPE bulk-density values that varied from 1.8 to 2.2 Mg/m^3. Because only selected cores were run through the MST, downhole trends could not be interpreted for

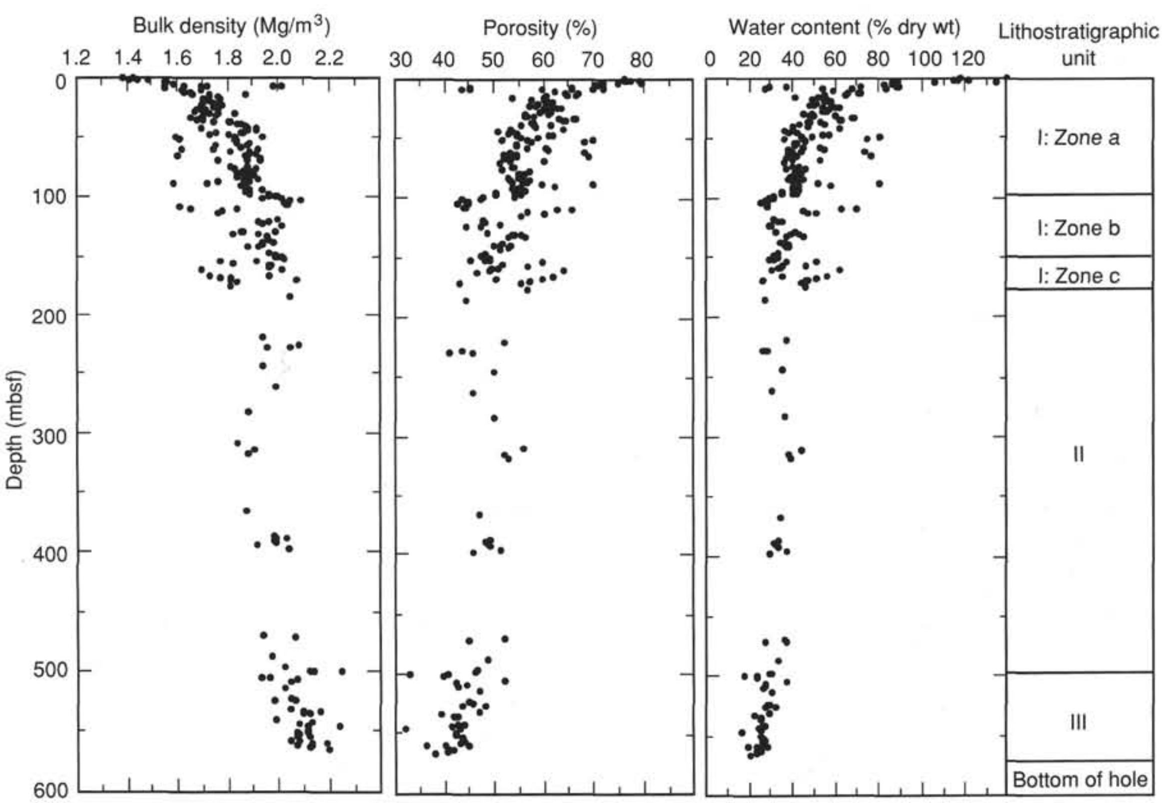

Figure 42. Bulk density, porosity, and water content plotted vs. depth for lithostratigraphic Units I, II, and III. Unit I is broken into three zones based on physical property variations.

Table 10. Summary of index property data, Hole 888A and 888B.

Core, section, interval (cm)	Depth (mbsf)	Bulk density (Mg/m^3)	Porosity (%)	Water content (%)		Grain density (Mg/m^3)	Dry-bulk density (Mg/m3)
				Dry mass	Total mass		
146-888A-							
1H-1, 49	0.49	1.42	76.3	118.6	53.70	2.66	0.65
1H-1, 98	0.98	1.38	79.3	139.7	61.74	2.68	0.58
1H-2, 15	1.65	1.44	79.3	115.4	56.81	2.71	0.67
1H-2, 47	1.97	1.44	77.8	121.9	58.22	2.81	0.65
1H-2, 118	2.68	1.44	76.7	116.9	57.11	2.76	0.66
1H-3, 39	3.39	1.48	76.7	106.3	54.62	2.78	0.72
1H-3, 89[a]	3.89	1.55	72.0	88.7	47.61	2.72	0.82
1H-4, 43	4.93	1.55	71.0	86.6	49.19	2.77	0.83
1H-4, 111[a]	5.61	1.58	70.5	82.5	45.79	2.72	0.86
1H-5, 134	7.34	1.98	45.2	29.8	24.31	2.74	1.52
1H-6, 53	8.03	1.69	45.3	36.9	26.92	2.23	1.24
1H-6, 84	8.34	2.01	43.7	27.9	23.14	2.76	1.57
1H-6, 114	8.64	1.72	65.6	53.6	36.97	2.72	1.12
2H-2, 124[a]	8.24	1.55	45.3	88.2	47.45	2.72	0.82
2H-2, 23[a]	7.23	1.55	70.5	89.1	47.71	2.72	0.82
2H-3, 8	8.58	1.63	43.7	68.2	43.00	2.75	0.97
2H-3, 104	9.54	1.55	69.9	84.1	48.39	2.71	0.84
2H-4, 50	10.50	1.69	62.1	59.2	39.42	2.73	1.06
2H-5, 124	12.74	1.65	66.8	65.5	41.92	2.74	0.99
2H-5, 40	11.90	1.62	62.1	71.4	44.14	2.77	0.94
2H-6, 50	13.50	1.63	66.7	70.4	43.80	2.79	0.96
2H-6, 125	14.25	1.66	64.8	65.1	41.82	2.79	1.01
2H-7, 22	14.72	1.73	71.5	55.1	37.66	2.78	1.11
146-888B-							
1H-3, 40[a]	3.40	1.41	76.7	135.2	58.07	2.72	0.60
1H-3, 40[a]	4.40	1.56	72.0	86.7	47.03	2.72	0.83
2H-1, 130	6.80	1.58	70.5	72.1	41.86	2.62	0.92
3H-1, 40[a]	15.40	1.87	65.8	40.9	29.50	2.72	1.33
3H-1, 106	16.06	1.73	60.0	53.6	36.97	2.76	1.13
3H-2, 28[a]	16.78	1.76	60.0	52.2	34.85	2.72	1.16
3H-2, 120	17.70	1.72	60.8	55.6	37.87	2.75	1.10
3H-3, 8	18.08	1.77	57.8	49.0	34.83	2.76	1.19
3H-3, 98	18.98	1.70	62.0	58.1	38.96	2.77	1.08
3H-4, 41	19.91	1.70	61.8	58.2	38.96	2.74	1.07
3H-4, 98	20.48	1.73	60.6	54.9	37.57	2.76	1.11
3H-5, 20	21.20	1.74	58.7	51.4	35.97	2.73	1.15
3H-5, 115	22.15	1.70	61.7	57.9	38.86	2.74	1.07
3H-6, 35	22.85	1.78	57.3	48.0	34.40	2.76	1.20
3H-6, 111	23.61	1.76	58.3	50.0	35.32	2.76	1.18
3H-7, 45	24.45	1.69	62.9	60.1	39.76	2.77	1.06
4H-1, 70	25.20	1.74	60.3	53.6	37.01	2.80	1.13
4H-1, 101	25.51	1.69	63.6	61.5	40.38	2.80	1.04
4H-2, 55	26.55	1.71	61.6	57.1	38.54	2.76	1.09
4H-2, 119	27.19	1.68	60.2	56.6	36.12	2.63	1.07
4H-3, 40	27.90	1.76	61.3	53.9	34.97	2.89	1.15
4H-3, 100	28.50	1.67	59.2	55.4	35.61	2.58	1.08
4H-4, 36	29.36	1.70	61.0	56.5	36.06	2.73	1.09
4H-4, 108	30.08	1.73	56.3	48.7	32.71	2.61	1.16
4H-5, 40	30.90	1.83	56.3	44.8	30.88	2.84	1.27
4H-5, 80	31.30	1.76	56.9	48.3	32.52	2.70	1.19
4H-6, 20	32.20	1.75	58.0	50.1	33.35	2.72	1.17
4H-6, 85[a]	32.85	1.70	63.3	60.0	38.07	2.72	1.06
4H-7, 38[a]	33.88	1.65	66.0	67.5	40.88	2.72	0.99
5H-1, 30[a]	34.30	1.65	66.4	68.6	41.25	2.72	0.98
5H-1, 110[a]	35.10	1.69	64.2	62.4	38.99	2.72	1.04
5H-2, 45[a]	35.95	1.68	64.4	62.8	39.13	2.72	1.03
5H-2, 110	36.60	1.70	58.2	52.9	34.56	2.60	1.11
5H-3, 25	37.25	1.81	57.8	47.6	32.20	2.83	1.22
5H-3, 100[a]	38.00	1.80	58.0	48.3	33.09	2.72	1.21
5H-4, 20[a]	38.70	1.74	61.3	55.3	36.14	2.72	1.12
5H-4, 110[a]	39.60	1.84	55.5	43.6	30.86	2.72	1.28
5H-5, 20	40.20	1.85	58.6	46.7	31.81	2.98	1.26
5H-6, 20	41.70	1.87	53.5	40.5	28.80	2.81	1.33
5H-6, 105[a]	42.55	1.69	63.9	61.7	38.71	2.72	1.05
5H-7, 35	43.35	1.88	53.7	40.3	28.67	2.84	1.34
6H-1, 30	43.80	1.91	50.7	36.6	26.75	2.79	1.40
6H-1, 100	44.50	1.88	53.2	39.9	28.47	2.82	1.34
6H-2, 40	45.40	1.91	52.9	38.7	27.86	2.87	1.38
6H-2, 100	46.00	1.85	54.7	42.5	29.80	2.80	1.30
6H-3, 54	47.04	1.86	54.6	41.9	29.47	2.84	1.31
6H-3, 100	47.50	1.75	60.9	54.0	35.02	2.84	1.14
6H-4, 20[a]	48.20	1.73	61.9	56.6	36.69	2.72	1.10
6H-4, 120	49.20	1.80	58.8	49.1	32.90	2.86	1.21
6H-5, 60	50.10	1.83	55.7	44.4	30.71	2.80	1.26
6H-5, 100[a]	50.50	1.59	69.9	80.4	45.17	2.72	0.88
6H-6, 30	51.30	1.83	56.8	45.7	31.31	2.84	1.25
6H-6, 100[a]	52.00	1.61	51.8	75.1	43.48	2.72	0.92
6H-6, 7	51.07	1.94	69.9	36.8	26.86	2.89	1.42
7H-1, 60	53.60	1.84	57.7	46.4	31.65	2.90	1.25
7H-2, 80	55.30	1.84	54.8	42.7	29.89	2.80	1.29
7H-2, 110	55.60	1.89	54.6	41.1	29.11	2.89	1.34
7H-3, 77	56.77	1.88	54.8	41.7	29.40	2.87	1.32
7H-4, 130	58.80	1.85	60.4	44.8	30.91	2.88	1.27
7H-4, 50[a]	58.00	1.75	54.8	53.2	35.26	2.72	1.15
7H-5, 130[a]	60.30	1.74	61.1	54.7	35.91	2.72	1.13
7H-6, 100[a]	61.50	1.62	53.3	74.0	43.10	2.72	0.93
7H-6, 31	60.81	1.92	61.1	38.8	27.93	2.91	1.38
7H-7, 64	62.64	1.89	53.9	40.3	28.67	2.87	1.35
8H-1, 30	62.80	1.81	54.7	43.8	30.43	2.72	0.77
8H-1, 88	63.38	1.89	52.3	38.7	27.86	2.80	1.36
8H-2, 30	64.30	1.91	53.0	38.8	27.92	2.87	1.38
8H-2, 124	65.24	1.87	53.7	41.9	29.49	2.86	1.32
8H-2, 50	64.50	1.89	53.0	40.0	28.54	2.87	1.35
8H-3, 20[a]	65.70	1.60	69.0	77.0	44.07	2.72	0.91
8H-4, 16	67.16	1.93	52.3	37.5	27.24	2.89	1.40
8H-5, 47[a]	68.97	1.76	60.3	52.9	35.14	2.72	1.15
8H-5, 104[a]	69.54	1.88	53.2	39.9	29.01	2.72	1.34
8H-6, 45	70.45	1.93	51.3	36.4	26.68	2.86	1.42
9H-2, 130	74.80	1.81	53.7	43.4	30.21	2.71	1.26
9H-2, 73	74.23	1.88	51.3	40.2	28.65	2.84	1.34
9H-3, 80[a]	75.80	1.91	51.5	37.3	27.65	2.72	1.39
9H-4, 28	76.78	1.83	57.1	46.0	31.45	2.86	1.25
9H-5, 38	78.38	1.86	55.2	42.6	29.82	2.86	1.31
9H-5, 95	78.95	1.89	55.3	41.6	29.36	2.93	1.34
9H-6, 25	79.75	1.84	56.2	44.4	30.69	2.86	1.28
9H-6, 110	80.60	1.85	55.9	43.9	30.46	2.85	1.28
10H-1, 40	81.90	1.88	54.9	41.6	29.34	2.89	1.33
10H-1, 113	82.63	1.90	53.1	39.1	28.05	2.87	1.37
10H-2, 30	83.30	1.88	55.7	42.5	29.79	2.92	1.32
10H-2, 145	84.45	1.84	57.1	45.6	31.26	2.88	1.26
10H-3, 40	84.90	1.92	53.3	38.7	27.86	2.92	1.39
10H-3, 100	85.50	1.87	56.9	44.4	30.70	2.94	1.29
10H-4, 35	86.35	1.86	56.1	43.7	30.39	2.88	1.29
10H-4, 100	87.00	1.89	54.0	40.4	28.75	2.87	1.34
10H-5, 50[a]	88.00	1.76	59.9	52.1	34.78	2.72	1.16
10H-5, 100[a]	88.50	1.58	70.1	80.9	45.30	2.72	0.88
10H-6, 50[a]	89.50	1.72	62.5	58.1	37.29	2.72	1.09
10H-6, 110	90.10	1.87	55.7	42.9	29.97	2.89	1.31
10H-7, 30	90.80	1.85	55.6	43.4	30.22	2.85	1.29
11H-1, 20	91.20	1.87	54.5	41.6	29.36	2.85	1.32
11H-1, 110	92.10	1.87	53.7	40.7	28.90	2.82	1.33
11H-2, 50	93.00	1.87	56.4	43.5	30.29	2.93	1.31
11H-3, 40	94.40	1.89	54.4	40.7	28.90	2.89	1.34
11H-3, 100	95.00	1.94	50.6	35.7	26.29	2.84	1.43
11H-4, 40	95.90	1.89	54.8	41.4	29.22	2.89	1.33
11H-4, 100	96.50	1.87	55.3	42.5	29.77	2.87	1.31
11H-5, 50	97.50	1.96	50.4	35.0	25.87	2.87	1.45
11H-5, 100	98.00	1.89	54.1	40.6	28.86	2.87	1.34
11H-6, 30	98.80	1.99	47.7	31.7	24.06	2.84	1.51
11H-6, 100	99.50	2.00	47.3	31.2	23.76	2.84	1.52
11H-7, 40	100.40	1.96	43.8	29.1	22.49	2.66	1.52
12H-5, 40	106.90	2.04	44.6	28.1	21.90	2.84	1.60
12H-5, 80	107.30	2.03	45.0	28.1	21.89	2.80	1.58
12H-1, 40	100.90	2.01	43.8	31.3	23.83	2.87	1.53
12H-1, 100	101.50	1.94	43.8	30.2	23.18	2.67	1.49
12H-2, 40	102.40	2.05	43.8	27.8	21.74	2.84	1.60
12H-3, 30	103.80	2.09	43.8	25.8	20.46	2.86	1.66
12H-3, 90	104.40	2.02	43.8	28.9	22.42	2.80	1.56
13H-1, 40	109.00	1.61	65.7	70.3	41.22	2.68	0.94
13H-1, 130	109.90	1.65	62.9	62.5	38.42	2.67	1.02
13H-2, 60	110.70	1.84	56.9	45.1	31.05	2.89	1.27
13H-3, 120	112.80	1.78	60.1	51.6	34.00	2.88	1.17
13H-4, 60	113.70	1.76	55.7	47.0	31.91	2.64	1.19
14H-1, 55	118.65	2.00	47.9	31.8	24.09	2.86	1.51
14H-1, 120	119.30	2.00	47.9	31.8	24.07	2.86	1.52
14H-2, 70	120.30	1.92	48.2	33.7	25.15	2.73	1.44
14H-2, 115	120.75	1.96	51.3	35.7	26.29	2.91	1.44
14H-4, 50	123.10	1.94	44.3	29.8	22.91	2.65	1.50
14H-4, 95	123.55	2.01	47.3	30.9	23.58	2.87	1.54
15H-1, 125	128.85	1.99	48.6	32.7	24.60	2.87	1.50
15H-2, 40	129.50	1.86	54.4	41.6	29.36	2.83	1.31
15H-2, 120	130.30	1.85	55.6	43.2	30.15	2.85	1.29
15H-3, 40	131.00	1.92	54.0	39.4	28.22	2.94	1.38
15H-3, 130[a]	131.90	1.82	56.5	45.4	31.75	2.72	1.25
15H-4, 20	132.30	1.95	53.0	37.5	27.25	2.96	1.42
16H-1, 25	137.35	1.96	51.7	36.3	26.60	2.92	1.43
16H-1, 110	138.20	1.98	50.1	34.2	25.46	2.90	1.47
16H-3, 30	140.40	1.94	53.0	38.0	27.49	2.94	1.41
16H-3, 120	141.30	1.92	51.2	38.4	27.71	2.89	1.39
16H-2, 50	139.10	1.94	50.1	38.4	27.70	2.95	1.40
16H-2, 100	139.60	1.94	50.1	36.1	26.51	2.88	1.43
16H-4, 50	142.10	1.88	51.2	37.8	27.39	2.75	1.36
17H-1, 30	146.90	1.96	48.3	32.9	24.75	2.80	1.47
17H-2, 42	148.52	1.99	47.4	31.4	23.89	2.84	1.52
17H-3, 42	150.02	1.99	49.0	33.0	24.81	2.88	1.49
17H-3, 100	150.60	2.00	49.0	32.8	24.67	2.90	1.50
17H-4, 15	151.25	2.01	48.1	31.8	24.07	2.89	1.53
17H-4, 101	152.11	2.02	45.2	29.0	22.43	2.82	1.57
17H-5, 116[a]	153.76	1.77	59.7	51.6	34.58	2.72	1.17
17H-6, 31[a]	154.41	1.91	51.6	37.4	27.69	2.72	1.39
18X-1, 75[a]	156.85	1.82	56.8	46.0	32.03	2.72	1.24
18X-2, 31	157.91	1.96	50.8	35.3	26.03	2.89	1.45
18X-2, 75	158.35	1.97	49.7	34.0	25.32	2.88	1.47
18X-3, 70	159.80	1.96	49.0	33.6	25.10	2.84	1.47
18X-4, 24[a]	160.84	1.69	64.0	61.9	38.80	2.72	1.04
18X-4, 97	161.57	2.01	46.7	30.5	23.34	2.85	1.54
19X-1, 56[a]	166.16	1.73	61.7	56.2	36.53	2.72	1.11
19X-1, 140	167.00	1.96	50.6	35.1	25.97	2.88	1.45
19X-2, 67[a]	167.77	1.77	59.6	51.5	34.54	2.72	1.17
19X-3, 35[a]	168.95	1.81	57.1	46.5	32.26	2.72	1.24
19X-3, 104[a]	169.64	1.81	57.4	47.1	32.52	2.72	1.23
19X-4, 30	170.40	2.07	43.2	26.5	20.94	2.85	1.64
19X-4, 120[a]	171.30	1.84	55.7	44.1	31.10	2.72	1.27
20X-1, 35[a]	175.45	1.81	56.9	46.2	32.12	2.72	1.24
21X-1, 25	184.85	2.05	44.4	27.8	21.73	2.85	1.61
25H-2, 36	219.26	1.94	52.3	37.4	27.17	2.90	1.41
26H-1, 10	227.00	2.08	43.7	26.8	21.10	2.87	1.64
26H-1, 120	228.10	2.05	45.6	28.9	22.38	2.87	1.59
26H-2, 20	228.60	1.95	41.1	27.0	21.21	2.57	1.53
28H-1, 62	243.92	1.94	49.9	34.9	25.83	2.83	1.44
30H-1, 130	262.10	1.99	45.9	30.2	23.16	2.78	1.53
33H-1, 25	283.05	1.88	50.0	36.5	26.72	2.71	1.38
36H-1, 25	310.25	1.84	55.9	44.3	30.66	2.83	1.27
36H-6, 55	318.05	1.88	51.9	39.4	28.23	2.80	1.35
36X-4, 60	315.10	1.90	55.9	37.9	27.43	2.82	1.38
42X-1, 30	366.30	1.87	47.2	34.0	25.33	2.60	1.40
44X-1, 120	386.70	1.98	49.1	33.3	24.96	2.87	1.48
44X-2, 130	388.30	1.99	48.8	32.6	24.57	2.89	1.50

Table 10 (continued).

Core, section, interval (cm)	Depth (mbsf)	Bulk density (Mg/m^3)	Porosity (%)	Water content (%)		Grain density (Mg/m^3)	Dry-bulk density (Mg/m3)
				Dry mass	Total mass		
44X-3, 30	388.80	2.03	48.1	31.3	23.83	2.93	1.54
44X-4, 68	390.68	1.98	48.5	32.8	24.64	2.85	1.49
44X-5, 41	391.91	1.99	49.0	32.9	24.74	2.89	1.50
45X-1, 30	395.30	1.91	51.3	37.0	26.96	2.82	1.40
45X-2, 85	397.35	2.04	45.7	29.1	22.49	2.86	1.58
53X-8, 30	471.30	2.06	51.9	27.9	21.77	2.88	1.61
54X-1, 85	470.25	1.94	45.7	36.8	26.88	2.90	1.42
54X-1, 110	470.50	1.94	45.7	36.9	26.94	2.89	1.42
56X-1, 10	487.40	1.97	48.7	33.1	24.85	2.83	1.48
57X-1, 65	496.85	2.02	46.5	30.1	23.09	2.86	1.56
57X-1, 90	497.10	2.02	46.2	29.8	22.92	2.85	1.56
57X-3, 55	499.75	2.12	40.6	23.8	19.21	2.84	1.71
57X-3, 102	500.22	2.25	32.9	17.2	14.69	2.83	1.92
57X-3, 144	500.64	2.14	39.9	23.1	18.74	2.85	1.74
58X-1, 40	505.50	1.93	52.3	37.5	27.24	2.89	1.40
58X-1, 80	505.90	1.96	42.5	27.9	21.81	2.62	1.53
58X-2, 120	507.80	2.07	44.3	27.4	21.51	2.87	1.62
58X-3, 135	509.45	2.05	42.7	26.4	20.89	2.80	1.62
59P-1, 15	514.15	2.02	46.9	30.4	23.27	2.88	1.55
60X-8, 5	525.55	2.06	48.3	27.0	21.21	2.83	1.62
61X-1, 140	523.40	2.05	46.9	28.2	21.96	2.87	1.60
61X-2, 30	523.80	2.05	46.9	29.0	22.44	2.88	1.59
61X-3, 50	525.50	1.98	46.9	32.5	24.50	2.85	1.50
62X-1, 25	531.95	2.05	46.8	29.8	22.93	2.93	1.58
62X-2, 20	533.40	2.16	39.3	22.3	18.23	2.87	1.77
62X-2, 95	534.15	2.10	42.1	25.1	20.07	2.86	1.68
62X-3, 20	534.90	2.10	42.9	25.9	20.54	2.87	1.66
62X-3, 100	535.70	2.12	42.4	25.2	20.09	2.90	1.69
63X-1, 75	541.15	1.99	42.9	27.8	21.70	2.68	1.55
63X-2, 20	542.10	2.13	44.2	26.4	20.85	2.97	1.68
63X-3, 40[a]	543.80	2.08	41.4	24.9	20.32	2.72	1.67
63X-4, 50	545.40	2.11	43.0	25.8	20.50	2.90	1.67
63X-4, 120[a]	546.10	2.24	32.1	16.8	14.65	2.72	1.92
64X-1, 55	549.75	2.11	42.4	25.4	20.20	2.88	1.68
64X-2, 50	551.20	2.11	42.5	25.4	20.22	2.88	1.68
64X-2, 130	552.00	2.07	43.4	26.6	20.99	2.85	1.64
64X-3, 105	553.25	2.08	43.6	26.6	21.00	2.88	1.65
64X-4, 75	554.45	2.07	43.7	27.0	21.22	2.85	1.63
64X-5, 45	555.65	2.12	44.1	26.5	20.93	2.95	1.67
65X-1, 30	558.40	2.08	43.3	26.4	20.88	2.86	1.65
65X-1, 110	559.20	2.05	44.8	28.2	21.96	2.86	1.60
65X-2, 20	559.80	2.13	40.4	23.5	18.98	2.86	1.73
65X-2, 25	559.85	2.19	36.4	20.0	16.67	2.84	1.82
65X-3, 105	562.15	2.07	42.0	25.6	20.38	2.80	1.64
65X-4, 10	562.70	2.13	41.2	24.0	19.35	2.89	1.72
65X-5, 36	564.46	2.12	40.6	23.8	19.21	2.85	1.71
65X-6, 30	565.90	2.20	38.0	21.0	17.34	2.90	1.82

[a]Water content, bulk density, and porosity were back-calculated assuming an average grain density of 2.72 Mg/m^3. This back-calculation was necessary because one batch of samples was oven-dried improperly.

Units II or III from the GRAPE data. However, the data are of moderately good quality and can be used if the lower values of density measured with the GRAPE are ignored. The cores in Units II and III suffered primarily from XCB core disturbance and the low density values are most likely associated with drill slurry which infills partially intact "biscuited" sediment. It is recommended that all MST bulk-density values measured within Units II and III that are lower than 1.8 Mg/m^3 be considered suspect and not be used for analysis.

Electrical Resistivity

Resistivity was measured in selected core samples that were relatively undisturbed in Holes 888A and 888B. The measurement interval varied with the amount and quality of recovered sediment in each core. Electrical resistivity is reported here in its nondimensional form as the ratio of saturated sediment resistivity to pore-fluid resistivity, formation factor. Formation factor has been shown to correlate log-linearly to a function of sediment porosity (Archie, 1942; Lovell, 1984). For the Site 888 measurements, formation factor was used to estimate porosity (see "Explanatory Notes" chapter, this volume).

Formation factor and calculated porosity show trends with depth that are similar to the discrete index property measurements. Within Zone a in Unit I, the resistivity-derived porosity decreases log-linearly with depth, and like the index property data, shows a short excursion to lower values between 5 and 8.5 mbsf (Fig. 45). The large peaks and troughs in the index property data for Zone b and the variability within Zone c in Unit I are also clearly seen in the resistivity data. Resistivity in Unit II also mimics the discrete index measurements, although the data are sparse in this interval.

A comparison of the discrete direct measurements of porosity with the resistivity-derived porosity shows good correlation in trends throughout the site (Fig. 45). The coefficients used in the Archie equation were approximated using an exponential fit to the data from

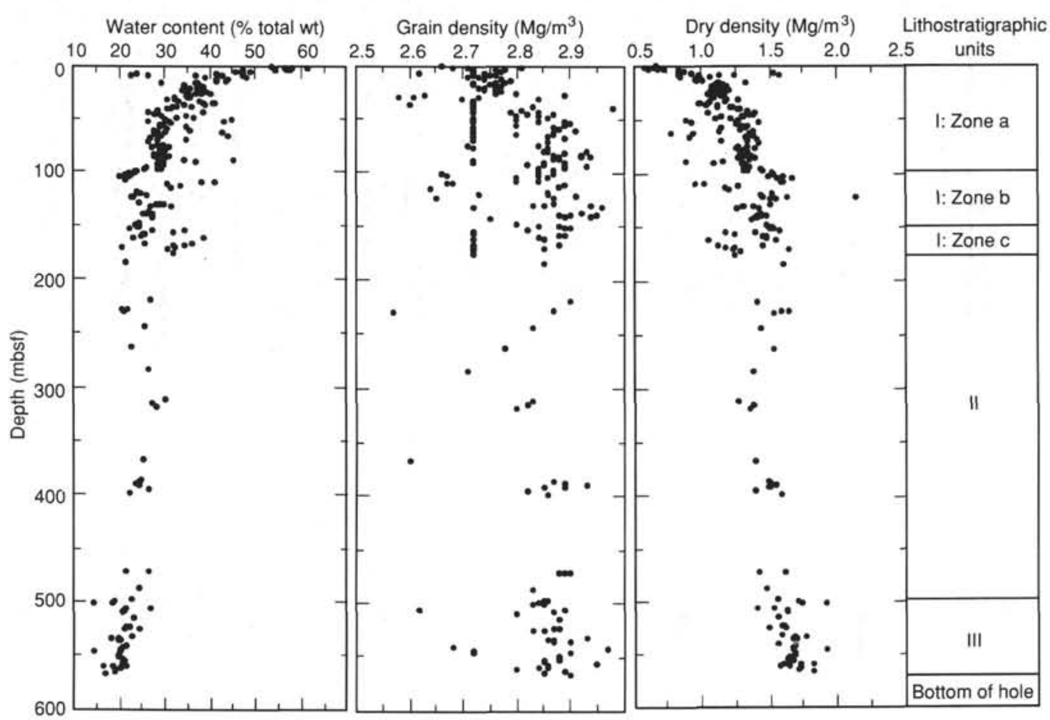

Figure 43. Water content as a percent of total mass, grain density, and dry density vs. depth for lithostratigraphic Units I, II, and III.

Table 11. Thermal conductivity data, Site 888.

Depth (mbsf)	Thermal conductivity (corrected) (W/[m · K])	Depth (mbsf)	Thermal conductivity (corrected) (W/[m · K])
2.60	0.96	140.60	1.24
2.70	1.01	140.60	1.17
3.20	0.90	142.10	1.18
3.90	1.24	142.10	1.21
4.31	0.99	143.60	1.37
5.00	1.04	143.60	1.39
5.80	1.42	148.60	1.49
7.20	1.48	150.10	1.43
7.80	1.48	151.60	1.35
9.30	1.12	153.10	1.49
10.80	1.13	156.60	1.55
12.00	1.12	158.10	1.22
17.30	1.38	159.60	1.31
17.30	1.15	161.05	1.39
18.80	1.12	166.40	1.32
18.80	1.12	167.90	1.46
20.30	1.11	169.40	1.28
20.30	1.10	170.90	1.30
21.80	1.13	175.38	1.46
21.80	1.14	184.88	1.52
26.80	1.30	213.70	1.09
28.30	1.17	216.70	1.46
29.80	1.09	218.10	1.47
31.30	1.19	219.60	1.15
36.30	1.10	220.40	1.18
37.80	1.20	225.60	1.57
39.30	1.36	229.00	1.33
40.80	1.20	230.50	1.20
45.60	1.02	232.00	1.66
47.62	1.17	233.40	1.42
49.30	1.18	236.50	1.39
50.30	1.15	238.00	1.26
55.10	1.12	239.50	1.27
56.50	1.27	241.00	1.48
58.30	1.26	243.92	1.19
60.30	1.22	254.00	1.53
64.71	1.37	258.50	1.47
66.22	1.14	260.00	1.43
69.42	1.26	264.30	1.63
70.42	1.37	265.80	1.58
88.10	1.26	269.80	1.63
89.60	1.25	270.40	1.55
94.42	1.31	272.80	1.60
97.40	1.25	274.30	1.48
98.87	1.31	302.50	1.39
102.78	1.46	303.10	0.97
104.27	1.45	314.93	1.23
107.16	1.40	316.33	1.18
110.85	0.97	387.25	1.36
112.35	1.22	389.15	1.30
113.82	1.20	390.30	1.28
117.10	1.27	392.53	1.52
120.60	1.37	395.70	1.23
123.60	1.25	397.20	1.61
125.10	1.37	470.00	1.37
129.60	1.24	471.02	1.29
131.10	1.21	496.65	1.17
134.10	1.22	498.20	1.54
135.60	1.32	499.70	1.36
139.10	1.27	500.15	1.58
139.10	1.19		

porosity vs. formation factor. The cementation coefficient (m) was set as a constant value of 1.76, representative of deep-sea sediments (Wang et al., 1976). The exponential regression analysis on the data using this value for m results in a tortuosity coefficient (a) of 1.44 (Fig. 46).

Like the index data, the resistivity data are discontinuous at this site because of poor sample quality and low recovery. However, these data can be correlated with the downhole measurements where the shallowest and deepest units have not been logged to provide a complete log of porosity with depth for this site (see "Downhole Logging" section, this chapter).

Acoustic Velocity

Acoustic velocity was measured over discrete intervals in the upper 220-m section of Site 888. Below this depth, low core recovery and highly disturbed XCB cores prohibited measurement. In fine-grained sediment samples from XCB cores, drilling-induced shearing of the sediment caused attenuation of the acoustic signal so that energy was not transmitted across the sample during measurement. The MST P-wave data in the upper 220 m of the site suffered from poor signal quality. Consequently, no MST-measured P-wave data are reported here. The use of these MST-measured velocity data stored in the data base for this site is not recommended.

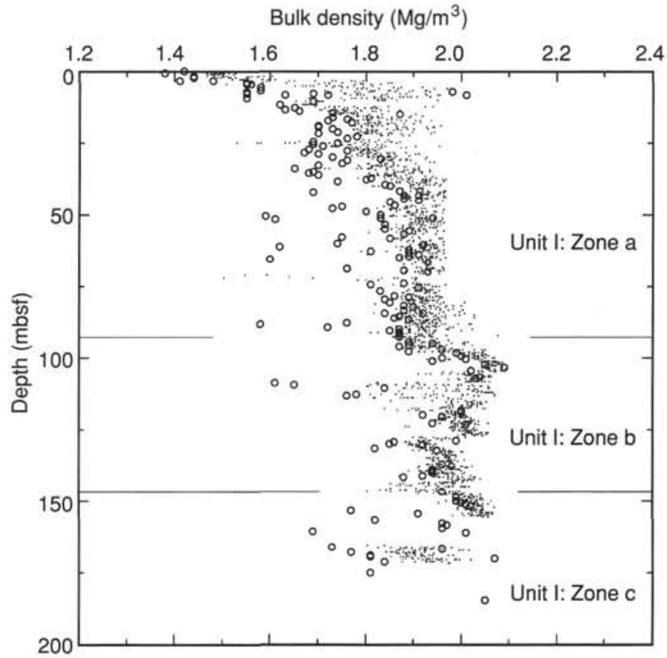

Figure 44. Discrete measurements (open circles) of bulk density compared with those determined with the GRAPE (dots) in lithostratigraphic Unit I of Site 888. The two measurements correlate well, although the discrete measurements are biased toward the lower density, finer materials.

Within Zone a in Unit I, the compressional-wave velocity shows two trends (Fig. 47). Between the mud line and 40 mbsf, the velocity increases nearly linearly from 1450 to 1570 m/s. Below 40 mbsf in Zone a, the velocity first decreases slightly and then varies cyclically from 1520 to 1580 m/s over intervals of 4–6 m, suggesting cyclic depositional sequences. In Zones b and c in Unit I, acoustic velocity shows large excursions from 1500 to 1690 m/s.

A large linear increase in velocity with depth begins at the interface between Zones a and b. This increase is sharply truncated at 105 mbsf, where the acoustic velocity drops to 1505 m/s and then increases again at the Unit I/II boundary. Below this boundary, the data are sparse, but velocity overall increases with depth in Unit II.

Acoustic impedance, the product of bulk density and velocity, can, in principle, be used to identify boundaries that would produce reflections of seismic energy. At Site 888, the impedance profile shows several intervals of high impedance contrast (Fig. 47). Large impedance contrasts must extend over a depth interval of approximately 8 m to produce a reflection event using a seismic frequency of approximately 50 Hz. The largest contrasts that occur over at least an 8-m depth interval are from 30 to 45, 89, 105 to 110, 154, 160 to 167, and 170 mbsf. Correlation of the core-measured impedance with the downhole-measured impedance is presented in the "Downhole Logging" section (this chapter).

Undrained Shear Strength

The undrained shear-strength measurements were made using a motorized miniature vane-shear device in Holes 888A and 888B (see "Explanatory Notes" chapter, this volume). Most data were collected from lithostratigraphic Unit I (0–175.1 mbsf), which is composed

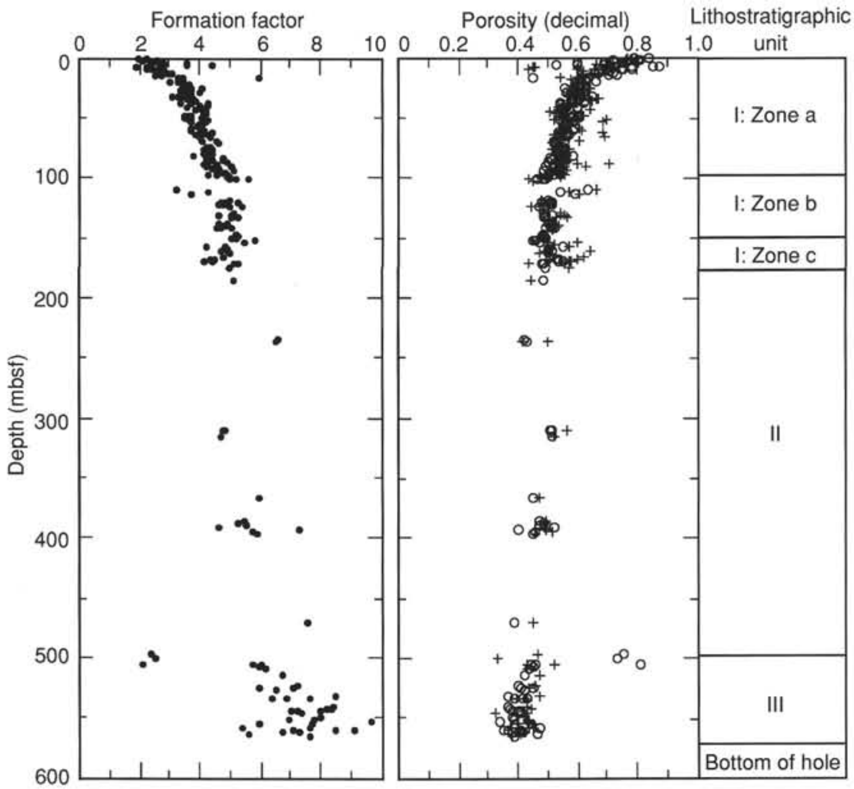

Figure 45. Formation factor (the ratio of sediment resistivity to pore-fluid resistivity) and porosity plotted with depth for Site 888. On the porosity plot, the open symbols were measured directly and the crosses are values derived from the formation factor.

mainly of thin interbedded silts, clays, and fine sand. Measurement was not done in the coarse-grained materials. Sediment strength varies among the zones defined within Unit I by the index properties (Fig. 48). In zone a (0–93 mbsf), strength generally increases downhole from 7 to 70 kPa, but shows increasing scatter with depth. Sediment strength in Zone b (93–147 mbsf) roughly increases downhole. The low strength values at about 105 mbsf can be attributed to the underconsolidation of silty clay layers that were rapidly loaded as a result of high sedimentation rates in the overlying interval. In the lower part of Unit I (135–175.1 mbsf), the values of strength are widely scattered between 30 and 100 kPa. The measurement of low strengths at about 390 mbsf suggests coring disturbance, although the small number of data below Unit II prevents interpretation of strength trends.

The state of sediment consolidation can be estimated by a comparison of the range of strengths measured relative to the range for normally consolidated sediments, expressed as the ratio of undrained strength (S_u) to effective overburden stress (P_o'). Effective overburden stress is calculated from bulk density, pore-fluid density, and overlying sediment thickness, assuming hydrostatic pore-fluid pressure (Fig. 48). The S_u/P_o' ratios decrease downhole in Unit I and have low values (less than 0.07) in Unit II. These ratios, low by comparison with the estimated ratio ($S_u/P_o' = 0.25$) for normal consolidation, indicate significant underconsolidation, which can be attributed to high sedimentation rates at this site.

Thermal Conductivity

Thermal conductivity was measured on soft sediment samples using the needle probe in the full-space mode (see "Explanatory Notes" chapter, this volume). Measurements were usually taken at four points per core in sections with good recovery. All measured values are given in Table 11 and plotted as a function of depth in Figure 49.

Most thermal conductivity measurements at Site 888 were made in lithostratigraphic Unit I, where core recovery was high and sediment samples generally of good quality. Over Unit I, thermal conductivity gradually increases from about 1 W/(m · K) near the seafloor to 1.3–1.5 W/(m · K) near the base of the unit at 175 mbsf. The best-fit line over this depth interval is given by $K(z) = 1.143 + 0.00126z$, where K is the thermal conductivity in W/(m · K) and z is the depth in mbsf.

Few measurements were taken in Units II and III, where core recovery was low and most samples are severely mechanically disturbed. It should be noted, however, that a set of consistently high conductivity values were obtained between 254 and 274 mbsf. These measurements average 1.54 ± 0.07 W/(m · K). They were taken in cores composed mostly of silty sand and sand. The high thermal conductivity over this depth interval probably reflects a grain composition enriched in quartz (see "Lithostratigraphy" section, this chapter).

WSTP AND ADARA TEMPERATURE MEASUREMENTS

Introduction

In-situ bottom-hole sediment temperature measurements at Site 888 were conducted to determine the thermal structure of the abyssal plain basin at the toe of the Cascadia accretionary prism. The thermal structure observed at Site 888 was intended to serve as a reference for thermal studies of the accretionary prism, in particular at the subsequent drilling sites, that aim to assess and quantitatively analyze the thermal effects associated with sediment deformation and fluid flow in the accretionary prism.

To determine the thermal structure at Site 888, a total of 18 bottom-hole sediment temperature measurements were attempted in Hole 888B. The measurements were taken using either the APC coring-shoe temperature tool (ADARA) during regular piston-coring

Table 12. Summary of WSTP and ADARA measurements, Hole 888B.

		Summary of WSTP temperature measurements			
Core	Depth (mbsf)	Temperature above mud line (°C)	Temperature in sediment (°C)	Comments	Status
146-888B-					
6H	43.5	3.00–3.20	6.1–6.7	Flat temperature record in sediment, high noise.	Accepted
9H	72.0	3.03	3.3 ± 0.2	Uncertain fit, high noise. Does not fit the main temperature trend with depth. Suspected invasion of formation by drilling fluid.	Doubtful
12H	100.5	3.04	10.3 ± 0.1	Fairly good-quality record.	Accepted
15H	127.6	2.92–3.23	11.7–12.4	Flat temperature record in sediment, high noise.	Accepted
18X	156.1	3.02	14.1 ± 0.1	Good-quality data.	
22X	194.1	3.04	8.5–9.7	High drift from 8.5° to 9.7°C while in sediment. Probe in fill or insufficient penetration?	Rejected
24H	212.9			Lost data.	
27H	234.2	3.05	4.9–6.7	High drift from 4.9° to 6.7°C while in sediment. Probe in fill or insufficient penetration?	Rejected
31H	267.8	3.04–3.10	4.0 ± 0.1	Good-quality data. Does not fit the main temperature trend with depth. Suspected invasion of formation by drilling fluid.	
46X	404.5	3.04	6.5 ± 0.1	Fairly good-quality data. Does not fit the main temperature trend with depth. Suspected invasion of formation by drilling fluid.	Doubtful

			Summary of APC tool temperature measurements (ADARA measurements)			
Core	Depth (mbsf)	Probe no.	Temperature above mud line (°C)	Temperature in sediment (°C)	Comments	Status
146-888B-						
3H	24.5	15	0.95	3.0 ± 0.1	Good-quality data.	Accepted
4H	34.0	12			Electronics failure, no data.	
5H	43.5	15	0.97	3.9 ± 0.05	Good-quality data.	Accepted
7H	62.5	15	0.94	5.14 ± 0.05	Good-quality data.	Accepted
8H	72.0	12	1.29	6.5 ± 0.4	Good-quality data.	Accepted
10H	91.0	15	0.98	7.4 ± 0.2	Good-quality data.	Accepted
11H	100.5	12	1.27	8.6 ± 0.1	Good-quality data.	Accepted
34H	300.5	12	1.32	21.5 ± 0.1	Good-quality data.	Accepted
37H	329.0	12	1.28	24.0 ± 2	Poor equilibrium determination.	Accepted

Note: All WSTP measurements were taken with Probe 105. Temperature data are raw data before correction for bottom seawater intercalibration.

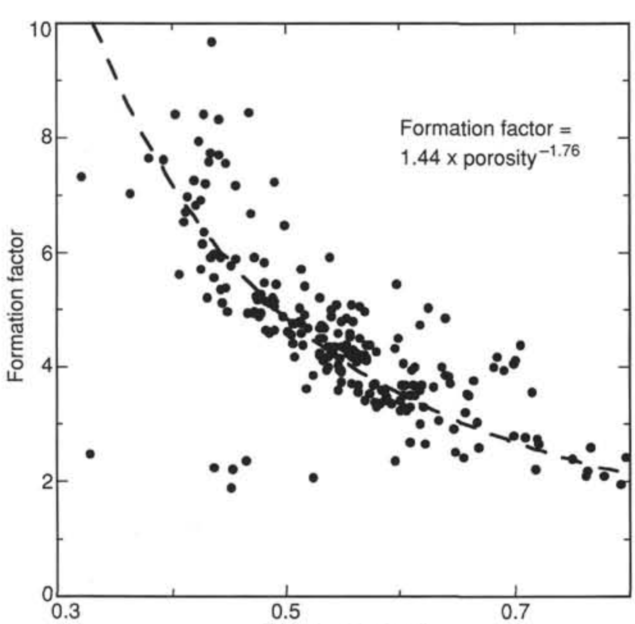

Figure 46. Correlation between formation factor and measured porosity. The fitted curve is of similar form to Archie's equation (Archie, 1942).

operations (see "Explanatory Notes" chapter, this volume) or the water-sampling temperature probe (WSTP), a wireline tool that takes a pore-water sample in addition to the temperature measurement (see "Explanatory Notes" chapter, this volume). The ADARA measurements were not made on the first two APC cores because the bottom-hole assembly (BHA) was not fully spudded into the sediment at that stage. The ADARA measurements were also not conducted when high overpulls indicated a risk of losing the tool if the shoe remained in the sediment for a prolonged time. The ADARA measurements on the APC cores were complemented by WSTP measurements at intervals along the XCB-cored sections of the hole. In addition, ADARA and WSTP measurements were taken at depths of 43.5, 72.0, and 100.5 mbsf for the purpose of cross-calibration. All measurements attempted in Hole 888B are summarized in Table 12.

WSTP Measurements

The version of the WSTP including the pore-water sampler (see "Explanatory Notes" chapter, this volume) was deployed at 10 depths between 43.5 and 403.5 mbsf. The WSTP measurements (Figs. 50 through 58) are of variable quality. Unfortunately, the data collected at 212.9 mbsf were lost during the initial data handling. Out of the nine temperature records collected, those at 194.1 and 234.2 mbsf (Figs. 55–56) showed a high drift, in excess of 1°C over the approximately half-hour duration of measurement. The high drift suggests that the measurements were taken in sediment subject to a considerably disturbed thermal regime. These two measurements were rejected. One

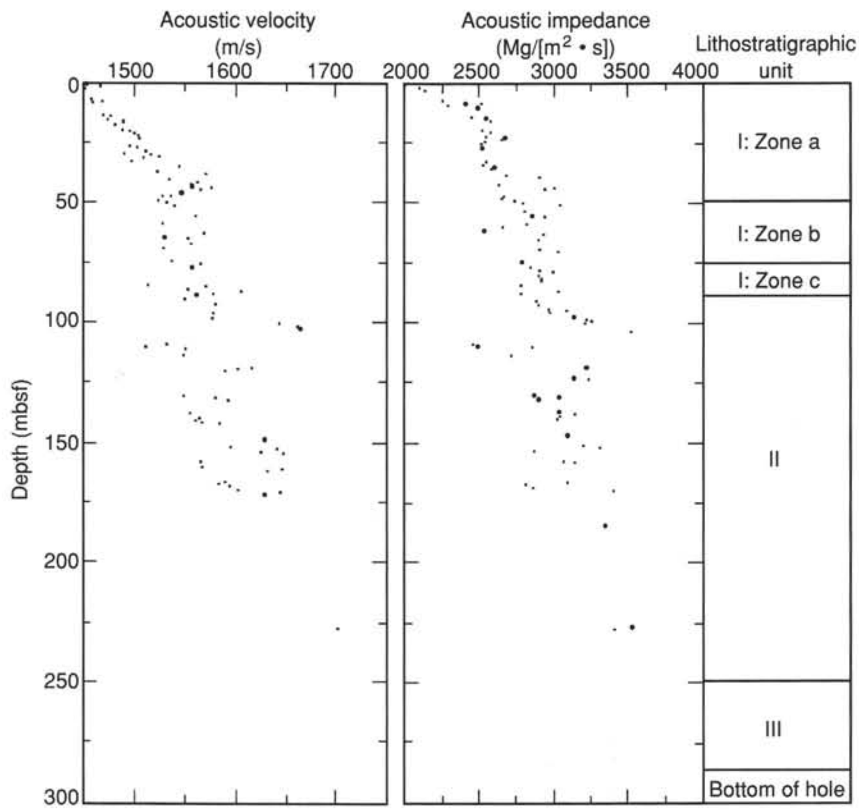

Figure 47. Acoustic compressional-wave velocity, measured discretely on split-core samples, and calculated impedance with depth at Site 888. Velocity measurements were limited to the upper 250 mbsf because of low recovery and disturbed samples below this depth.

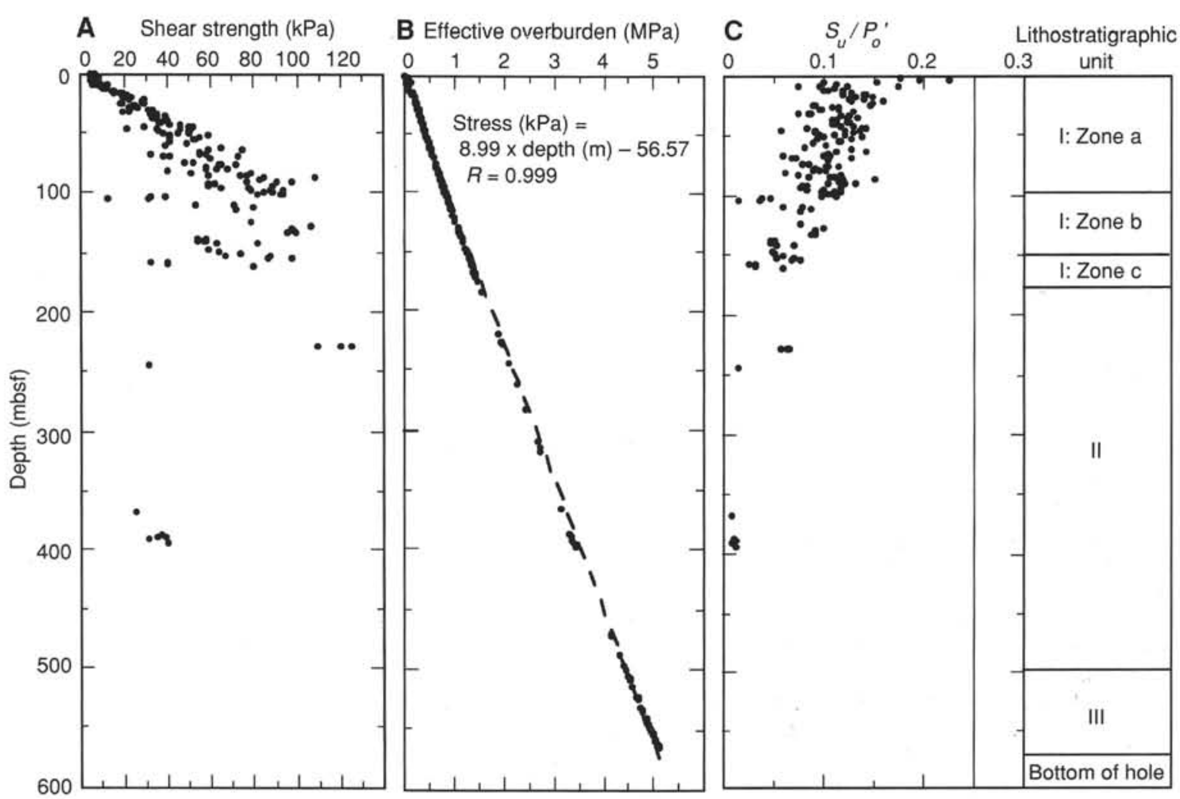

Figure 48. **A.** Undrained shear strength measured with a miniature vane-shear device vs. depth at Site 888. **B.** The effective overburden stress, calculated from discrete bulk-density measurements vs. depth. **C.** Effective overburden stress plotted as a ratio with shear strength vs. depth. A typical normally consolidated clay has a ratio of about 0.25, which suggests that the sediment at Site 888 is undercoı.solidated.

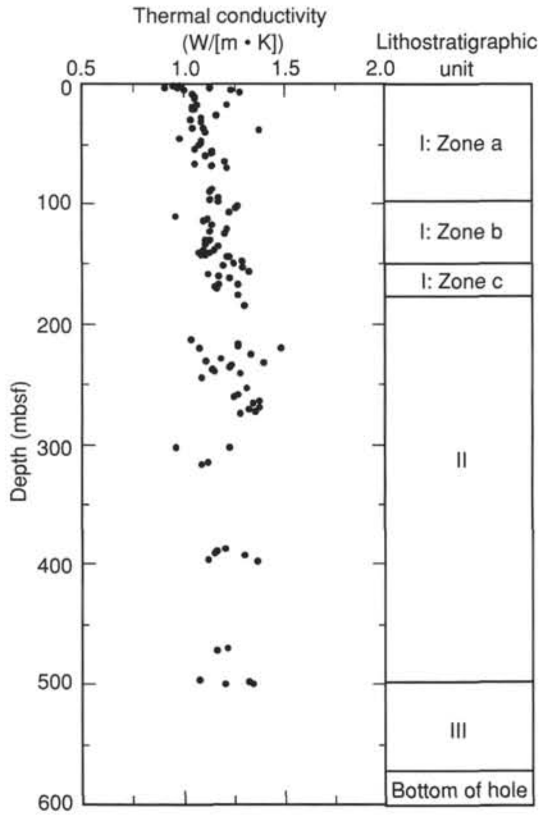

Figure 49. Thermal conductivity vs. depth for Site 888 for lithostratigraphic Units I, II, and III.

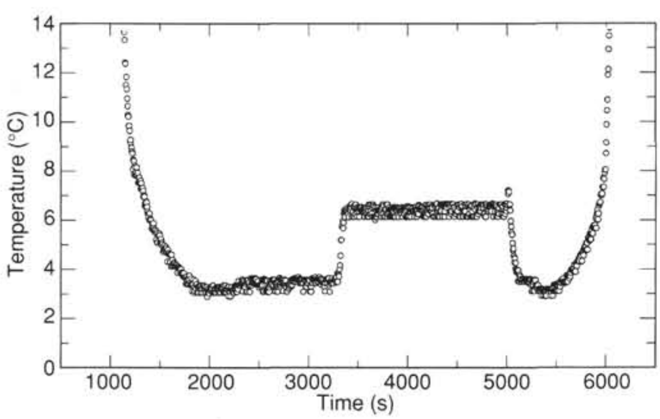

Figure 50. Temperature record from WSTP deployment in Hole 888B at 43.5 mbsf (Core 146-888B-6H).

possible reason why the measurements were unsteady is poor probe penetration, with the result that the probe remained in the field of the thermal disturbance caused by drilling. Except for the two rejected measurements, equilibrium temperatures could be calculated with reasonably high accuracy for all the other WSTP deployments (Table 12). Fairly flat temperature records with no frictional heating peaks at penetration are characteristic of the measurements in clayey silts at 43.5 and 127.6 mbsf (Figs. 50 and 53). In contrast, the measurement at 72 mbsf (Fig. 51) in a sand-rich (80% sand) sediment exhibits a strong heat pulse at penetration. An odd record was obtained at 100.5 mbsf. The temperature record at this depth (Fig. 52) appears to indicate that after a first failed penetration (the probe may have been pulled out immediately after penetration), the probe was slowly forced into the sediment 15 min later with a subsequent normal temperature record. This later record does not show, however, frictional heat pulses at penetration and withdrawal.

All the WSTP deployments were made with the same probe (probe 105). The bottom-water temperature readings range from 2.92° to 3.23°C.

ADARA Measurements

The ADARA measurements are all high-quality data (Figs. 59–60) except for the measurement at 329 mbsf during which the core barrel became stuck in the hole for a short while (Fig. 60). This measurement excluded, equilibrium temperatures could be computed from the decay curves with a high degree of confidence. Estimated uncertainties in the equilibrium temperatures are all within 0.5°C (Table 12).

The ADARA measurements were taken using two different probes, numbers 12 and 15 (Table 12). Both the sensors and the data-acquisition electronics of the two probes are different. The bottom-water temperature readings taken with probe 12 average 0.96° ± 0.02°C; those taken with probe 15 average 1.29° ± 0.02°C. Both probes were crudely calibrated in a thermostabilized bath on board the ship. Readings with both probes were not found to differ from the thermostabilized bath temperature by more than 0.3°C at about 1°C. The average probe 15 temperature reading of 1.29°C was used as the reference bottom-seawater temperature at Site 888.

Temperature Profile with Depth

All the equilibrium temperatures determined are plotted as a function of sub-bottom depth in Figure 61. These temperatures are raw determinations before any correction for intercalibration of the WSTP and ADARA probes has been applied. Figure 62 shows the same data set after the WSTP and ADARA probe 12 temperatures have been corrected by constant values given by the differences in readings of the bottom seawater temperature. Constant corrections of −1.75°C and 0.33°C, respectively, were applied to all the WSTP and ADARA probe 12 readings (Table 13), assuming that the corrections for bottom-seawater temperature remain valid over the whole range of temperatures measured.

The temperature data in Figure 62 clearly indicate a nearly linear increase in temperature with depth, when one excludes the three WSTP data points that plot far below the main temperature trend. The mean temperature gradient defined by the main temperature trend is 68°C/km.

The three WSTP data points, at 72.0, 267.8, and 404.5 mbsf, that plot far below the main temperature trend, were not suspected to be erroneous measurements at the time they were processed. They have well-developed penetration and decay curves. Equilibrium temperatures were calculated in the normal way for these three measurements (Figs. 51 and 57–58). Note, however, that the WSTP temperature measurement of 1.55°C (value corrected for bottom-seawater temperature calibration; Table 13) at 72.0 mbsf is not confirmed by the ADARA measurement of 6.5°C at the same depth, which plots on the main linear trend (Fig. 62).

In contrast, the WSTP- and ADARA-corrected temperatures of 8.55° and 8.6°C, respectively, measured at 100.5 mbsf are comparable and follow the linear trend. The WSTP and ADARA measurements at 43.5 mbsf of 4.35° to 4.95° and 4.23°C, respectively, also match.

One common factor linking the three WSTP measurements that plot far below the main linear temperature trend with depth is that these determinations were taken in sand-rich sections of the hole. It has been noted that the WSTP measurement at 72 mbsf was taken in a sediment composed of approximately 80% fine sand. Massive silty sand was cored at 267.8 mbsf. No sediment was recovered by coring at 404.5 mbsf, presumably because of the occurrence of massive sand at this depth. Significant invasion of the sand formations by the drilling fluid is suspected. The near bottom-water temperature of the

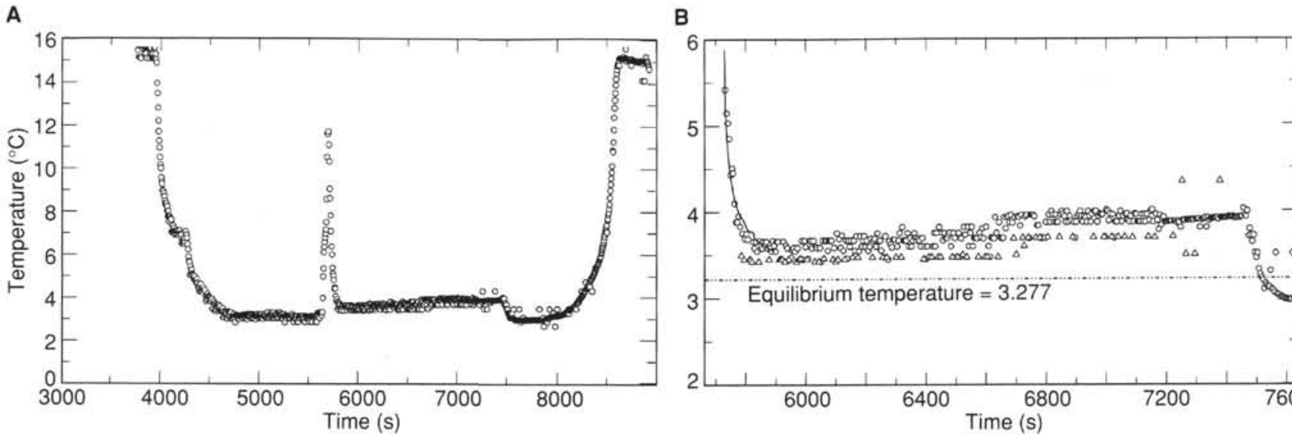

Figure 51. Records from WSTP deployment in Hole 888B at 72 mbsf (Core 146-888B-9H). **A.** Temperature record for entire run. **B.** Close-up of temperature record in sediment. The solid line is the fit curve used to estimate the equilibrium temperature shown by the dashed line. Triangles are points not used for the fit calculation. Note change in both time and temperature scales for each plot.

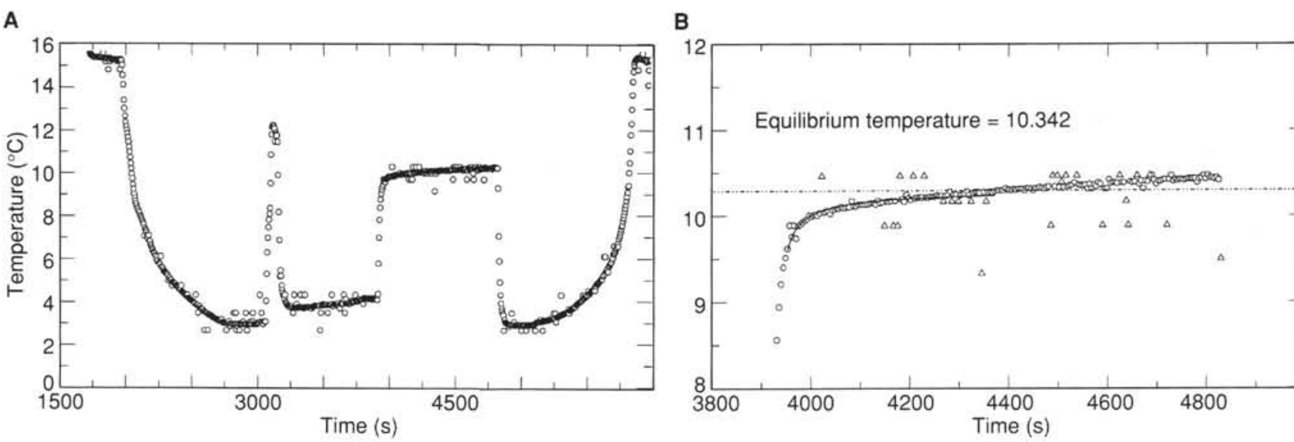

Figure 52. Records from WSTP deployment in Hole 888B at 100.5 mbsf (Core 146-888B-12H). **A.** Temperature record for entire run. **B.** Close-up of temperature record in sediment. Conventions as in Figure 51. Note change in both time and temperature scales for each plot.

drilling fluid would produce cooling of the formations ahead of the bit down to depths exceeding the shallow penetration depth of the WSTP probe. Note that the increase of temperature from the middle to the end of the measurement period at these three depths indicates a disturbed thermal regime.

On the basis that the three WSTP measurements at 72, 267.8, and 404.5 mbsf are doubtful, the overall temperature structure at Site 888, from seafloor to 329 mbsf, can be approximated by a linear increase in temperature with depth at a mean geothermal gradient of 68° ± 2°C/km (Fig. 62).

Heat Flow

Adopting a constant geothermal gradient of 68°C/km and a linear increase in thermal conductivity with depth, as given by $K(z) = 1.143 + 0.00126z$ (see "Physical Properties" section, this chapter), we can infer that heat flow increases from 78 mW/m^2 near the seafloor to 94 mW/m^2 at the base of the transition zone below lithostratigraphic Unit I at 193.0 mbsf. If we adopt a constant thermal conductivity of 1.38 W/(m · K) (measured mean value) below 193.0 mbsf, heat flow remains constant at 94 W/m^2 through lithostratigraphic Units II and III. These preliminary estimates indicate a significant increase in heat flow with depth in the upper part of the hole. They are significantly lower than the surface heat flow of about 120 mW/m^2 measured by Davis et al. (1990).

DOWNHOLE LOGGING

Log Reliability

Hole size was the most important control on the accuracy of logs from Leg 146, and hole size at Hole 888C was quite variable, as shown by the caliper log (Fig. 63). This variability had two effects on Site 888 logging. First, a hole constriction, or "bridge," prevented the tool string from reaching the bottom 91 m of the hole; the deepest point logged was 509.4 mbsf. Second, the enlarged hole degraded the accuracy of some types of measurement.

Measurements made by the lithodensity tool are unreliable in intervals with a hole diameter greater than 43 cm, because this pad-type tool has an eccentralizing arm that is unable to maintain firm contact with such enlarged borehole walls. Loss of pad contact causes anomalously low bulk-density values. We have deleted the obviously erroneous density values (Fig. 63), but many of the lowest density measurements in the interval from 440 to 500 mbsf may also be underestimates of the true bulk density. Enlargement of the hole can cause more subtle systematic errors in the measurements from several other logs: neutron porosities may be too high, natural gamma counts may be too low, and resistivity measurements may be too low. Post-cruise borehole correction is expected to change these values slightly, resulting in minor differences between the borehole-corrected logs (see LDEO logging figures on CD-ROM in back pocket) and the uncorrected logs (Figs. 63–65).

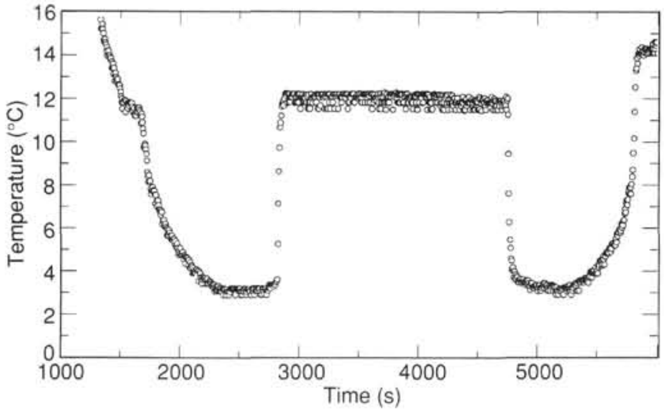

Figure 53. Temperature record from WSTP deployment in Hole 888B at 127.6 mbsf (Core 146-888B-15H).

As is often the case with ODP holes, the initial sonic logs from Hole 888C exhibit a few zones in which cycle skipping occurred, resulting in unreliable swings in apparent velocity. Reprocessing (see "Explanatory Notes" chapter, this volume) appears to have removed all unreliable data, and we consider the reprocessed velocity log (Fig. 64) to be of good quality.

The spectral gamma and neutron tools are the only tools on the geophysical string that can provide useful formation data through pipe. At Hole 888C, through-pipe spectral gamma and neutron logs were obtained for the interval 0–89 mbsf. These logs should be corrected for pipe attenuation, but such corrections have not been undertaken yet.

Correlation of Logs with Lithostratigraphic Units

The three lithostratigraphic units at Site 888 are well delineated by the caliper, gamma-ray, and velocity logs (Figs. 64–65). Lithostratigraphic Unit I, which extends from the seafloor to 175.1 mbsf (see "Lithostratigraphy" section, this chapter), is characterized by a hole that is relatively uniform and close to bit size (26 cm), with minor deviations to 35 cm. Gamma-ray values exceed 50 API units for most of the open-hole-logged section (below 89 mbsf).

Logs indicate that the boundary between Units I and II is transitional. The caliper and gamma-ray log responses for the interval between 175 and 193 mbsf show that deposition of the massive sands of Unit II was followed by a period of dominantly silt deposition, interrupted by four influxes of sand (173.5–176.8, 178.4–179.8, 182.7–184.8, and 186.0–187.3 mbsf). The base of the transition zone (193 mbsf) is marked by a distinct increase in sonic velocity below the transition zone.

Unit II is characterized by sections of enlarged hole tens of meters in length and by velocity values consistently higher than those observed in Unit I. Gamma-ray values in Unit II range from about 30–50 API units, and they vary inversely with hole diameter. The logged portion of Unit III is marked by short-wavelength variations in hole diameter, with an absence of large-diameter sections more than 10 m thick, and with gamma values generally exceeding 40 API units.

The high gamma-ray values and the normal hole diameter indicate that Unit I is more cohesive than Unit II, probably because it is richer in clay or in mud/mudstone. The substantial washouts in Unit II suggest thick sequences of sand beds, as do the low gamma values over the same intervals. A standard gauge hole is about 26 cm in diameter, in contrast to the washed-out sections that reach more than 44 cm. The proportion of hole greater than or less than the midpoint between these two extremes provides a measure of the ratio of noncohesive to cohesive lithologies at 57:42. In Unit II the gamma-ray curve has been divided along its approximate median of 40 API units; the portion of the hole above the median (32%) correlates well with the smaller gauge hole and is interpreted as a mud-rich section, whereas the portion lower than the median value (68%) correlates well with the larger-diameter portion of the hole and is interpreted as a sand-rich section. Thus, analysis of both the caliper and gamma-ray logs suggests that Unit II is richer in sand than in mud/mudstone. Between 268 and 290 mbsf, the caliper tool shows two cycles of a gradual upsection decrease in hole diameter that may represent fining- and thinning-upward turbidite sequences indicative of submarine-fan channel fill.

Table 13. Summary of corrected WSTP and ADARA temperatures, Hole 888B.

Depth (mbsf)	Temperature[a] (°C)	Instrument
0.0	1.29	
24.5	3.33 (0.1)	ADARA15
43.5	4.23 (0.05)	ADARA15
43.5	4.65 (0.3)	WSTP105
62.5	5.47 (0.05)	ADARA15
72.0	6.50 (0.4)	ADARA12
72.0	1.55 (0.2)	WSTP105
91.0	7.70 (0.2)	ADARA15
100.5	8.60 (0.1)	ADARA12
100.5	8.55 (0.3)	WSTP105
127.6	10.30 (0.4)	WSTP105
156.1	12.35 (0.1)	WSTP105
267.8	2.25 (0.1)	WSTP105
300.5	21.50 (0.1)	ADARA12
329.0	24.00 (2.0)	ADARA12
404.5	4.75 (0.1)	WSTP105

[a]Error limits in parentheses.

The gamma-ray log appears to exhibit a bimodal pattern of alternation between sand and clayey silt beds. These lithologic variations can be quantified by estimating sand and silt baselines. Figure 66 shows our estimate of the sand baseline: a linear reduction in gamma-ray counts down to about 230 mbsf, then a constant baseline value of 30 API units below this depth. When this apparent sand baseline is removed, the constant-value silt baseline is evident. Rescaling the gamma-ray log to 0% at the sand baseline and 100% at the silt baseline yields the sand/silt log of Figures 66 and 67. This sand/silt log is generally similar to our interpreted variations in silt and sand based on the caliper log (Fig. 67). These two independent measures of downhole lithologic variations serve as our basis for interpreting the relationship of lithology to velocity, porosity, and density at Site 888.

Porosity and Density

We obtained log-based estimates of porosity at Site 888 from the neutron, density, and resistivity logs. Neutron porosity (ϕ_n) measures the total hydrogen content of the formation, including bound water in clays, free water in pores, and hydrocarbons. Thus, neutron porosities can be too high in formations that are rich in clay minerals. At Site 888, however, clay mineral concentration is so low (see "Lithostratigraphy" section, this chapter) that this source of error is minor. A more substantial source of neutron-log error is the lack of tool eccentralization during logging. Broglia and Ellis (1990) estimate that this error can cause measured porosities in basalts to be too high by as much as 7%, and a similar error of several percent is likely for Site 888 sediments.

The density log (ρ_b) was converted to porosity (ϕ_d) using the relationship $\phi_d = (\rho_b - \rho_m)/(\rho_w - \rho_m)$, where water density ($\rho_w$) and grain density ($\rho_m$) were assumed to be 1.05 and 2.80 Mg/m^3, respectively, based on index measurements of the core (see "Physical Properties" section, this chapter). Sensitivity to variations in ρ_m was evaluated over the range from 2.75 to 2.85 Mg/m^3; calculated porosities varied by less than 2%.

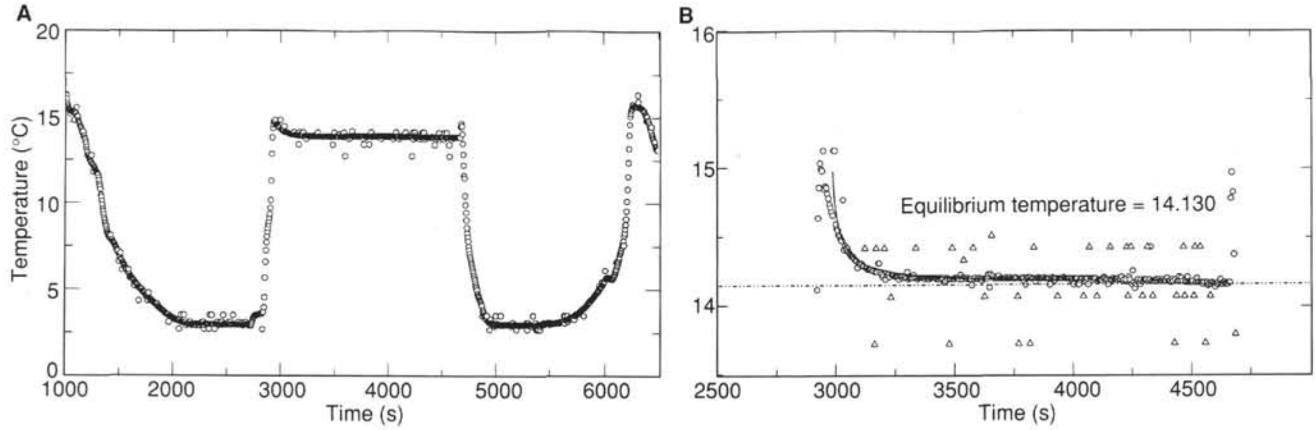

Figure 54. Records from WSTP deployment in Hole 888B at 156.1 mbsf (Core 146-888B-18X). **A.** Temperature record for entire run. **B.** Close-up of temperature record in sediment. Conventions as in Figure 51. Note change in both time and temperature scales for each plot.

Porosity was estimated from the resistivity log (Ω) using the relationship of Archie (1942), as generalized by Winsauer et al. (1952):

$$\phi_r = (a/F)^{-m},$$

where F is the formation factor and a and m are constants. This equation assumes that all electrical conduction in the rocks is attributable to pore fluids; clay conduction is assumed to be negligible. Though clay conduction can dominate the porosity response of compacted shales (Waxman and Smits, 1968), its effect is small in high-porosity terrigenous sediments (Jarrard et al., 1989), and the sediments at Site 888 are lower in clay minerals than most terrigenous sediments.

The formation factor is a function of measured formation resistivity (R_o) and of pore-water resistivity (R_w):

$$F = R_o/R_w.$$

The resistivity of pore water is a function of temperature and salinity. Temperature was assumed to vary linearly from 2°C at the seafloor to 16°C at 500 mbsf. This estimate assumes that pore-water temperatures within the near-borehole zone measured by the resistivity log are intermediate between equilibrium pore-water temperatures and the temperature of seawater used for drilling. Constant salinity of 35‰ was assumed, although observed salinities decrease with increasing depth, to values of about 32‰ below 250 mbsf (see "Inorganic Geochemistry" section, this chapter). Temperature uncertainties have a much larger effect on assumed pore-water resistivity than do salinity uncertainties. Of our three available resistivity logs, we use the medium-penetration induction log, because it is less subject to borehole effects than is the spherically focused log and because it has higher vertical resolution than the deep induction log.

The constants a and m must be empirically determined for each locality; in unconsolidated sediments $a \approx 1$ and $m \approx 1.3$ (Archie, 1942). Physical properties measurements on cores from Site 888 suggest that $a \approx 1.44$ and $m \approx 1.76$. Because these constants and R_w are only approximately known, we considered the combined effects of both in our calculation of porosity, through regression of ϕ_n as a function of F. This regression yielded apparent values for a and m of 0.89 and 0.59, respectively, with a correlation coefficient $R = 0.57$.

Plots of the three porosity estimates over the logged intervals are presented in Figure 68. The in-pipe section of the neutron porosity log has not been corrected for pipe-collar effects. The neutron porosity and density-derived porosity (ϕ_d) are similar, with ϕ_n generally slightly lower than ϕ_d for the same depth range. Both neutron porosity and density-derived porosity decrease with depth to approximately 220 mbsf, and they gradually increase (~5%) from 220 mbsf to the bottom of the logged interval at about 500 mbsf. The resistivity-derived porosity (ϕ_r) log has a similar character, particularly in the upper 200 mbsf, but suggests a general trend of porosity decreasing with depth. This trend is somewhat dependent on our assumed pattern of increasing fluid conductivity with depth, caused by increasing temperature with depth. The resistivity-derived porosity log does not exhibit the porosity inversion evident in the neutron- and density-derived porosities. Such an inversion is unlikely to be present but obscured in the resistivity-derived porosity log, unless pore tortuosity increases with depth, resulting in a downhole increase in the coefficient m. Because neutron and especially density logs are more affected by hole washouts than is the resistivity log, the porosity inversions implied by the neutron and density logs may be artifacts. Post-cruise borehole correction of the neutron log will be required to resolve this uncertainty.

All three porosity estimates (ϕ_n, ϕ_d, and ϕ_r) show strong local porosity minima at 100 and 110 mbsf that correlate with indications of sandier sections in the gamma and caliper logs. The latter minimum correlates with sand intervals recovered within the 105–118 mbsf interval. In general, all three porosity estimates indicate that the sands within Unit I are consistently lower in porosity than are the silts. Within Unit II, however, silts and sands are more similar in porosity. In contrast to the relationship observed in Unit I, a local porosity minimum at 230 mbsf corresponds to a finer grained unit observed in Core 146-888B-26H.

Measurements of density and porosity from core are numerous above 200 mbsf and below 500 mbsf, but sparse between these depths (see "Physical Properties" section, this chapter). This sampling distribution complements the logging data distribution excellently: logs fill the 200–500 mbsf gap, and the 90–200 mbsf overlap zone of log and core measurements provides a check on the consistency of the two data types.

Core and log measurements of bulk density (Fig. 69) are generally similar. Obvious discrepancies are observed, however, in the interval from 80 to 170 mbsf and at 500 mbsf. Many core measurements between 80 and 170 mbsf are consistent with the logs, but some measurements in this and deeper intervals have much lower core densities, possibly resulting from core disturbance. Core density values below 500 mbsf are substantially higher than log values between 400 and 500 mbsf. As discussed previously, we suspect that many of the density-log values between 400 and 500 mbsf are erroneously low owing to the loss of pad contact. No such offset at 500 mbsf is present in the comparison of core and neutron-log porosities (Fig. 70). Core porosities are substantially higher than neutron porosities in the interval above 500 mbsf, and especially above 200 mbsf. Above 89 mbsf, this discrepancy can be attributed to through-pipe logging, but the discrepancy persists in the open hole.

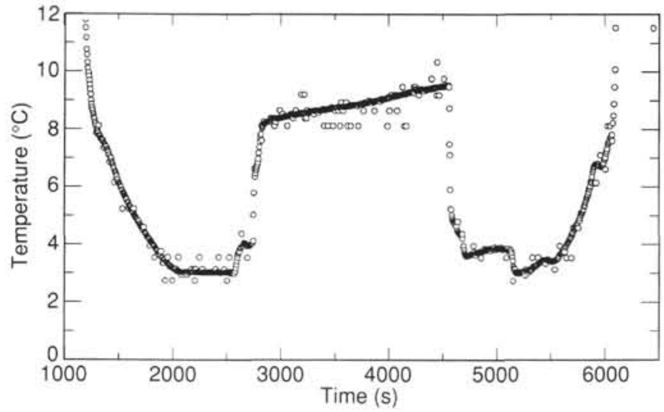

Figure 55. Temperature record from WSTP deployment in Hole 888B at 194.1 mbsf (Core 146-888B-22X).

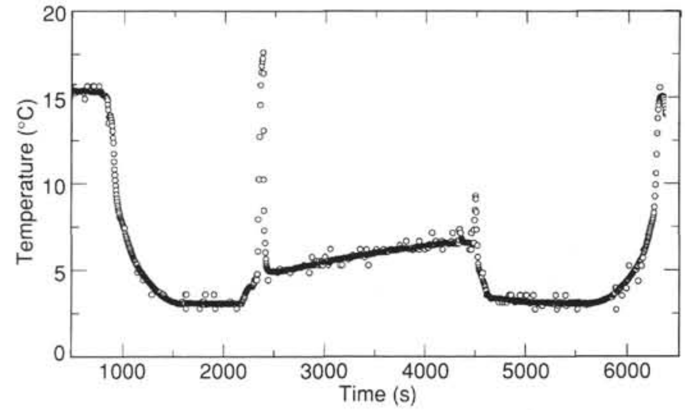

Figure 56. Temperature record from WSTP deployment in Hole 888B at 234.2 mbsf (Core 146-888B-27H).

Core rebound can be expected to cause slightly higher porosities at laboratory pressures than in situ, but rebound cannot account for the greater compatibility of densities than of porosities.

Core and log measurements of formation factor also exhibit systematic differences (Fig. 71) for which we cannot account. In-situ measurements of fluid resistivity are quite uncertain, but not enough to account for the large differences between core and log results in the range 80–180 mbsf.

Sonic Velocity

Sonic velocity at Site 888 generally increases with depth throughout the logged interval (Fig. 64). Velocities in the upper portion logged within Unit I (approximately 90–125 mbsf) are highly variable and show a strong correlation with the caliper and porosity logs in this region, indicating that high velocities correspond to sand units. Both the velocity and caliper logs show a relatively smooth increase from approximately 125 to 173 mbsf. The transition from Units I to II is marked by an increase in velocity and several high-velocity spikes between 173 and 193 mbsf. A pronounced baseline shift in velocity, as well as a decrease in the velocity gradient, marks the top of Unit II at 193 mbsf.

Velocity is a function of bulk modulus (κ), rigidity (μ), and bulk density (ρ): $V_p = [(\kappa + 4/3\,\mu)/\rho]^{1/2}$. Empirical data (e.g., Hamilton, 1978) show that increasing porosity causes a decrease in velocity, implying that the elastic moduli are more sensitive to porosity changes than is density. For example, the porosity minima observed at 100 and 110 mbsf are expressed as velocity maxima. The inverse relationship of velocity and porosity is clearly observed in Figure 72 down to a depth of 300 mbsf. Below 300 mbsf, velocity does not appear to be strongly dependent on porosity. In part, the weakness of this relationship may be attributable to inaccuracies in the density-based porosities; the lack of lithologic influence on porosity also inhibits a correlation (Fig. 67).

Time-Depth Relationship

To create synthetic seismograms, we derived a wavelet from the seismic-reflection data by averaging the seafloor reflection across 20 traces. This produced a symmetrical wavelet with a negative polarity peak (Fig. 73). We calculated two synthetic seismograms (Fig. 73), one assuming constant density and the other using the density log of Figure 63. Incorporating density values did not significantly change the resulting synthetic seismogram, except for the loss of several minor reflectors between 300 and 500 msbf. The good match of the synthetic seismogram to the seismic data provides time/depth conversion. Two of the logged horizons are readily identifiable in the seismic data: (1) the velocity maximum/porosity minimum at 105 mbsf correlates with a strong, laterally consistent reflector at 3530 ms and (2) the high-velocity peak marking the Unit II/III boundary at 457 mbsf lies at 3920 ms on the seismic section. The sign convention of the seismic profile is that a negative-polarity input wavelet corresponds to an impedance increase. Therefore, the large velocity increase marking the base of the transition zone between Units I and II at 193 mbsf is expressed as a negative reflection at 3640 ms.

The logging information provides significant additional detail on the thickness and character of the depositional units making up Unit II, where there was little core recovery. On the seismic-reflection section (Figs. 73–74), Unit I coincides with the upper seismic unit that is dominated by largely continuous reflections. Unit II corresponds with a seismic unit extending from 3615 to 3920 ms, characterized by laterally discontinuous reflections. This sandy sedimentary section of Unit II is interpreted as deposits of the prograding Nitinat Fan. Features resembling both channels (3630–3660 ms) and lobes (3900 ms) are observed in the seismic data. The top of Unit III correlates with a high-amplitude laterally continuous reflection at 3920 ms.

Temperature

The Lamont-Doherty Earth Observatory temperature tool was run at the bottom of the geophysical and well seismic tool (WST) tool strings. The data recorder from the tool run at the bottom of the geophysical tool string malfunctioned, preventing data recovery. Drilling-water circulation during the WST run substantially degraded the usefulness of the temperature data. The WSTP and ADARA measurements at this site indicate a thermal gradient of about 68°C/km and a bottom-water temperature of about 1°C (see "WSTP and ADARA Temperature Measurements" section, this chapter).

SUMMARY AND CONCLUSIONS

The general purpose of coring at Site 888 was to provide information on the age, lithology, physical properties, and geochemical characteristics of sediments near the continental margin before they have undergone the process of accretion, with its accompanying deformation and generation of fluid flow. In principle, such a reference site may also provide data on the sedimentary section that is thrust beneath the accretionary wedge and either subcreted beneath it or subducted. The holes at Site 888, however, only sampled the top quarter of the sedimentary sequence on the ocean floor. This top quarter has been part of the accreted section for about the last million years, and it is possible to infer from an interpretation of the seismic section how much of the incoming sedimentary section has been detached to form the accretionary wedge that comprises the outer part of the continental margin.

The sediments were deposited at lower bathyal water depths in a submarine fan system, which in its present form is the Nitinat Fan

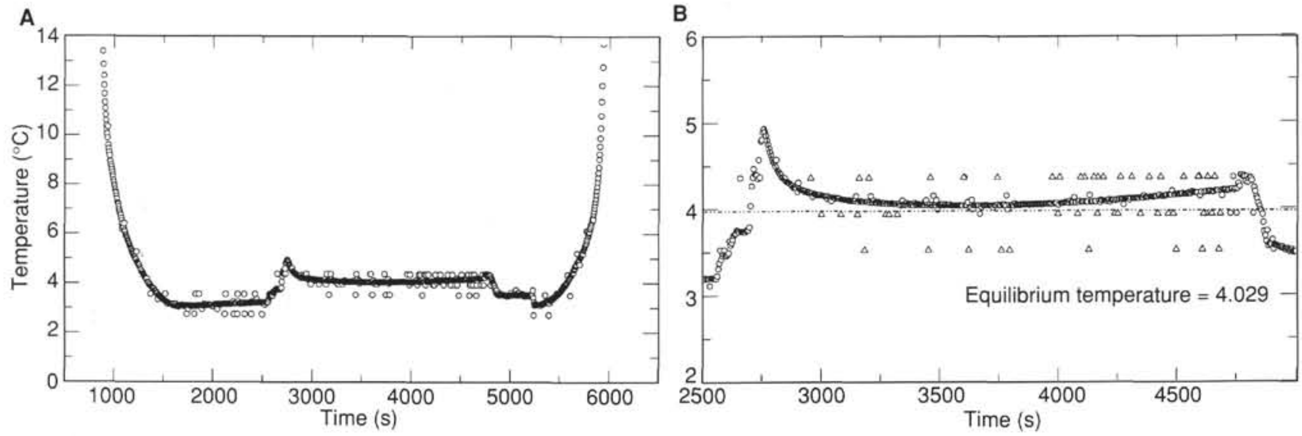

Figure 57. Records from WSTP deployment in Hole 888B at 267.8 mbsf (Core 146-888B-31H). **A.** Temperature record for entire run. **B.** Close-up of temperature record in sediment. Conventions as in Figure 51. Note change in both time and temperature scales for each plot.

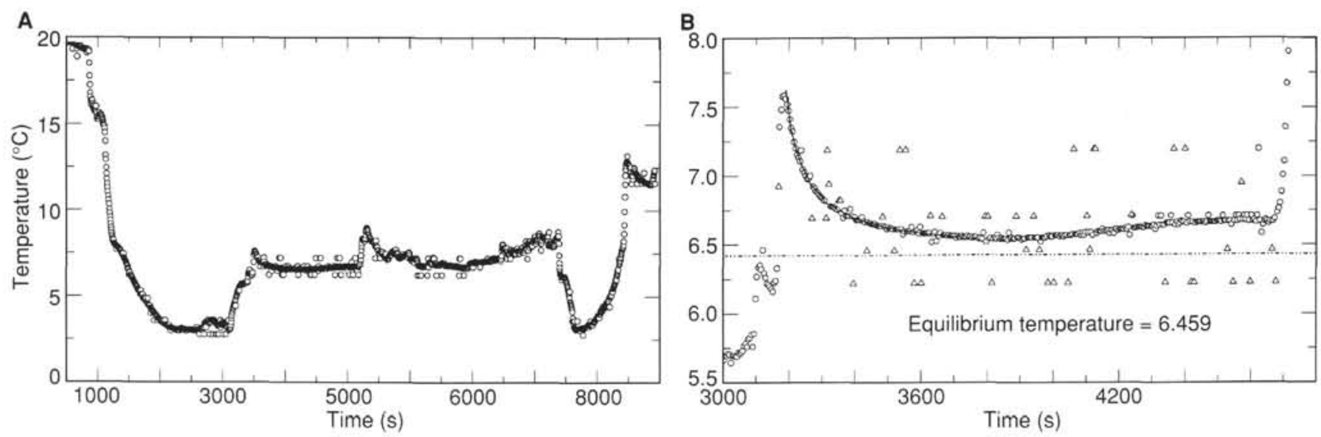

Figure 58. Records from WSTP deployment in Hole 888B at 404.5 mbsf (Core 146-888B-46X). **A.** Temperature record for entire run. **B.** Close-up of temperature record in sediment. Conventions as in Figure 51. Note change in time and temperature scales for each plot.

(Fig. 77). The magnetic polarity of the whole of the cored interval is normal, except for a short interval at 100 mbsf that may correspond to the Blake Event of 110,000 Ma. Radiolarians of the *Botryostrobus aquilonaris* Zone (less than 450,000 yr) were found to a depth of 170 mbsf. The dominance of sinistral *Neogloboquadrina pachyderma* in a normal polarity interval indicates that the cored section at Site 888 is younger than 600,000 yr.

Interpretation of seismic-reflection section 89-04 (Figs. 5–6) concurs with the general interpretation of the lithologies recovered in the cores in assigning Unit I (0–175 mbsf), with its predominance of clayey silts, to the outer fan, Unit II (193–457 mbsf) of mainly sands to the middle fan, and Unit III (457–567 mbsf) to a more distal part of the outer fan than Unit I. The seismic section shows that most of the section below the maximum depth of the boreholes is composed of what appear to be distal turbidites. The section also shows that the upper few hundred meters of section in and near the toe of accretionary wedge is generally made up of units with a more distal character than those penetrated by the holes at Site 888. In the region farther north, in the preaccretion sediment sequence on the ocean floor west of Site 889, seismic section 89-08 (Fig. 1 in "Sites 889 and 890" chapter, this volume) shows no fan-related units of the type penetrated at Site 888. From these observations, we may expect that the sediments in the accretionary wedge in the quadrant to the north and east of Site 888 are more likely to be like the clayey silts with thin sand interbeds of Units I and III than the more massive sands of Unit II. The presence of the more proximal facies cannot, however, be excluded, especially in the older part of the accreted section. In the quadrants to the east and south of Site 888, it is probable that a high proportion of the accreted sediments will be sands from the Nitinat Fan or its predecessors.

The sediments recovered in the cores showed no evidence of deformation that was unequivocally of tectonic origin. Apart from the effects of drilling disturbance, the few structures observed could all be explained as synsedimentary deformation associated with local gravitational slumping and water escape.

The porosity of the sediments is an important parameter for calculating the amount of water that is taken into the accretionary wedge and expelled from it during subsequent deformation and compaction. The distribution of porosity with depth in the sedimentary section off Vancouver has been estimated from seismic velocity data by Davis et al. (1990) and by T. Yuan, G.D. Spence, and R.D. Hyndman (unpublished data) for the purpose of assessing the distribution of fluid outflow from the accretionary wedge. We have six measures of porosity available to us from the data collected at Site 888, which are direct measurements on samples using a pycnometer, converted GRAPE measurements on sections of core, and derived measurements from the density, neutron, resistivity, and sonic logs (the last using the porosity-velocity relation of Hyndman et al., 1993). Although these measures all show a general decrease in porosity with depth, they can yield values of porosity that are consistently different, by as much as 10%, in different sections of the hole (Fig. 75).

Within Unit I, the rate of increase of porosity with depth is greater than that predicted by normal compaction curves for similar types of sediment, predominantly clayey silts (Brückmann, 1989). Part of this discrepancy probably arises from the inadequacy of the exponential

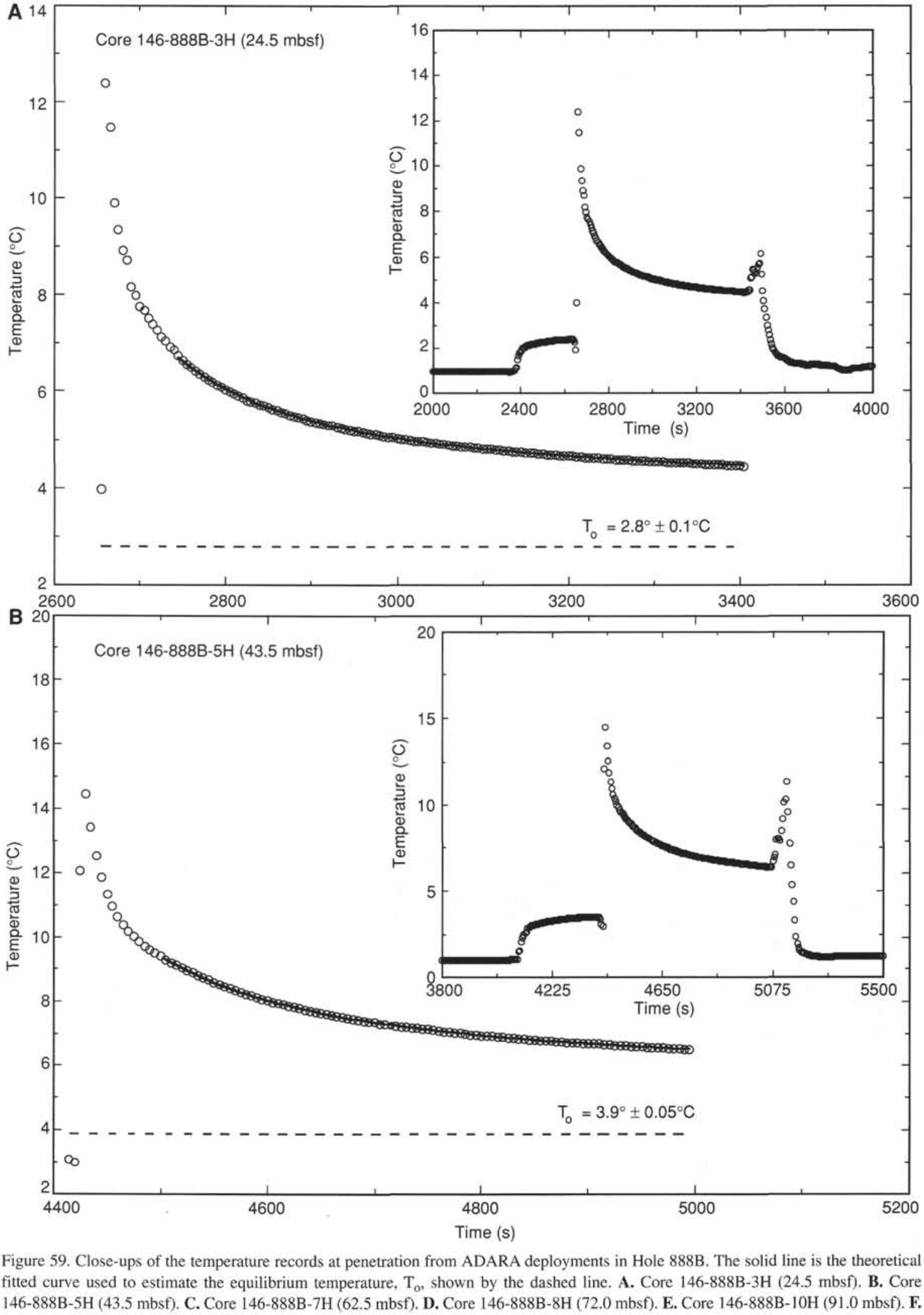

Figure 59. Close-ups of the temperature records at penetration from ADARA deployments in Hole 888B. The solid line is the theoretical fitted curve used to estimate the equilibrium temperature, T_o, shown by the dashed line. **A.** Core 146-888B-3H (24.5 mbsf). **B.** Core 146-888B-5H (43.5 mbsf). **C.** Core 146-888B-7H (62.5 mbsf). **D.** Core 146-888B-8H (72.0 mbsf). **E.** Core 146-888B-10H (91.0 mbsf). **F.** Core 146-888B-11H (100.5 mbsf). **G.** Core 146-888B-34H (300.5 mbsf). The inserts show both penetration (initial spike followed by exponential decay) and bottom-seawater (low temperatures at beginning and end of record) temperature records.

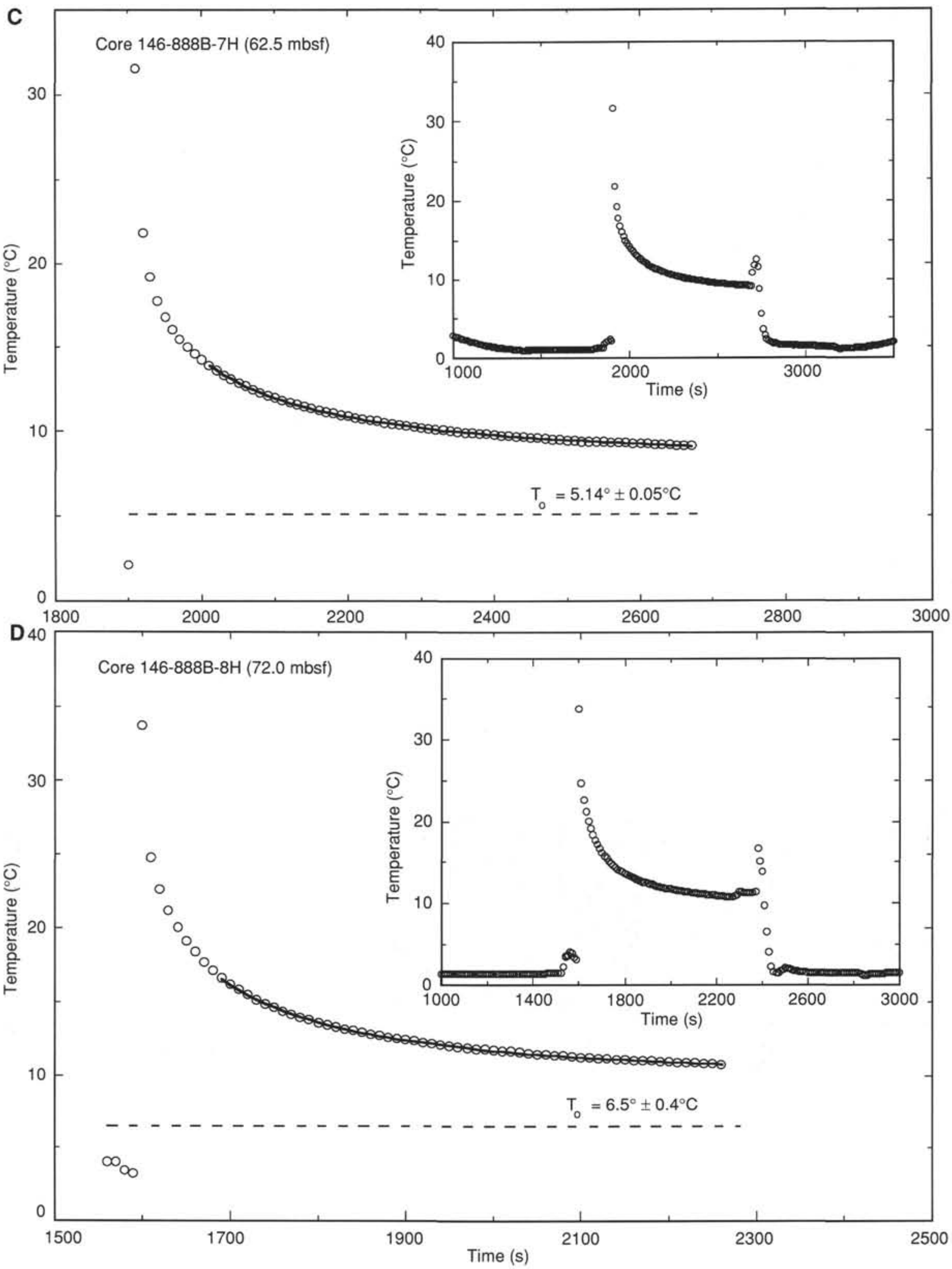

Figure 59 (continued).

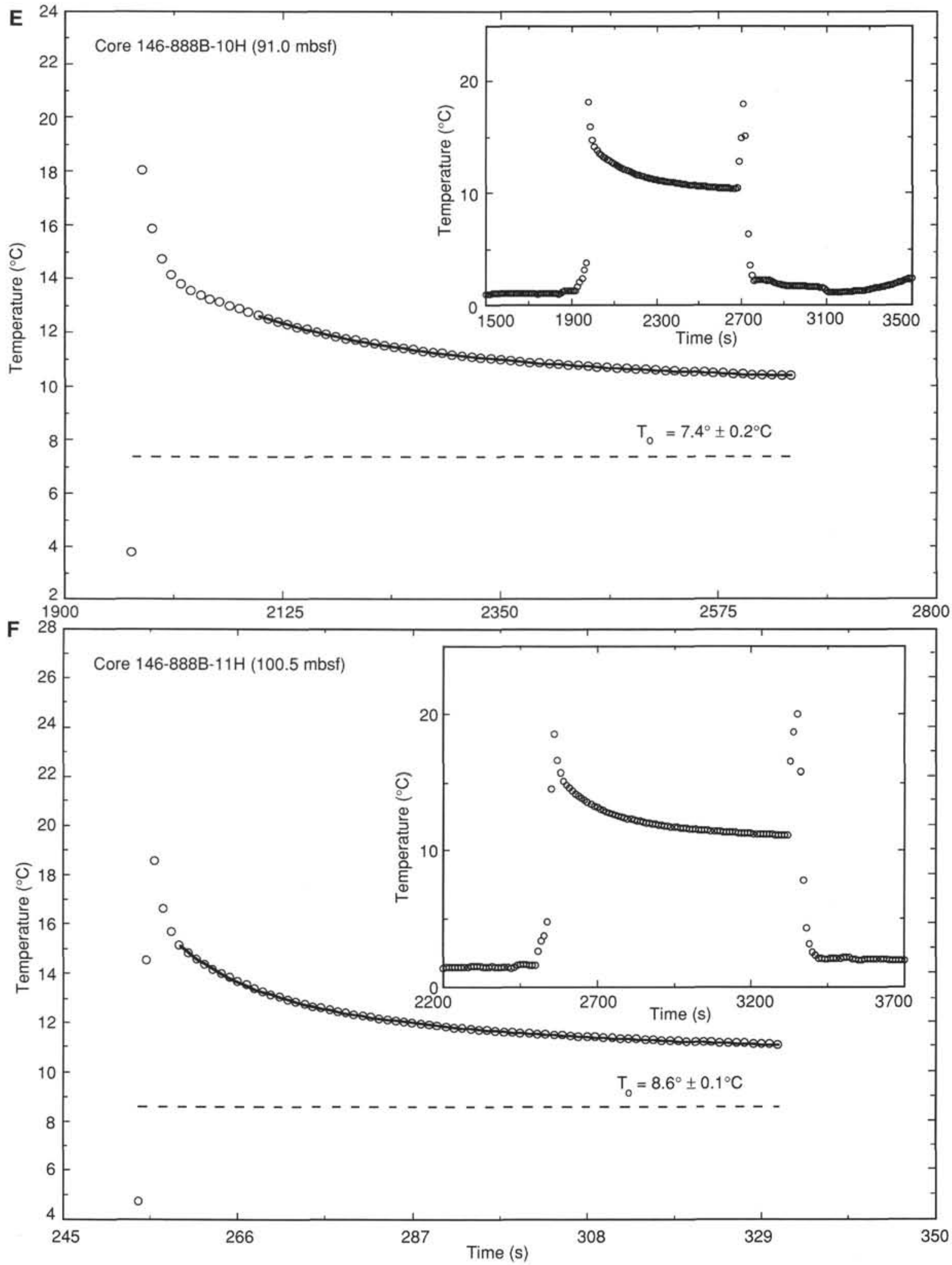

Figure 59 (continued).

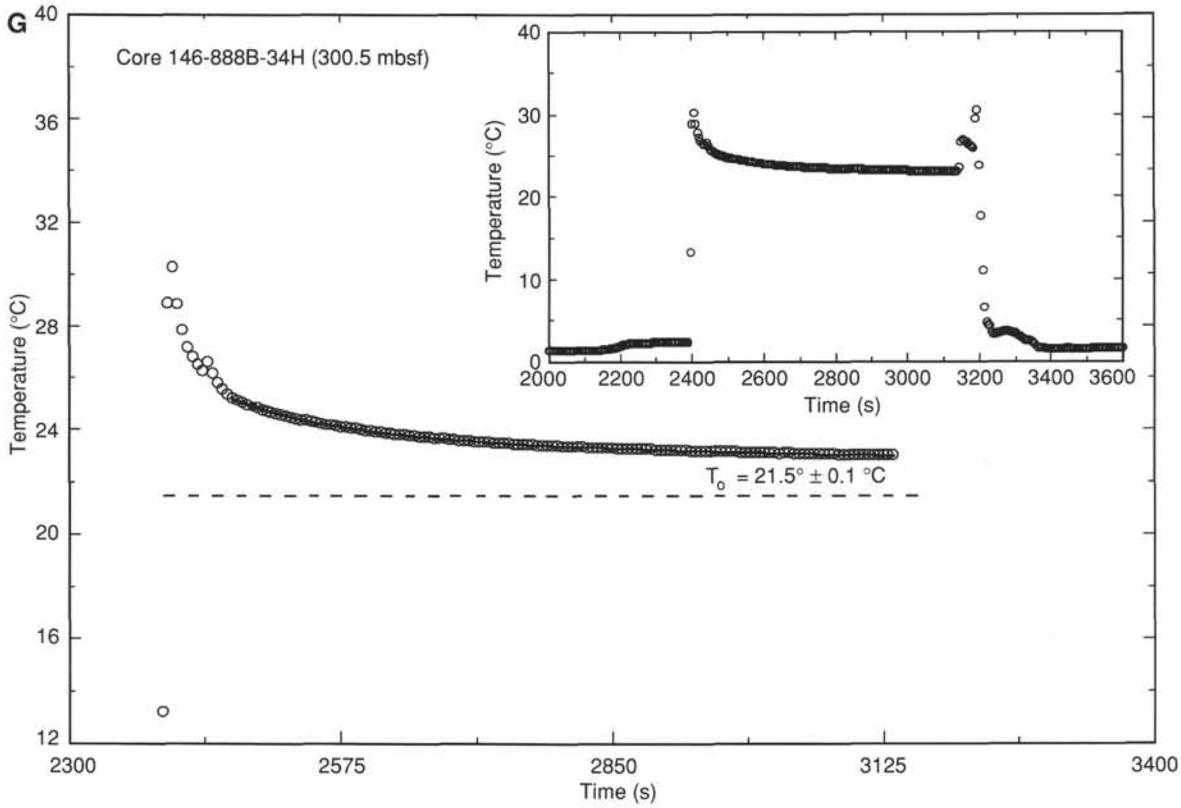

Figure 59 (continued).

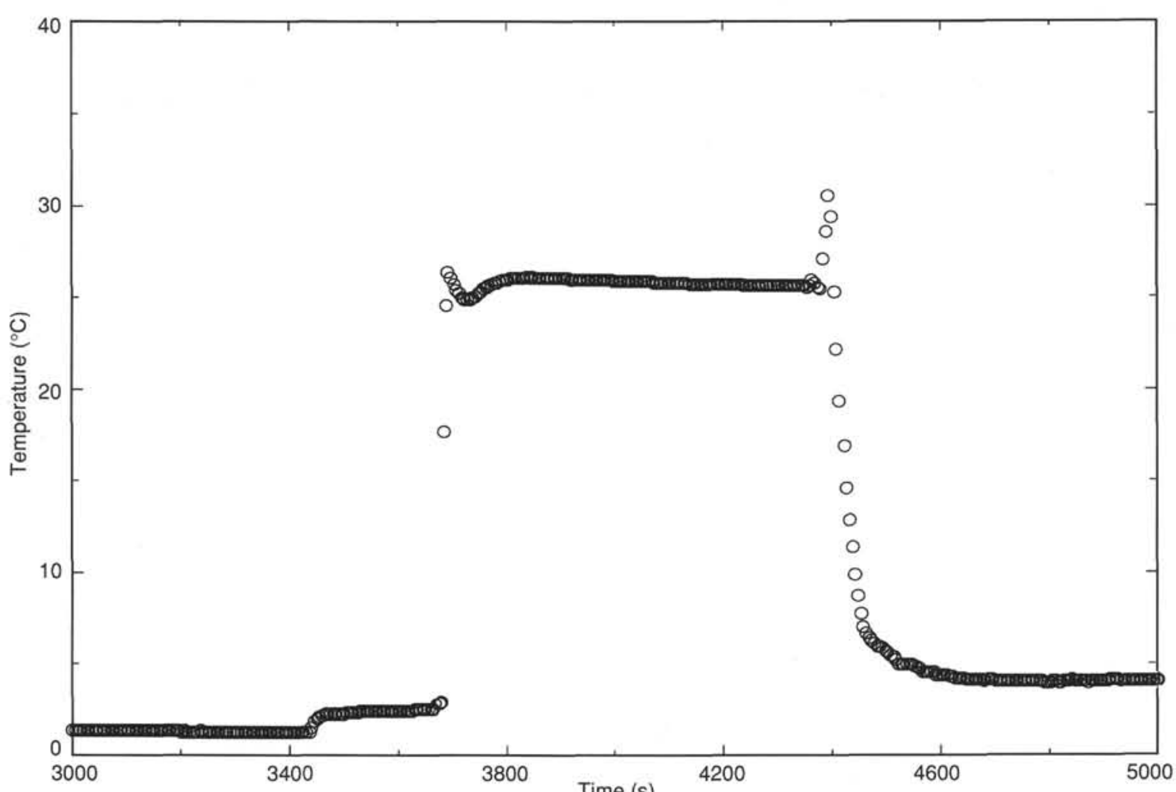

Figure 60. Penetration and bottom-seawater temperature records from ADARA deployment in Hole 888B at 329 mbsf (Core 146-888B-37H).

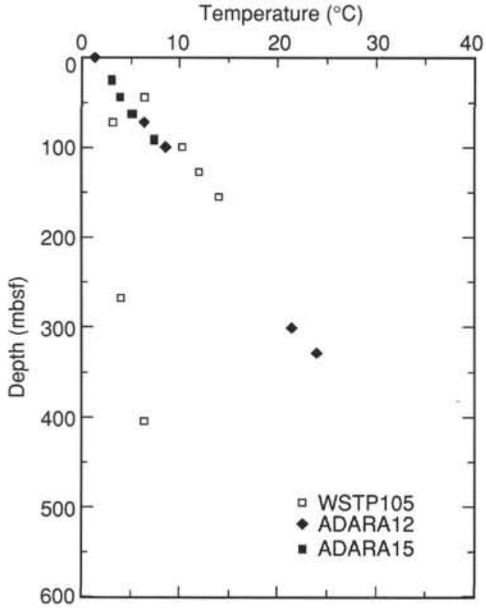

Figure 61. Temperature measured with the WSTP and ADARA vs. depth in Hole 888B (data uncorrected for bottom-seawater intercalibration).

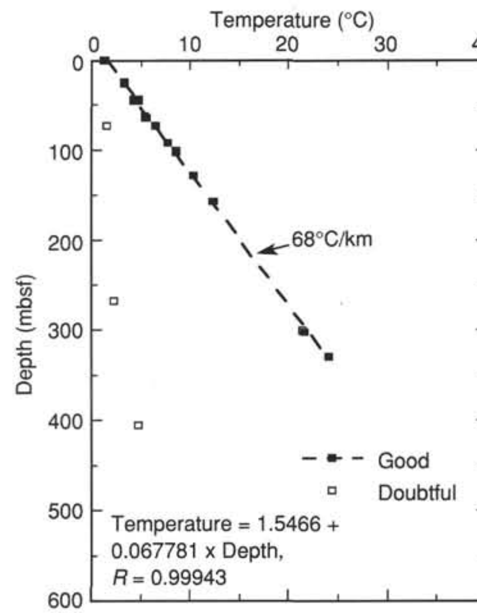

Figure 62. Temperature vs. depth in Hole 888B from WSTP and ADARA data corrected for bottom-seawater intercalibration. The dashed line shows the linear least-squares regression to temperature with depth, excluding the three data points of doubtful quality.

form of the reference curves to match the rapid change of porosity with depth in the top 20 or 30 m, but beyond that interval, the main trend of the porosity-depth data shows porosity that is 10% less than predicted in the interval 100–200 mbsf. This difference is, in part, an effect of the presence of sands, which have a more abrupt reduction of porosity with depth than the clayey silts or silty clays (Fig. 75), but the measured porosity lies well below Brückmann's sand curve also. On this evidence alone, it would appear that Unit I is overcompacted, but the ratios of shear strength to effective stress measured on samples from Unit I indicate that it is strongly underconsolidated (see "Physical Properties" section, this chapter).

In the upper part of Unit II, the logs give similar values of porosity, in the mid to low forties of percentage. The values are generally lower than those obtained from measurement on core samples, but this difference is attributable to the selective sampling of the more clay-rich sediments enforced by the poor core recovery. Where there are intervals of clayey silt within Unit II, the porosities derived from the logs are closer to those obtained from samples. Porosity varies little with depth in Unit II, which is suggestive of rapid deposition, producing little difference in the mechanical compaction of the top or bottom of the unit, and of a downward fining in the average grain size. The bottom of the unit should be underconsolidated, but it lies on the low-porosity side of the normal compaction curve for sands. The consistent deviation of the log-derived porosity values from this sand reference curve of Brückmann (1989) is probably, in part at least, a consequence of the inappropriateness of the reference curve. It is derived from laboratory measurements on samples that have not been corrected for in-situ conditions, and sands are poorly represented in the ODP data set from which the curves are derived.

Within Unit III, the values of porosity derived from the resistivity and sonic logs show a decrease in porosity with depth. The sample-derived porosity shows a similar trend, although the absolute values are higher (the samples have not been corrected for the effect of elastic rebound). The porosities derived from density and neutron logs trend toward low values for a reason that is not yet understood.

There are clear differences between the logs in their response to different lithologies. The logs are also affected differently by the width and rugosity of the bore hole. Resistivity, especially that derived from the induction log, is least affected, and in Figure 76 a comparison is made between the porosity derived from the density, neutron, and sonic logs, normalized to porosity derived from the resistivity log. Sonic-derived porosity is higher than resistivity-derived porosity in the clayey silts of Unit I. Between 102 and 117 mbsf, the sonic/resistivity ratio decreases and the density/resistivity ratio increases in an interval in which several sand layers occur. In Unit II, above 300 mbsf, the neutron/resistivity and density/resistivity ratios are lower than the sonic/resistivity ratio, but in the lower part of Unit II, they all have similar values. The poor recovery of core from Unit II makes it difficult to correlate this change at 300 mbsf with any obvious change in lithology. It is possible, however, that partial cementation may have helped arrest the compaction of the lower sequence, increasing its seismic velocity by increasing its rigidity, and increasing its resistivity by increasing the tortuosity of the pore spaces, but leaving the overall porosity little changed.

The porosities derived from measurements at Site 888 match broadly, in the overall shape of their distribution with depth, the porosity derived from seismic velocities obtained from the multichannel seismic data of line 89-04 (T. Yuan, R.D. Spence, and R.D. Hyndman, unpubl. data) using the empirical porosity-velocity relation of Hyndman et al. (1993). The absolute values of the porosity data from Site 888 are, however, generally about 4% higher. On this basis, the fluid content of the top kilometer of the sediment accreted to the wedge would be underestimated from the seismic-reflection velocity data from the drill site and elsewhere in the region of the Cascadia Basin close to the accretionary wedge (T. Yuan, R.D. Spence, and R.D. Hyndman, unpubl. data). These authors as well as Hyndman and Davis (1992), in their estimate of fluid flux bringing methane to the gas hydrate formed beneath the continental margin, use a best-fit porosity-depth function in which porosity = 0.6exp(–depth/1.5) for the whole of the undeformed sedimentary section. This function overestimates the porosity in the cored interval of Site 888, below 100 mbsf, by about 3% on average, and yields an error of about 2% in the estimate of the total fluid content of the sedimentary section.

The measurements of temperature in Hole 888B yielded a remarkably linear geothermal gradient of 68°C/km (see "WSTP and ADARA Temperature Measurements" section, this chapter). From the almost linear increase of thermal conductivity with depth in Unit I (see "Physical Properties" section, this chapter), this geothermal gradient

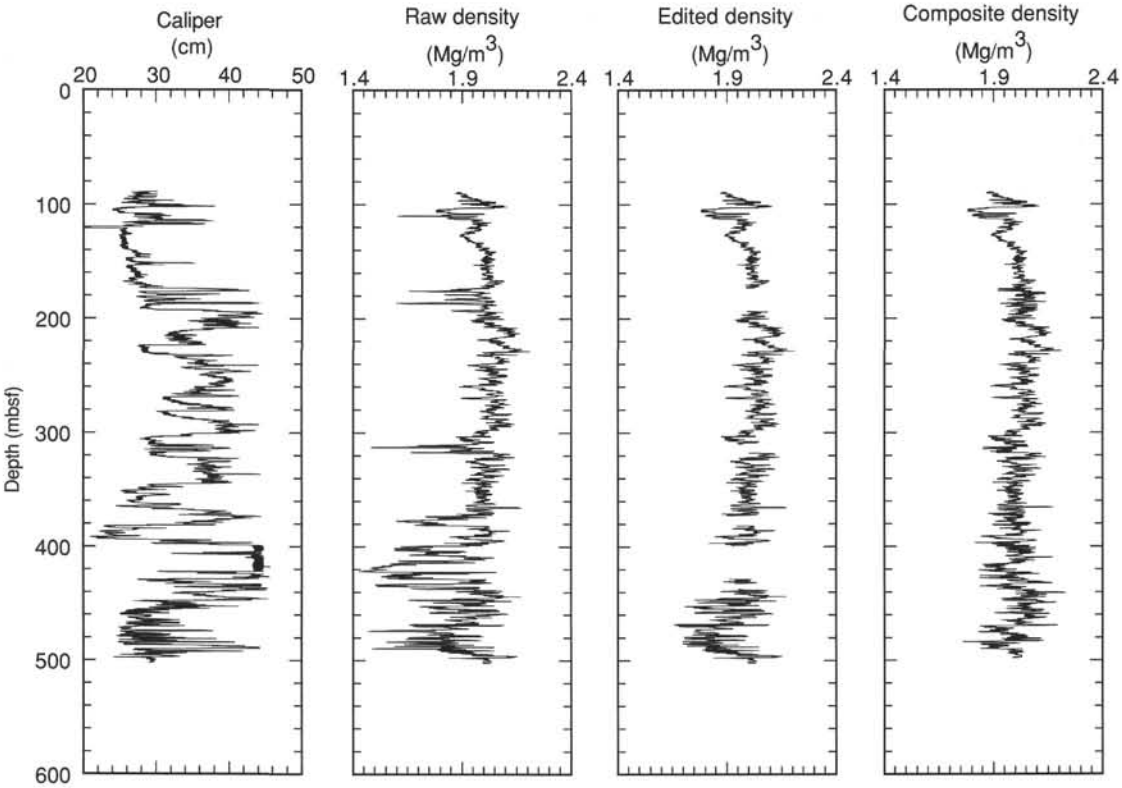

Figure 63. Logs of hole diameter (caliper), raw density data, edited density curve, and composite density curve derived from edited density, with gaps and the lower hundred meters filled with pseudodensity from neutron porosity.

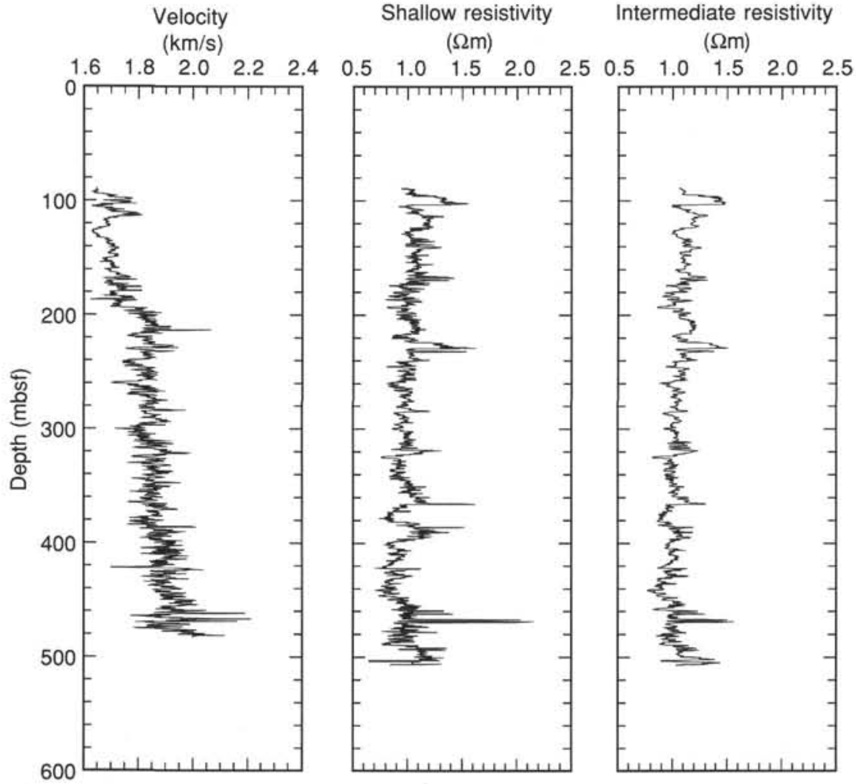

Figure 64. Logs of velocities from sonic traveltimes, shallow resistivity, and intermediate resistivity.

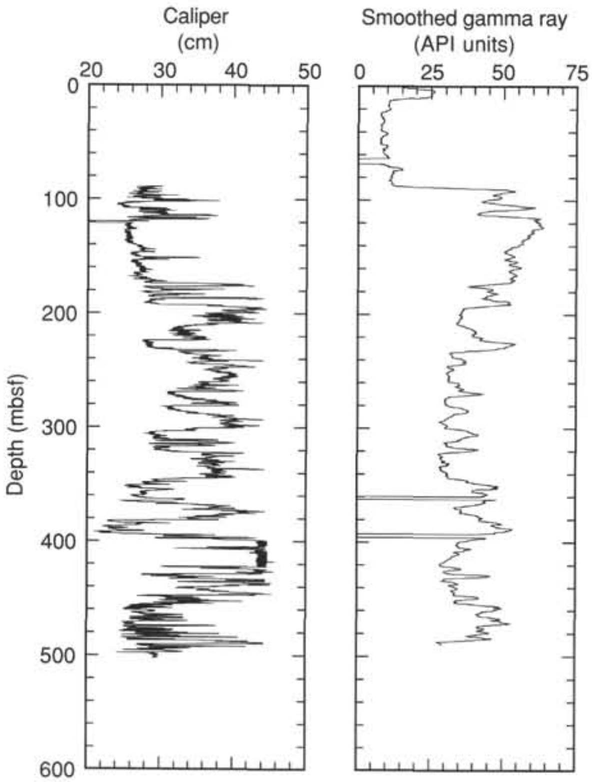

Figure 65. Logs of hole diameter (caliper) and smoothed gamma ray. Gamma-ray data above 89 mbsf are reduced in value because of through-pipe logging.

yields an increase in heat flow from 78 mW/m^2 near the seabed to 94 mW/m^2 at 193 mbsf, remaining constant at 94 mW/m^2 below this level. The near-surface heat flow is much less than the average value of 115 mW/m^2 for measurements made with heat-flow probes in the vicinity of Site 888 (Davis et al., 1990). Such a large difference is a matter for concern, as both sets of measurements appear to have been taken in a reliable way. A possible explanation may be that a reduction in the bottom-water temperature over the last few years modulated by seasonal variation could have increased the geothermal gradient near the seabed sufficiently to give a high gradient that was sufficiently linear to appear to be steady state in the measurements from the heat-flow probes in the seabed, yet the effect of the change had not diffused sufficiently deeply to be noticeable in the shallowest temperature measurements in the borehole (after 10 yr, a constant change in bottom-water temperature of 0.3°C would produce a change of only 0.05°C at a depth of 25 mbsf, but a change of 0.23°C at a depth of 5 mbsf would increase a gradient of 68°C/km measured over the uppermost 5-m interval to 81°C/km) (Carslaw and Jaeger, 1959). The measured temperature of the bottom water is 1.29°C, and the seabed temperature predicted from the best-fitting straight line to borehole temperature measurements is 1.54°C. This is in the right sense for a cooling of bottom-water, but it is a small difference that could be explained by changes in thermal conductivity near the seabed.

The geochemistry of the pore water in the section varies downward in response to bacterial sulfate reduction, carbonate diagenesis, and fluid flow within some intervals. The variations in several species are, however, quite moderate in comparison with the other sites, such as Site 889, in the accretionary wedge. For example, chloride varies between 543 and 571 mM at Site 888, but at Site 889 chloride varies between 350 and 550 mM. Organic carbon is refractory and present in low concentrations (0.2–0.4 wt%). The concentrations of methane in Unit I are less than 5 ppmv. The methane is of bacterial origin.

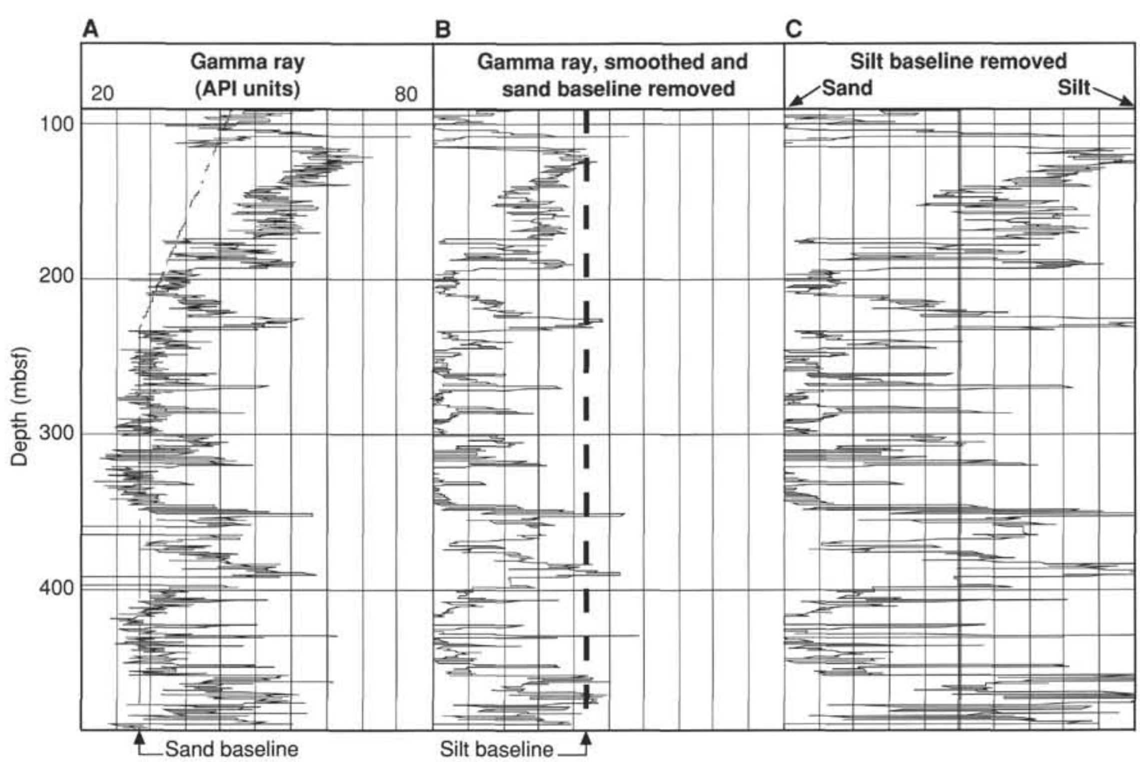

Figure 66. Gamma-ray log adjusted to show lithologic variations. **A.** Raw gamma-ray log showing sand baseline values (dashed line). **B.** Smoothed gamma-ray log with sand baseline removed and silt baseline shown. **C.** Gamma-ray values with silt baseline removed. The total variation in **C** is interpreted as the sand-silt range of the logged section.

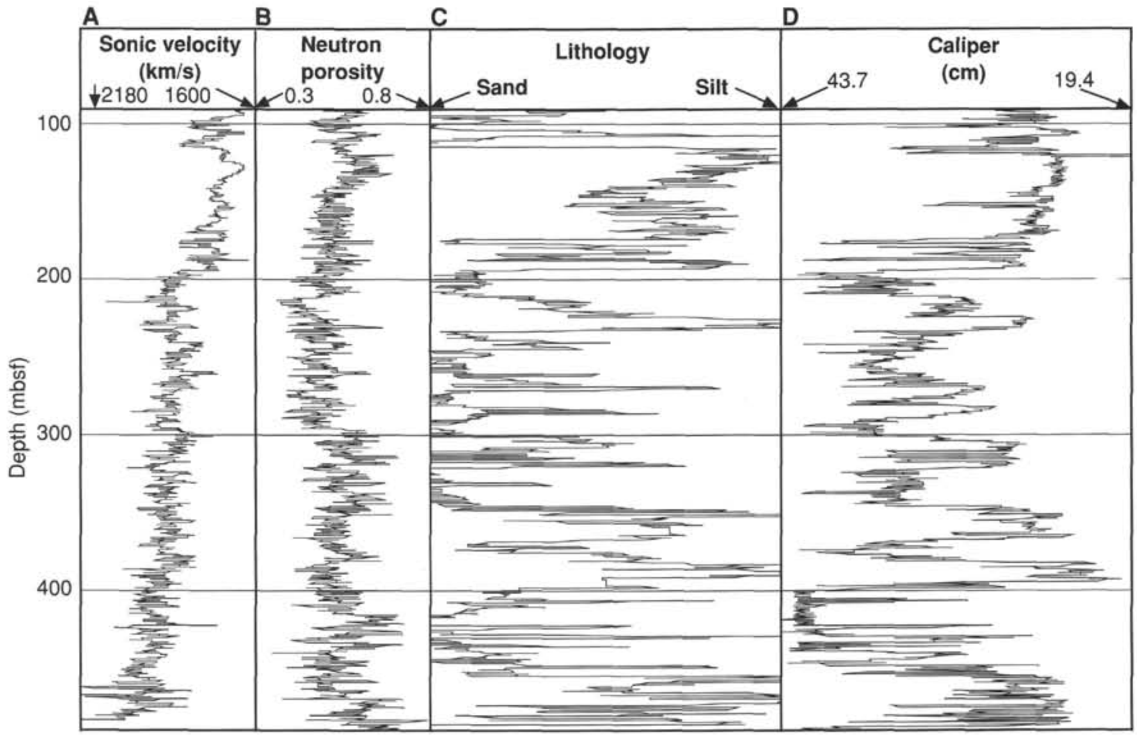

Figure 67. Comparison of lithologically sensitive logs. **A.** Sonic velocity. **B.** Neutron porosity. **C.** Lithology (from Fig. 66). **D.** Hole diameter (caliper). Note in-phase variations in lithology and caliper logs. The low values of sonic velocity and high neutron porosity, silt-rich nature, and small hole diameter correlate in Unit I and the transition zone, which occur above 193 mbsf.

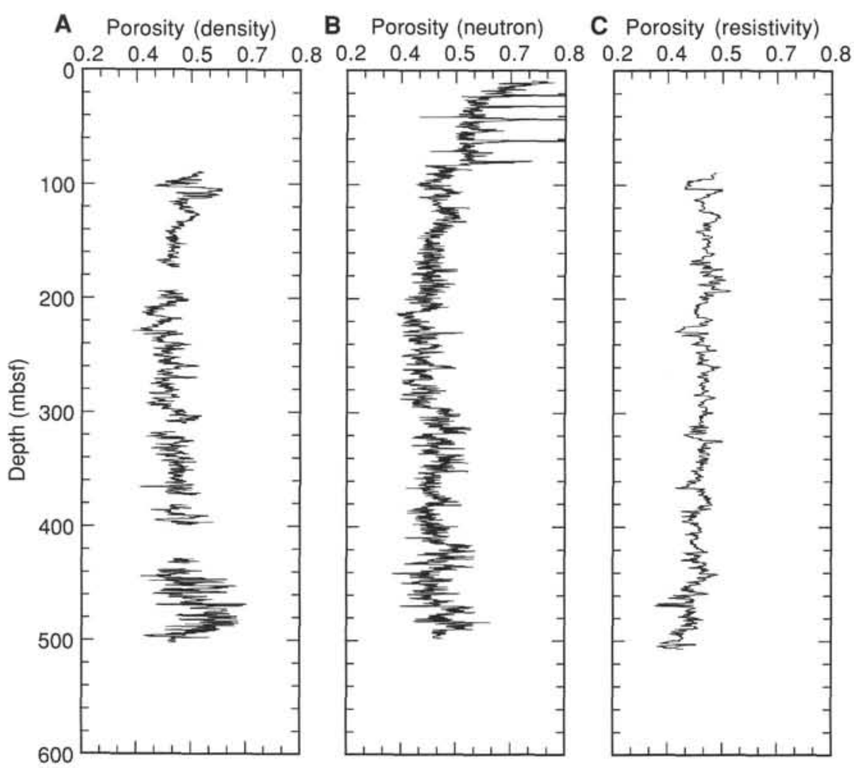

Figure 68. Porosity estimates from **(A)** edited density log shown in Figure 63, **(B)** neutron log, and **(C)** resistivity log.

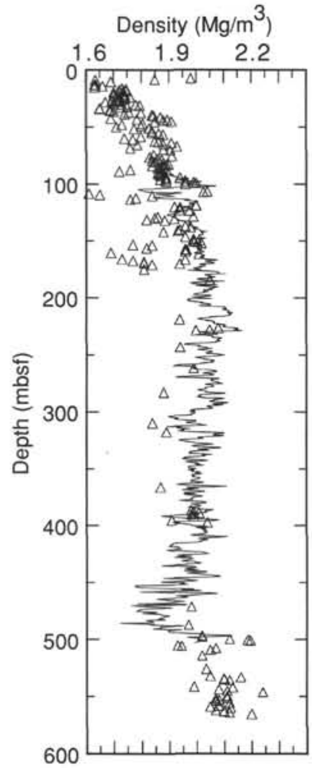

Figure 69. Comparison of density measured from core samples (triangles) with the edited bulk density from the geophysical tool string (line). Both core and log data are smoothed for comparison. Logged interval begins at 89 mbsf and ends at 503 mbsf.

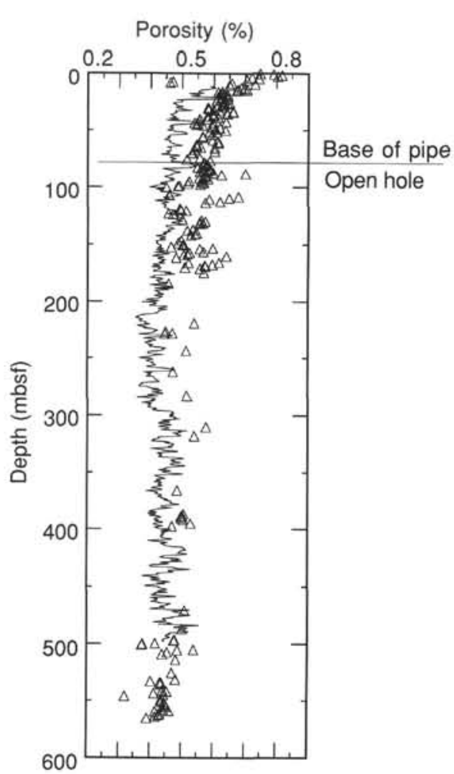

Figure 70. Comparison of fractional porosities measured in cores (triangles) with those measured by the neutron porosity log data (line). Neutron-log data for 0–89 mbsf are affected by logging through pipe. Both the core and log data are smoothed for correlation.

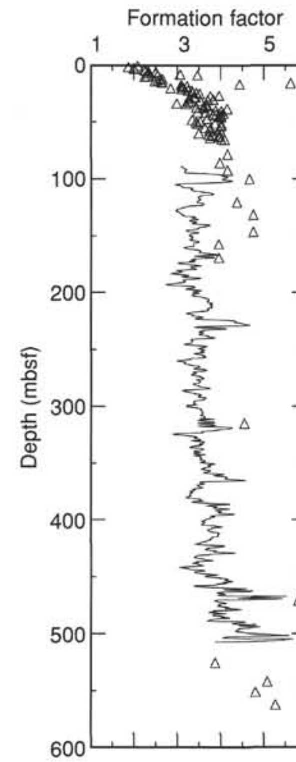

Figure 71. Comparison of formation factor determined from resistivity measurements on core (triangles) and from the intermediate resistivity log (line). Both core and log data are smoothed for comparison.

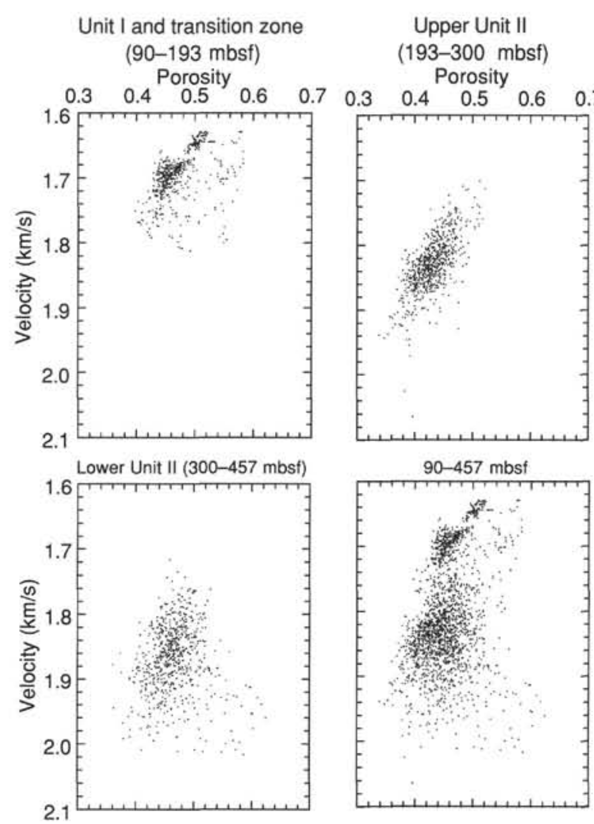

Figure 72. Velocity plotted as a function of density-based porosity for specified depth intervals.

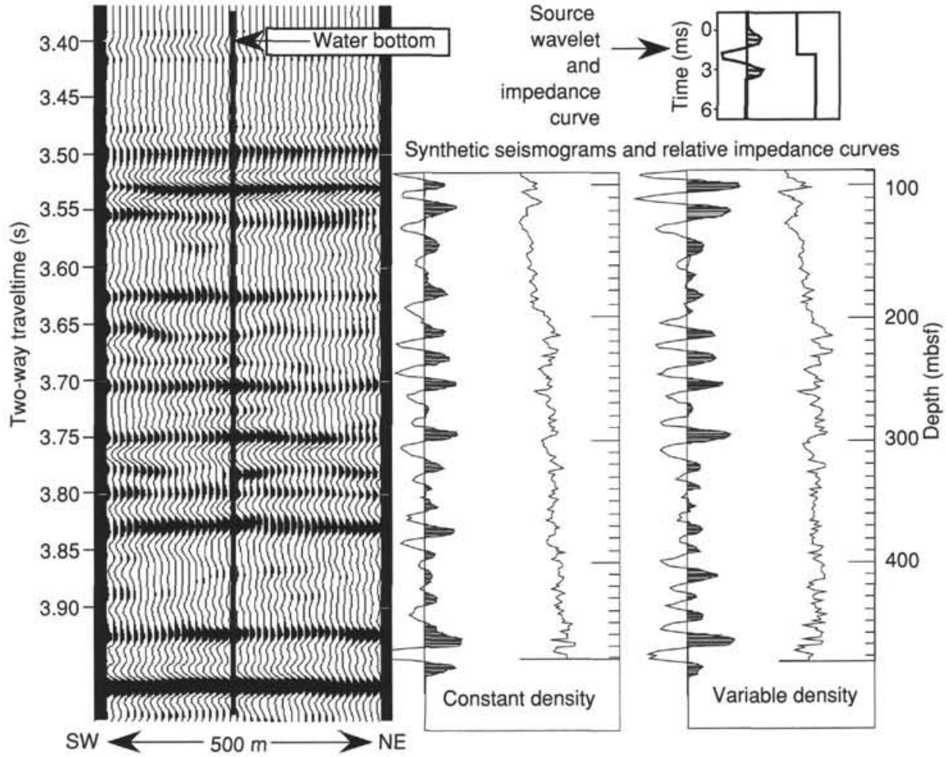

Figure 73. Comparison of seismic line 89-04 (see "Seismic Stratigraphy" section, this chapter) with synthetic seismograms generated by convolving the source wavelet (upper right) with an impedance curve based on the log-based velocity curve and either a constant density or the variable density log derived from a combination of information from density and neutron tools (Fig. 63).

Ethane, propane, and butane are present only in trace amounts ($C_1/C_2 > 1000$). Within Unit II at 351 mbsf, there is an anomalously high methane concentration of 27,698 ppmv in a high-porosity sand. It is not clear that this gas was formed in situ, yet the inorganic fluid chemistry gives no indication of fluid flow. It is possible that this is an example of gas migrating into the bed independently of the movement of pore water. Elsewhere, there is evidence of fluid flow, such as at 514 mbsf, where a pronounced minimum in chloride of 18 mM below surrounding values needs fluid flow to prevent it from diminishing by diffusion.

In a 10-m-thick interval at 94 mbsf, a small occurrence of methane coincides with a pronounced minimum in sulfate, which decreases from about 25 mM at the surface to zero or near zero between 87 and 103 mbsf, then rises sharply to 10 mM at 110 mbsf, before decreasing to zero values below 200 mbsf. Magnesium and calcium also show a local minimum and maximum, respectively, and alkalinity and ammonia a maximum, at 94 mbsf. The interval at about 94 mbsf is sandy, with high porosity, and contains wood fragments. Bacterial reduction is the cause of its disappearance of sulfate with increasing depth, and in the absence of the sulfate, methanogens produce the methane associated with the sulfate minimum. Another process, however, is required to produce two minima. This could occur if the interval of the shallower minimum was enriched in labile organic carbon, promoting higher bacterial activity, or if the layer was a flow path of sulfate-depleted pore water from deeper in the section or a migration path for methane. The layer of the shallower sulfate minimum is at an unconformity truncating gently dipping beds. Another possible cause of the two sulfate minima would be the rapid deposition of a thick unit that would isolate the older, lower sulfate-reduction zone from the younger zone formed above it at subsequently lower rates of sedimentation.

To conclude, the sedimentary section investigated at Site 888 results from active sedimentation in a fan system, with rapid but varying rates of sedimentation, that has produced variation in lithology, in compaction, and in its organic and inorganic geochemistry. The lower part of the section, at least, is undercompacted. The mid-fan sands of Unit II are apparently uncharacteristic of most of the sedimentary section that is fed to the accretionary wedge off Vancouver. Within the fan there has been local fluid flow, presumably induced by differential compaction between laterally varying sediment bodies. There may be flow of fluids transmitted from the region of the toe of the accretionary wedge, but this has not been unequivocally demonstrated from the data, so far. The heat flow through the section is unexpectedly low. The section is undeformed, showing no sign of transmission of stress from the accretionary wedge, 7 km to the east.

REFERENCES*

Archie, G.E., 1942. The electrical resistivity log as an aid in determining some reservoir characteristics. *Trans. Am. Inst. Min. Metall. Pet. Eng.*, 146:54–62.

Athy, L.F., 1930. Density, porosity and compaction of sedimentary rocks. *AAPG Bull.*, 14:1–24.

Borradaile, G.J., Keeler, W., Alford, C., and Sarvas, P., 1987. Anisotropy of magnetic susceptibility of some metamorphic minerals. *Phys. Earth Planet. Inter.*, 48:161–166.

Broglia, C., and Ellis, D., 1990. Effect of alteration, formation absorption, and standoff on the response of the thermal neutron porosity log in gabbros and basalts: examples from Deep Sea Drilling Project-Ocean Drilling Program sites. *J. Geophys. Res.*, 95:9171–9188.

Brückmann, W., 1989. Typische Kompakationsmuster mariner Sedimente und ihre Modifikation in einem rezenten Akkretionskeil (Barbados Ridge). *Beitr. Geol. Inst. Univ. Tübingen, Rh. A*, 5:1–135.

Cande, S.C., and Kent, D.V., 1992. A new geomagnetic polarity time scale for the Late Cretaceous and Cenozoic. *J. Geophys. Res.*, 97:13917–13951.

*Abbreviations for names of organizations and publication titles in ODP reference lists follow the style given in *Chemical Abstracts Service Source Index* (published by American Chemical Society).

Carslaw, H.S., and Jaeger, J.C., 1959. *Conduction of Heat in Solids* (2nd ed.): Oxford (Clarendon Press).

Claypool, G.E., and Kaplan, I.R., 1974. The origin and distribution of methane in marine sediments. *In* Kaplan, I.R. (Ed.), *Natural Gases in Marine Sediments:* New York (Plenum), 99–140.

Daniels, L., Fulton, G., Spencer, R.W., and Orme-Johnson, W.H., 1980. Origin of hydrogen in methane produced by *Methanobacterium thermoautotrophicum. J. Bacteriol.,* 141:694–698.

Davis, E.E., Currie, R., and Sawyer, B., 1987. Marine geophysical maps of Western Canada: Southern Vancouver Island Margin. *Geol. Surv. Can.,* Map 15-1987.

Davis, E.E., and Hyndman, R.D., 1989. Accretion and recent deformation of sediments along the northern Cascadia subduction zone. *Geol. Soc. Am. Bull.,* 101:1465–1480.

Davis, E.E., Hyndman, R.D., and Villinger, H., 1990. Rates of fluid expulsion across the northern Cascadia accretionary prism: constraints from new heat flow and multichannel seismic reflection data. *J. Geophys. Res.,* 95:8869–8889.

Dekkers, M., 1988. Some rock-magnetic properties of fine-grained hematite, goethite, and pyrrhotite [Ph.D. dissert.]. Univ. of Utrecht.

Hamilton, E.L., 1978. Sound velocity-density relations in sea-floor sediments and rocks. *J. Acoust. Soc. Am.,* 63:366–377.

Hays, J.D., 1970. Stratigraphy and evolutionary trends of radiolaria in North Pacific deep sea sediments. *In* Hays, J.D. (Ed.), *Geological Investigations of the North Pacific.* Mem.—Geol. Soc. Am., 126:185–218.

Hyndman, R.D., and Davis, E.E., 1992. A mechanism for the formation of methane hydrate and seafloor bottom simulating reflectors by vertical fluid expulsion. *J. Geophys. Res.,* 97:7025–7041.

Hyndman, R.D., Moore, G.F., and Moran, K., 1993. Velocity, porosity, and pore-fluid loss from the Nankai subduction zone accretionary prism. *In* Hill, I.A., Taira, A., Firth, J.V., et al., *Proc. ODP, Sci. Results,* 131: College Station, TX (Ocean Drilling Program), 211–220.

Hyndman, R.D., Yorath, C.J., Clowes, R.M., and Davis, E.E., 1990. The northern Cascadia subduction at Vancouver Island: seismic structure and tectonic history. *Can. J. Earth Sci.,* 27:313–319.

Jackson, M., Sprowl, D., and Elwood, B., 1986. Anisotropies of partial and anhysteretic remanence and susceptibility in compacted black shales: grain-size- and composition-dependent magnetic fabric. *Geophys. Res. Lett.,* 16:1063–1066.

Jarrard, R.D., Dadey, K.A., and Busch, W.H., 1989. Velocity and density of sediments of Eirik Ridge, Labrador Sea: control by porosity and mineralogy. *In* Srivastava, S.P., Arthur, M.A., Clement, B., et al., *Proc. ODP, Sci. Results,* 105: College Station, TX (Ocean Drilling Program), 811–835.

Krs, M., Krsová, M., Pruner, P., Zeman, A., Novák, F., and Jansa, J., 1990. A petromagnetic study of Miocene rocks bearing micro-organic material and the magnetic mineral greigite (Sokolov and Cheb basins, Czechoslovakia). *Phys. Earth Planet. Inter.,* 63:98–112.

Lagoe, M.B., and Thompson, P.R., 1988. Chronostratigraphic significance of Late Cenozoic planktonic foraminifera from the Ventura Basin, California: potential for improving tectonic and depositional interpretation. *J. Foraminiferal Res.,* 18:250–266.

Lovell, M.A., 1984. Thermal conductivity and permeability assessment by electrical resistivity measurements in marine sediments. *Mar. Geotechnol.,* 6:205–240.

Lundberg, N., and Moore, J.C., 1986. Macroscopic structural features in Deep Sea Drilling Project cores from forearc regions. *In* Moore, J.C. (Ed.), *Structural Fabrics Preserved in Deep Sea Drilling Project Cores From Forearcs.* Mem.—Geol. Soc. Am., 166:13–44.

Marlowe, I.T., Brassell, S.C., Eglinton, G., and Green, J.C., 1984. Long-chain unsaturated ketones and esters in living algae and marine sediments. *In* Schenck, P.A., de Leeuw, J.W., and Lijmbach, G.W.M. (Eds.), *Advances in Organic Geochemistry 1983.* Org. Geochem., 6:135–141.

Musgrave, R.J., Delaney, M.L., Stax, R., and Tarduno, J.A., 1993. Magnetic diagenesis, organic input, interstitial water chemistry, and paleomagnetic record of the carbonate sequence on the Ontong Java Plateau. *In* Berger, W.H., Kroenke, L.W., Mayer, L.A., et al., *Proc. ODP, Sci. Results,* 130: College Station, TX (Ocean Drilling Program), 527–546.

Mutti, E., and Ricci Lucchi, F., 1972. Le torbiditi dell'Appennino settentrional: introduzione all'analisi di facies. *Mem. Soc. Geol. Ital.,* 11:161–199.

Nigrini, C.A., and Caulet, J.P., 1992. Late Neogene radiolarian assemblages characteristic of Indo-Pacific areas of upwelling. *Micropaleontology,* 38:139–164.

Oremland, R.S., Whiticar, M.J., Strohmaier, F.E., and Kiene, R.P., 1988. Bacterial ethane formation from reduced, ethylated sulfur compounds in anoxic sediments. *Geochim. Cosmochim. Acta,* 52:1895–1904.

Riddihough, R.P., 1977. A model for recent plate interactions off Canada's west coast. *Can. J. Earth Sci.,* 14:384–396.

Scheidegger, K.F., Kulm, L.D., and Piper, D.J.W., 1973. Heavy mineralogy of unconsolidated sands in northeastern Pacific sediments: Leg 18, Deep Sea Drilling Project. *In* Kulm, L.D., von Huene, R., et al., *Init. Repts. DSDP,* 18: Washington (U.S. Govt. Printing Office), 877–888.

Shipboard Scientific Party, 1973. Site 174. *In* Kulm, L.D., von Huene, R., et al., *Init. Repts. DSDP,* 18: Washington (U.S. Govt. Printing Office), 97–168.

————, 1991. Site 808. *In* Taira, A., Hill, I., Firth, J.V., et al., *Proc. ODP, Init. Repts.,* 131: College Station, TX (Ocean Drilling Program), 71–272.

Siemers, C.T., Tillman, R.W., and Williamson, C.R., 1981. *Deep Water Clastic Sediments: A Core Workshop.* Soc. Econ. Paleontol. Mineral. Core Workshop No. 2, San Francisco.

Simoneit, B.R.T., 1977. Diterpenoid compounds and other lipids in deep-sea sediments and their geochemical significance. *Geochim. Cosmochim. Acta,* 41:463–476.

————, 1978. The organic geochemistry of marine sediments. *In* Riley, J.P., and Chester, R. (Eds.), *Chemical Oceanography* (Vol. 7): London (Academic Press), 233–311.

Spence, G.D., Hyndman, R.D., Davis, E.E., and Yorath, C.J., 1991. Marine multichannel seismic reflection data across the continental margin of Vancouver Island. *Geol. Surv. Can., Open File Rep.,* 2391.

Suess, E., and Whiticar, M.J., 1989. Methane-derived CO_2 in pore fluids expelled from the Oregon subduction zone. *Palaeogeogr., Palaeoclimatol., Palaeoecol.,* 71:119–136.

Tric, E., Laj, C., Valet, J.-P., Tucholka, P., Paterne, M., and Guichard, F., 1991. The Blake geomagnetic event: transition geometry, dynamical characteristics and geomagnetic significance. *Earth Planet. Sci. Lett.,* 102:1–13.

Volkman, J.K., Eglinton, G., Corner, E.D.S., and Sargent, J.R., 1980. Novel unsaturated straight-chain C_{37}–C_{39} methyl and ethyl ketones in marine sediments and a coccolithophore *Emiliania huxleyi. In* Douglas, A.G., and Maxwell, J.R. (Eds.), *Advances in Organic Geochemistry 1979:* Oxford (Pergamon Press), 219–228.

Wang, K., Hyndman, R.D., and Davis, E.E., 1993. Thermal effects of sediment thickening and fluid expulsion in accretionary prisms: model and parameter analysis. *J. Geophys. Res.,* 98:9975–9984.

Wang, M.C., Nacci, V.A., and Markert, C.D., 1976. Electrical resistivity method for marine sediment consolidation study. *Proc. 8th Ann. Offshore Technol. Conf.,* Houston, TX, Pap. 2623.

Waxman, M.H., and Smits, L.J.M., 1968. Electrical conductivities in oil-bearing shaly sands. *SPEJ, Soc. Pet. Eng. J.,* 8:107–122.

Whiticar, M.J., 1990. A geochemical perspective of natural gas and atmospheric methane. *In* Durand, B., and Behar, F. (Eds.), *Advances in Organic Geochemistry 1989.* Org. Geochem., 16:531–547.

Whiticar, M.J., Faber, E., and Schoell, M., 1986. Biogenic methane formation in marine and freshwater environments: CO_2 reduction vs. acetate fermentation—isotope evidence. *Geochim. Cosmochim. Acta,* 50:693–709.

Whiticar, M.J., and Suess, E., 1989. Hydrothermal hydrocarbon gases in the sediments of the King George Basin, Bransfield Strait, Antarctica. *In* Simoneit, B.R.T. (Ed.), *Geochemistry of Hydrothermal Systems.* Appl. Geochem., 5:135–147.

Winsauer, W.O., Shearing, H.M., Jr., Masson, P.H., and Williams, M., 1952. Resistivity of brine saturated sands in relation to pore geometry. *AAPG Bull.,* 36:253–277.

Yorath, C.J., Clowes, R.M., MacDonald, R.D., Spencer, C., Davis, E.E., Hyndman, R.D., Rohr, K., Sweeney, J.F., Currie, R.G., Halpenny, J.F., and Seemann, D.A., 1987. Marine multichannel seismic reflection, gravity and magnetic profiles—Vancouver Island continental margin and Juan de Fuca Ridge. *Geol. Surv. Can., Open File Rep.,* 1661.

Zehnder, A.J.B. (Ed.), 1988. *Biology of Anaerobic Microorganisms:* New York (Wiley).

Ms 146IR-007

NOTE: For all sites drilled, core-description forms ("barrel sheets") and core photographs can be found in Section 6, beginning on page 429. Forms containing smear-slide data can be found in Section 7, beginning on page 591.

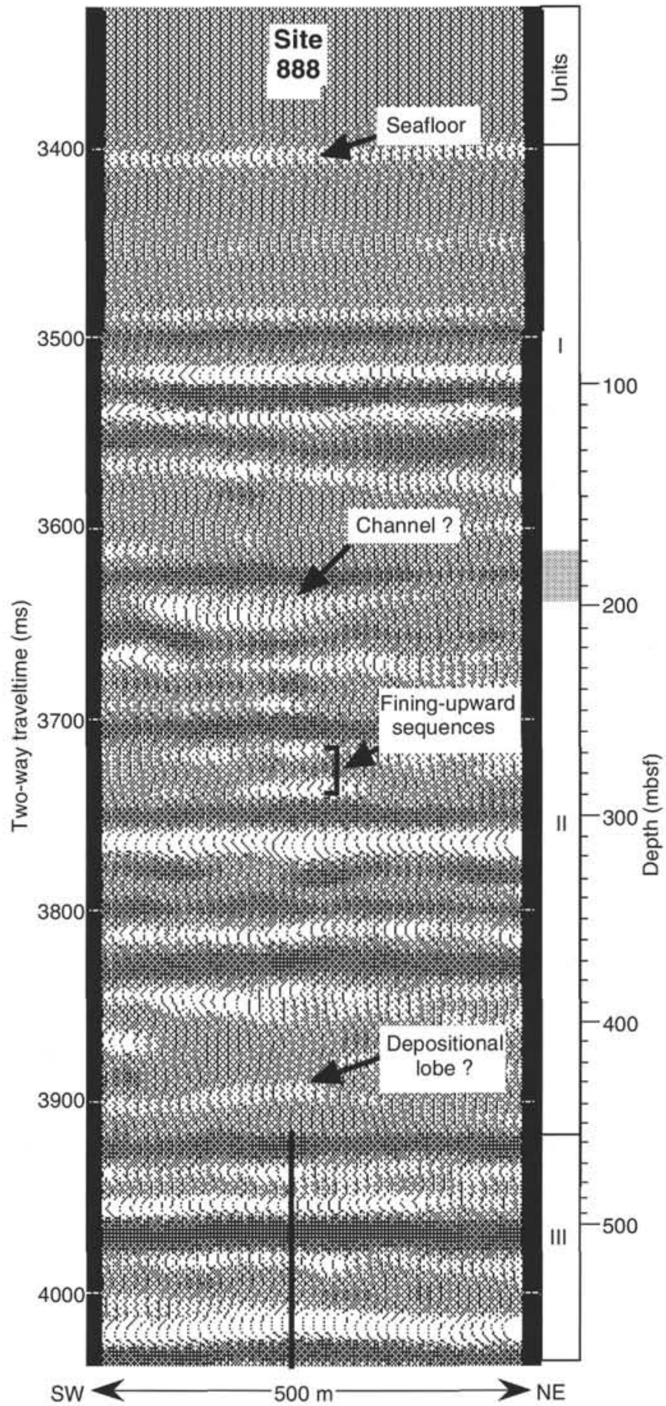

Figure 74. Comparison of lithostratigraphic units and seismic data (line 89-04; see "Seismic Stratigraphy" section, this chapter). Depth scale from synthetic seismogram (Fig. 73). Note how Unit II shows a preponderance of laterally discontinuous reflectors, some of which resemble the channels and lobes of submarine fan complexes. The "Channel?" feature is marked in the caliper log by the first extensive washout (thick sand), which ranges from 193 to about 225 mbsf. Above 193 mbsf a series of smaller washouts (thinner sands) marks the transition to an in-gauge (mudstone-rich) section in Unit I. This transition may represent a thinning- and fining-upward sequence. Two fining-upward sequences apparent on the caliper log between 268 and 290 mbsf may be represented by prominent reflections on the seismic data.

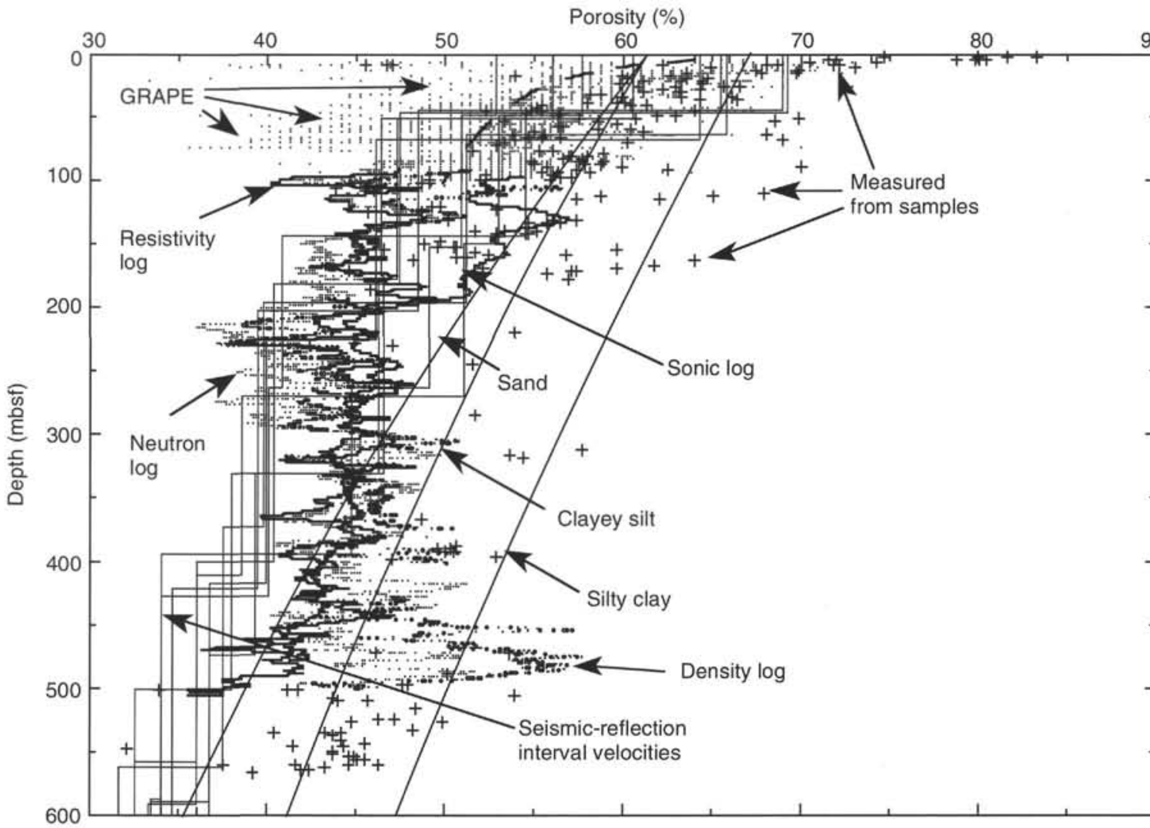

Figure 75. Comparison of porosity as a function of depth, derived from shipboard measurements of physical properties, from geophysical logs down Hole 888C, and from seismic interval velocities obtained from multichannel seismic-reflection line 89-04. Measurements of porosity made on samples with a pycnometer are represented by plus signs. Porosity estimated from the GRAPE-determined bulk density, using a grain density of 2.8 Mg/m^3, is shown by individual points that plot on vertical lines spaced by the measurement increment. The thick dashed line is the best-fitting logarithmic curve through the GRAPE data. The curves for the porosities derived from the density log, neutron log, resistivity log, sonic log, and seismic-reflection data are indicated by labels. Porosity was derived from the density log, using a grain density of 2.8 Mg/m^3. Porosity was derived from the sonic log and seismic-reflection data using the empirically derived relation: porosity $= -1.18 + 8.607/\text{velocity} - 17.89/\text{velocity}^2 + 13.94/\text{velocity}^3$, from Hyndman et al. (1993). Also shown are empirically derived reference curves for normally compacted sand, clayey silt, and silty clay, from Brückmann (1989).

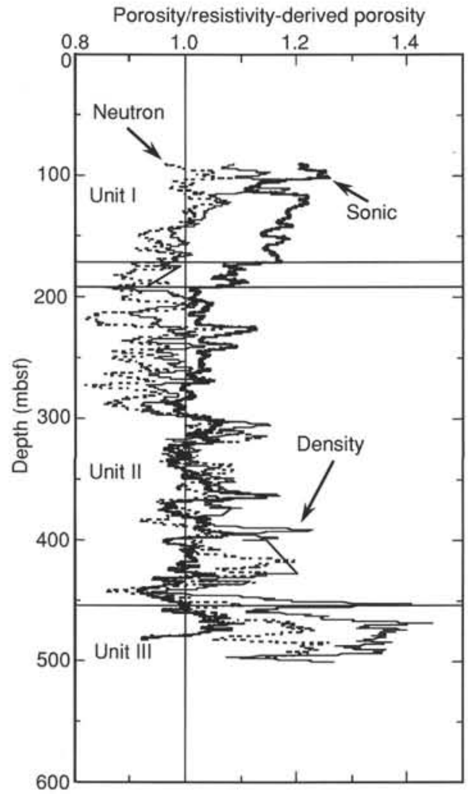

Figure 76. Comparison of the porosity/depth curves derived from the density, neutron, and sonic logs expressed as ratios of the porosity derived from the resistivity log.

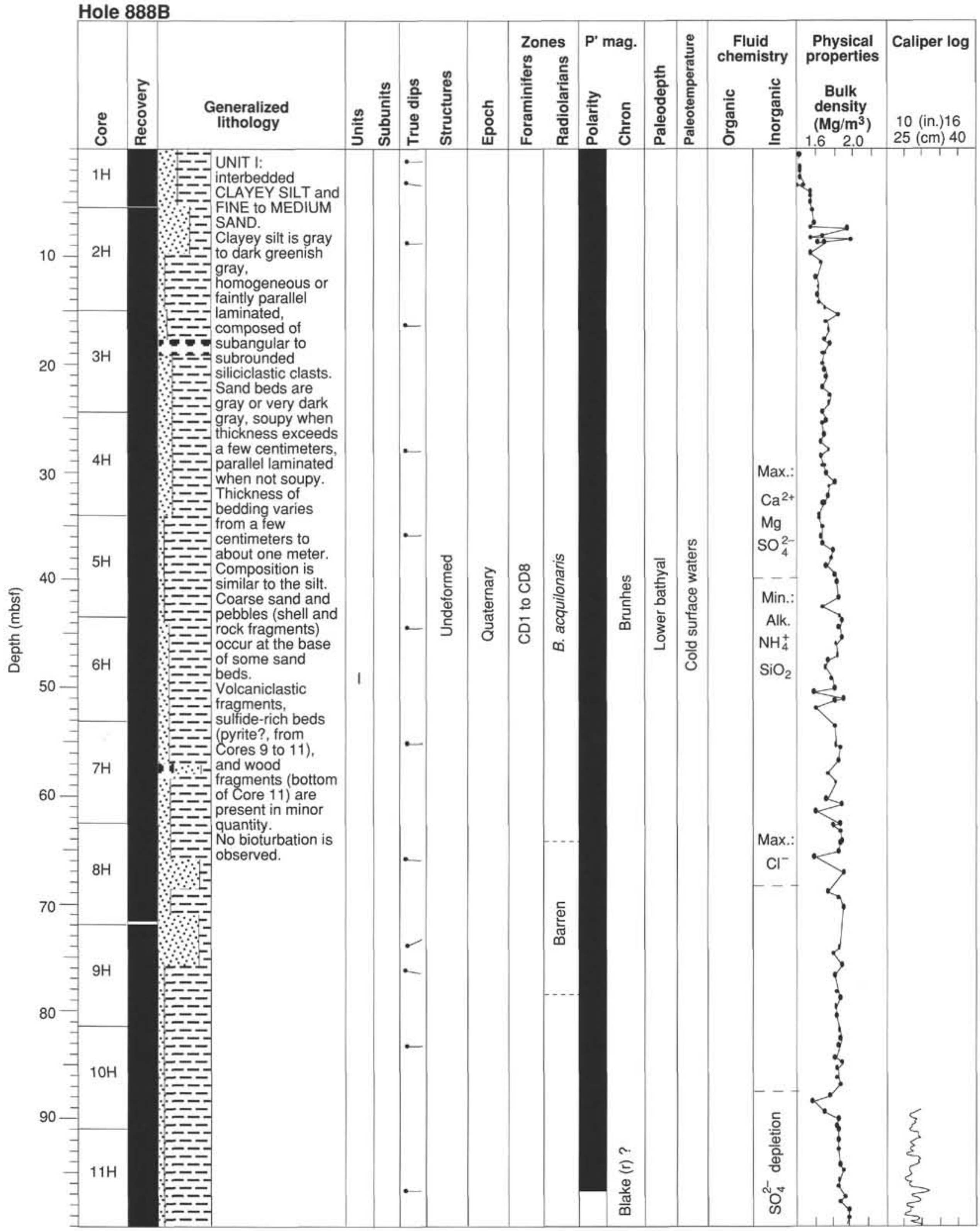

Figure 77. Master chart, Hole 888B.

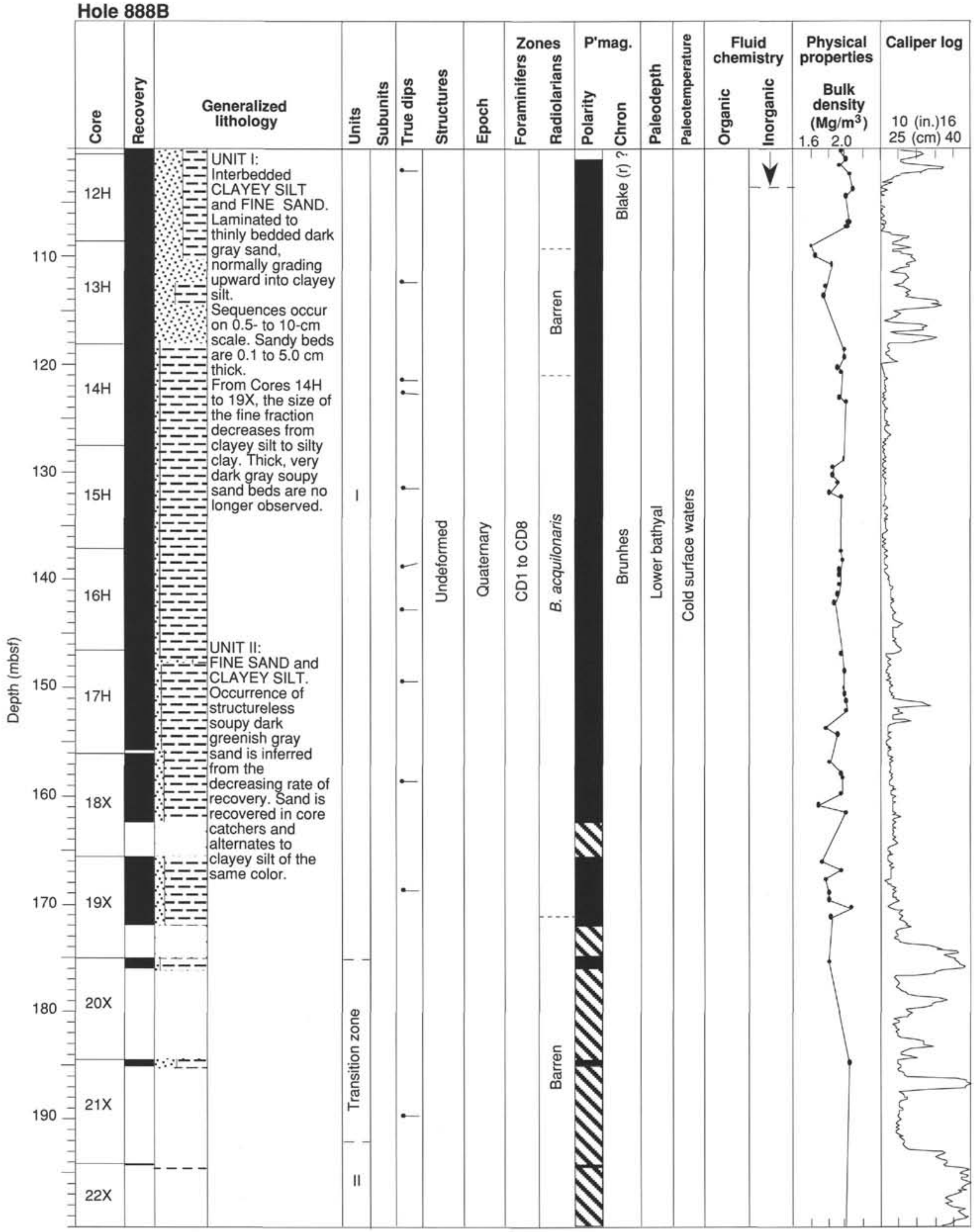

Figure 77 (continued).

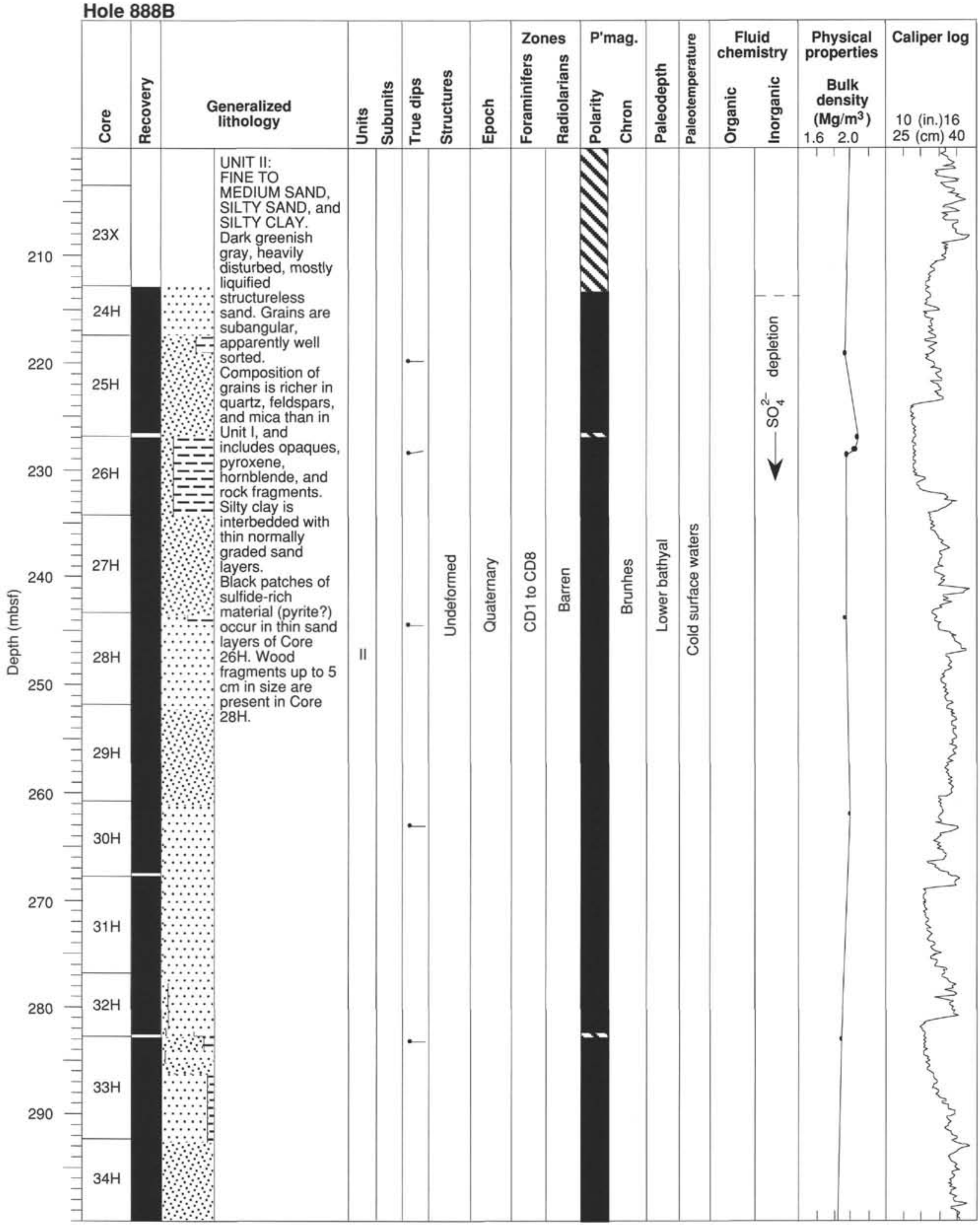

Figure 77 (continued).

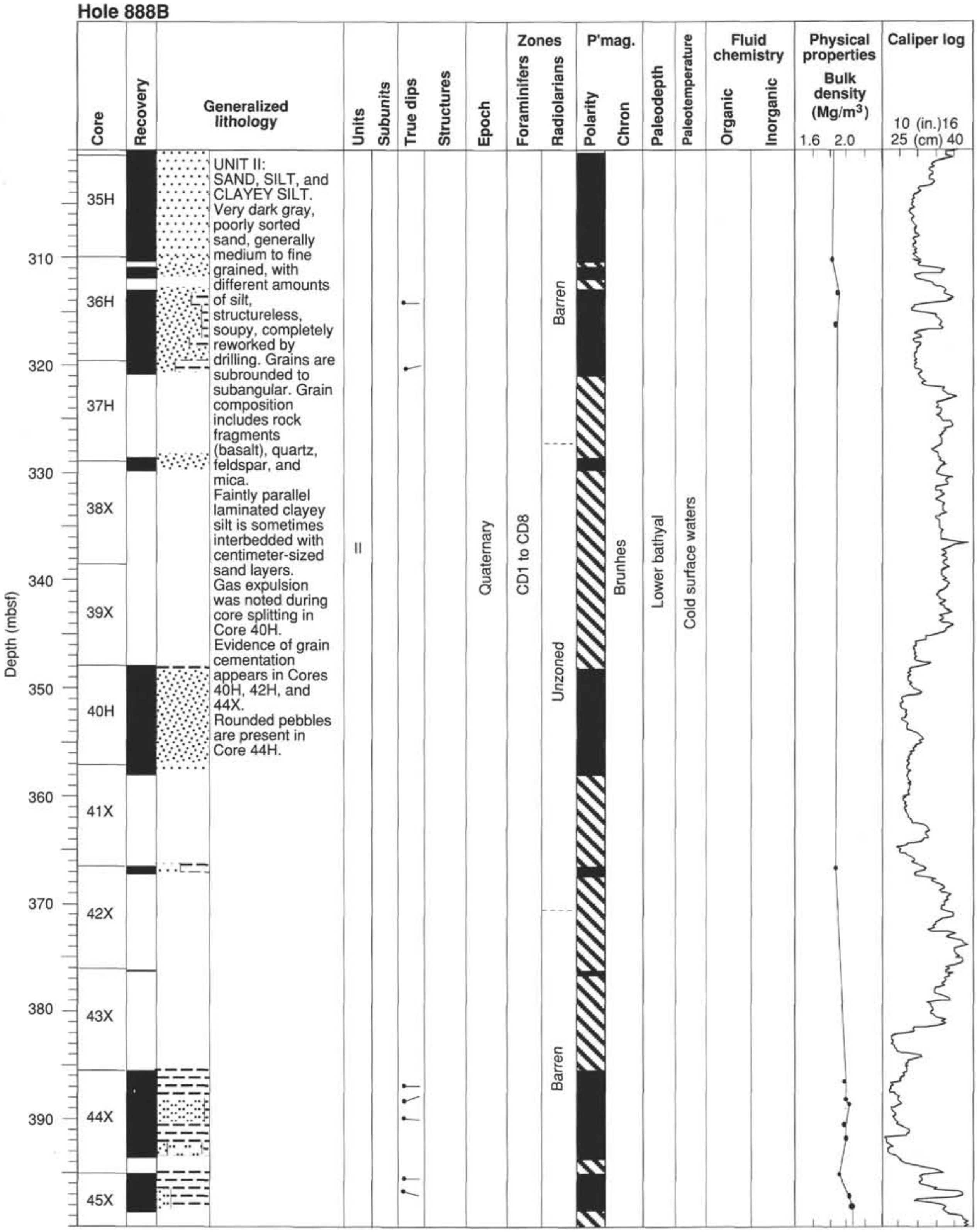

Figure 77 (continued).

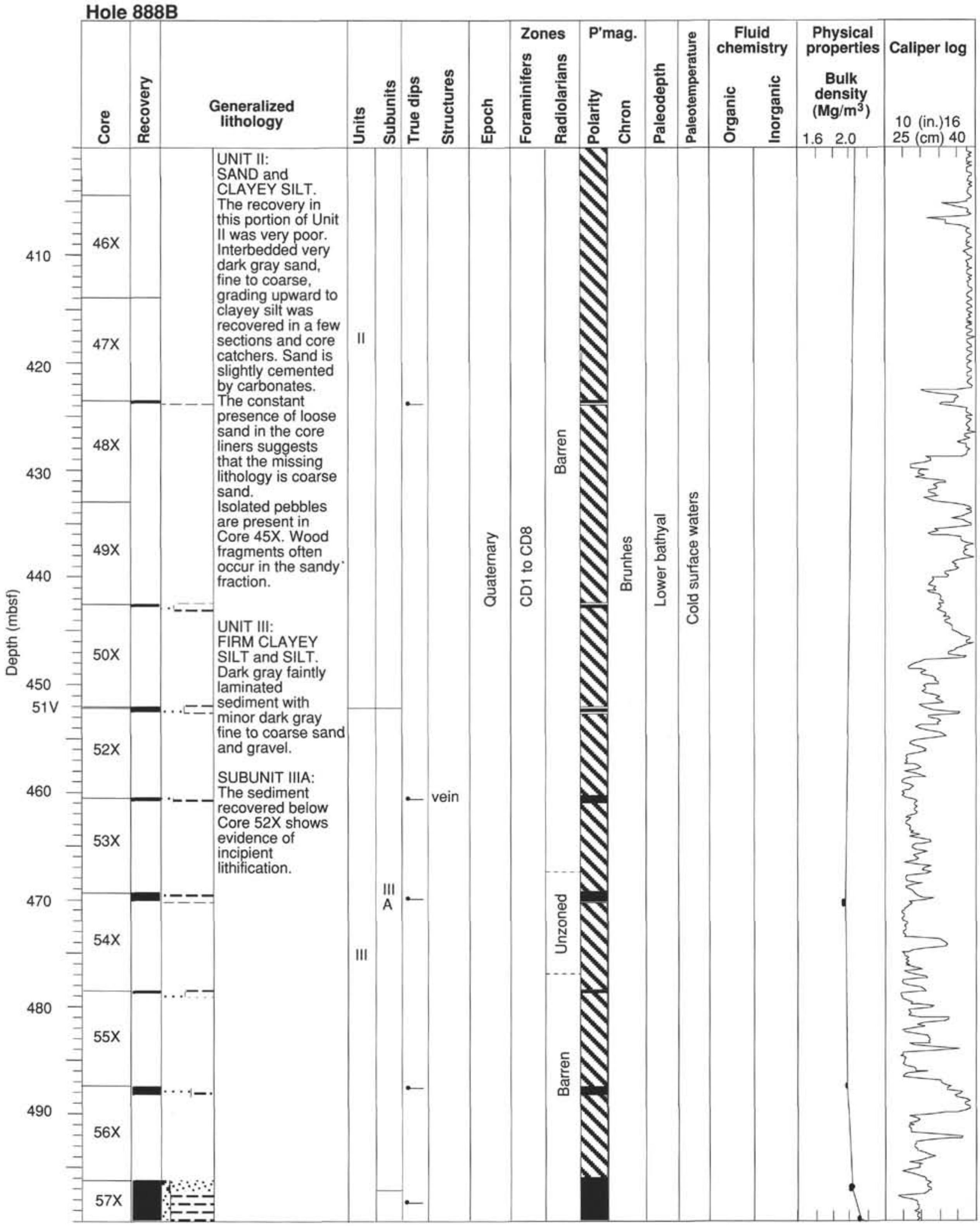

Figure 77 (continued).

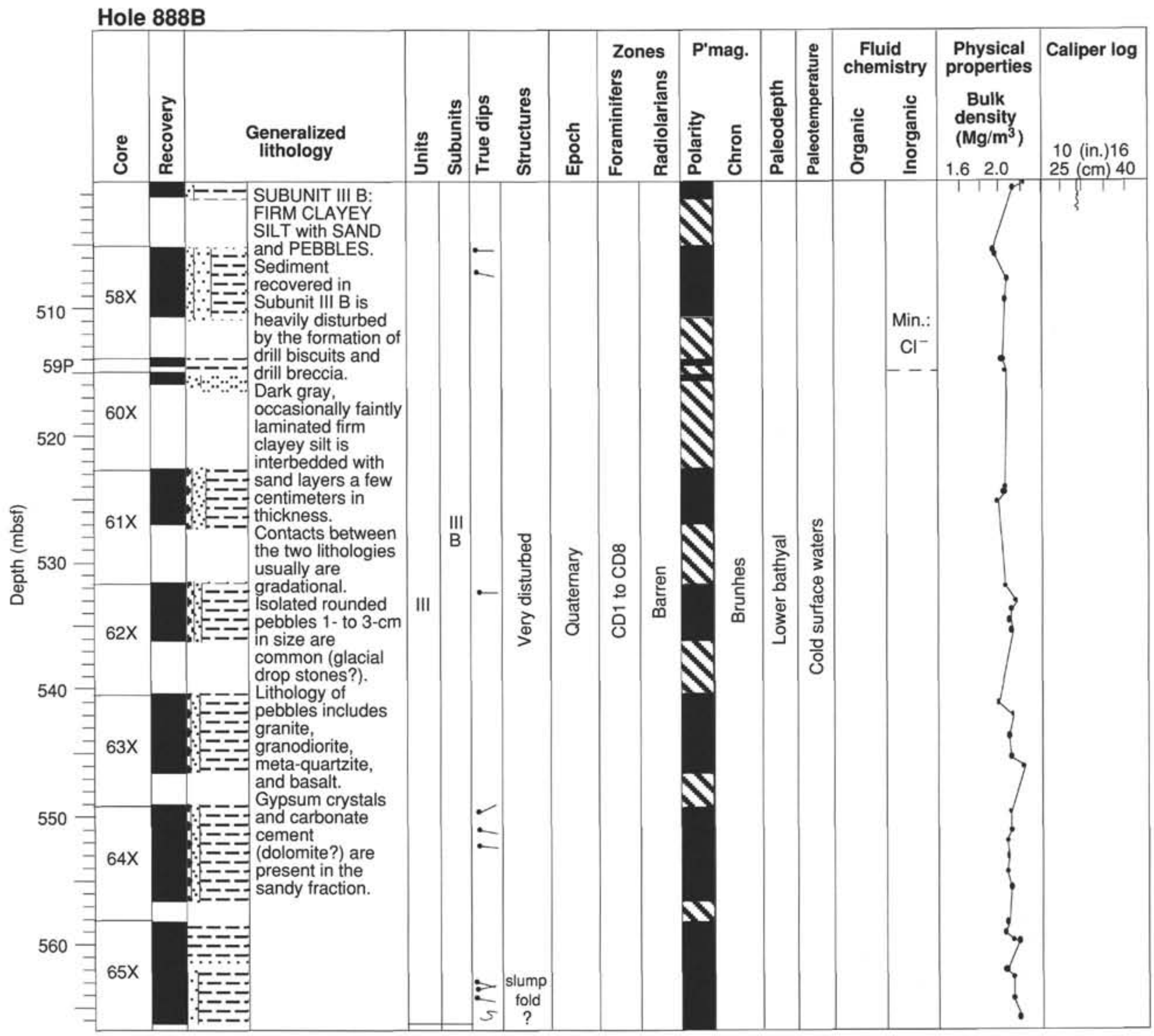

Figure 77 (continued).

Hole 888C: Resistivity-Velocity-Natural Gamma Ray Log Summary

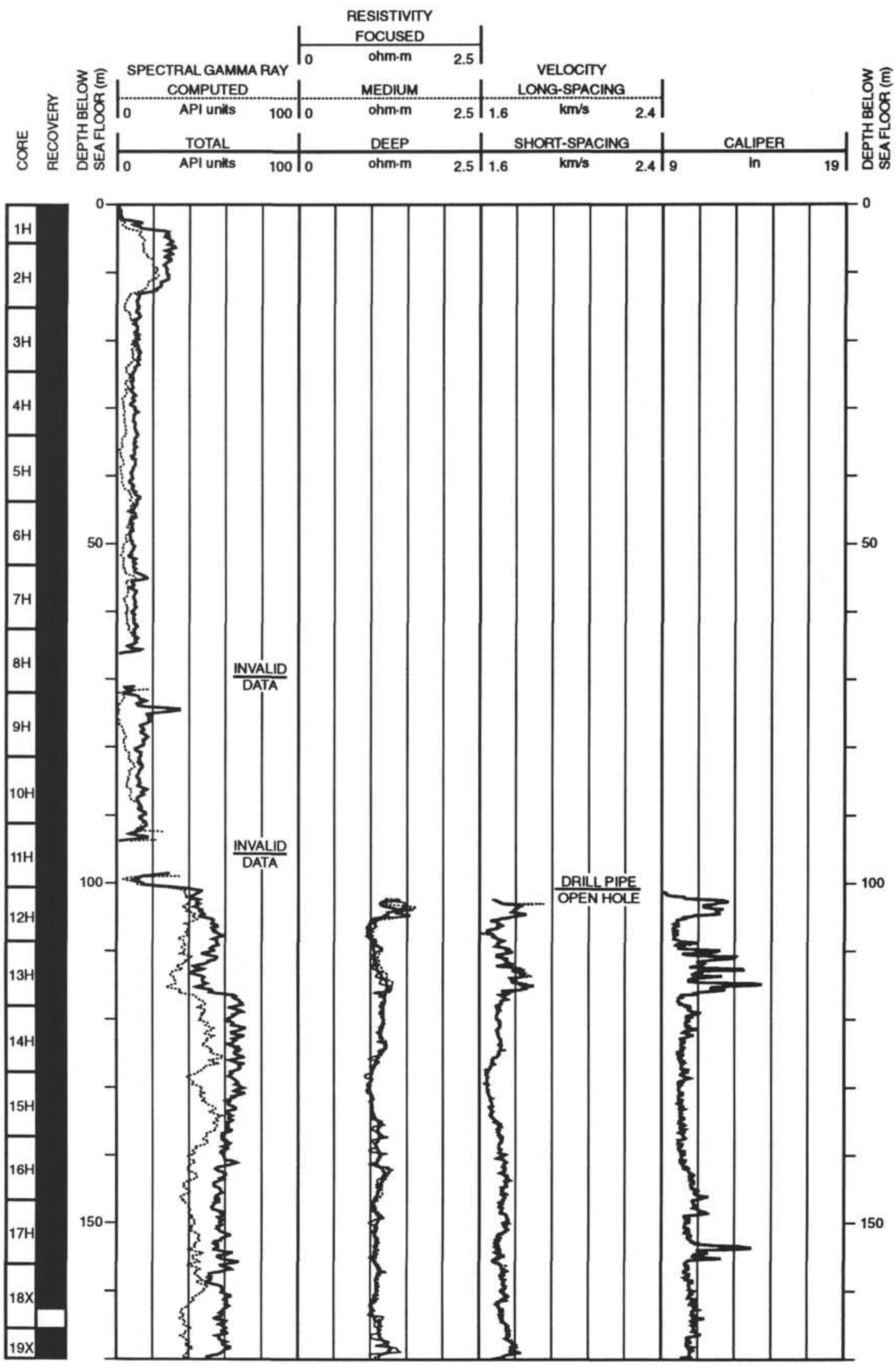

Hole 888C: Resistivity-Velocity-Natural Gamma Ray Log Summary (continued)

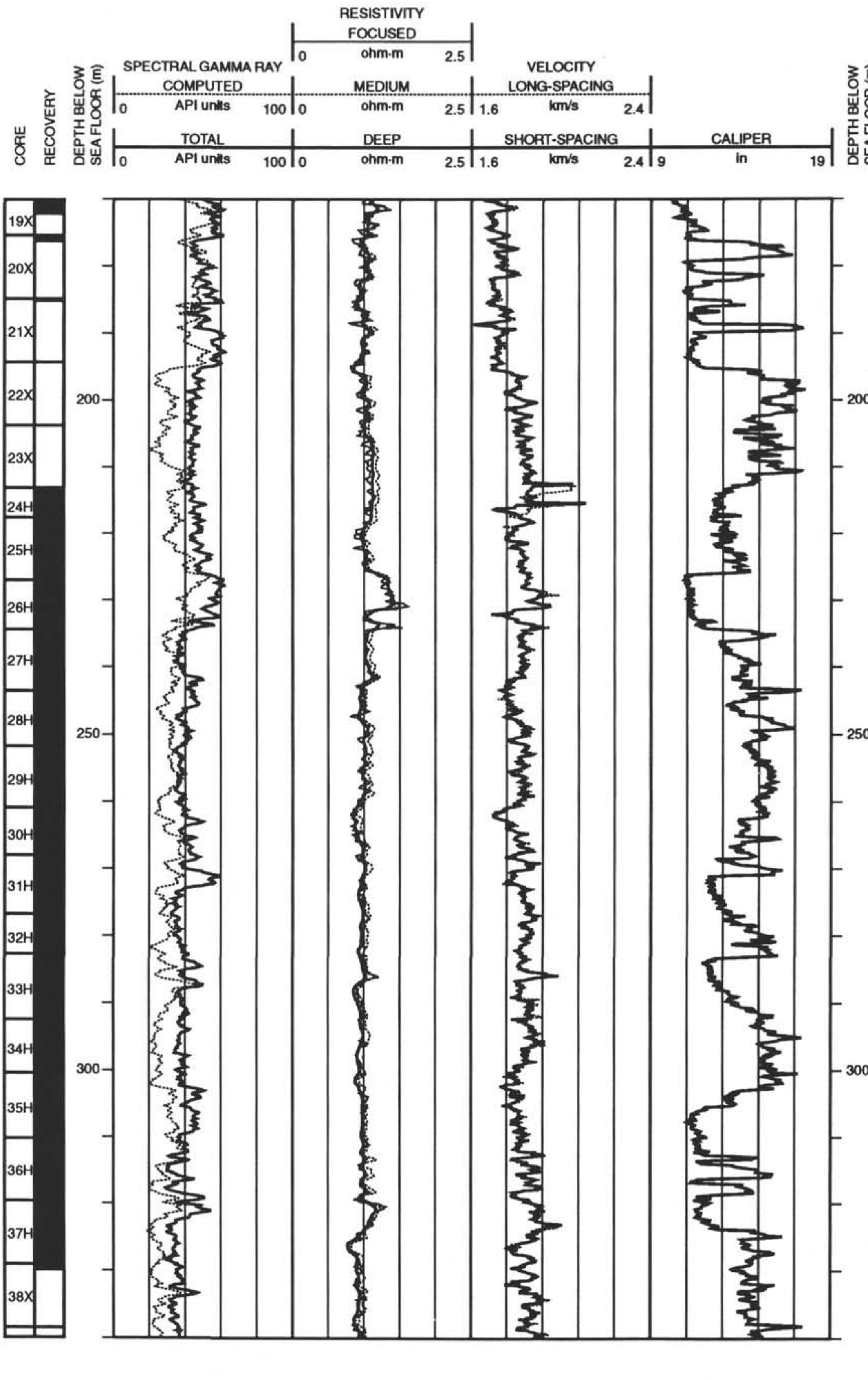

Hole 888C: Resistivity-Velocity-Natural Gamma Ray Log Summary (continued)

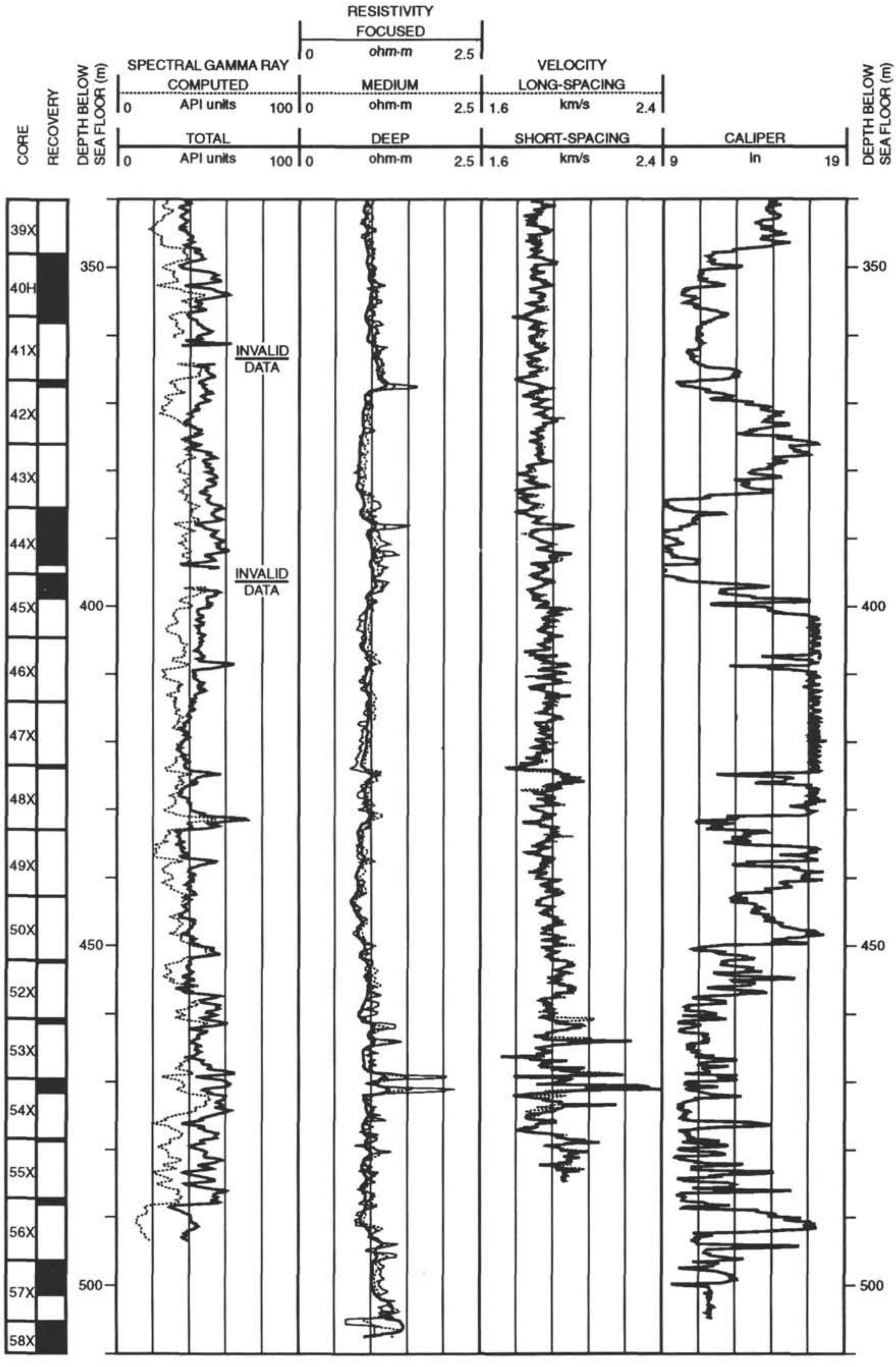

Hole 888C: Density-Porosity-Natural Gamma Ray Log Summary

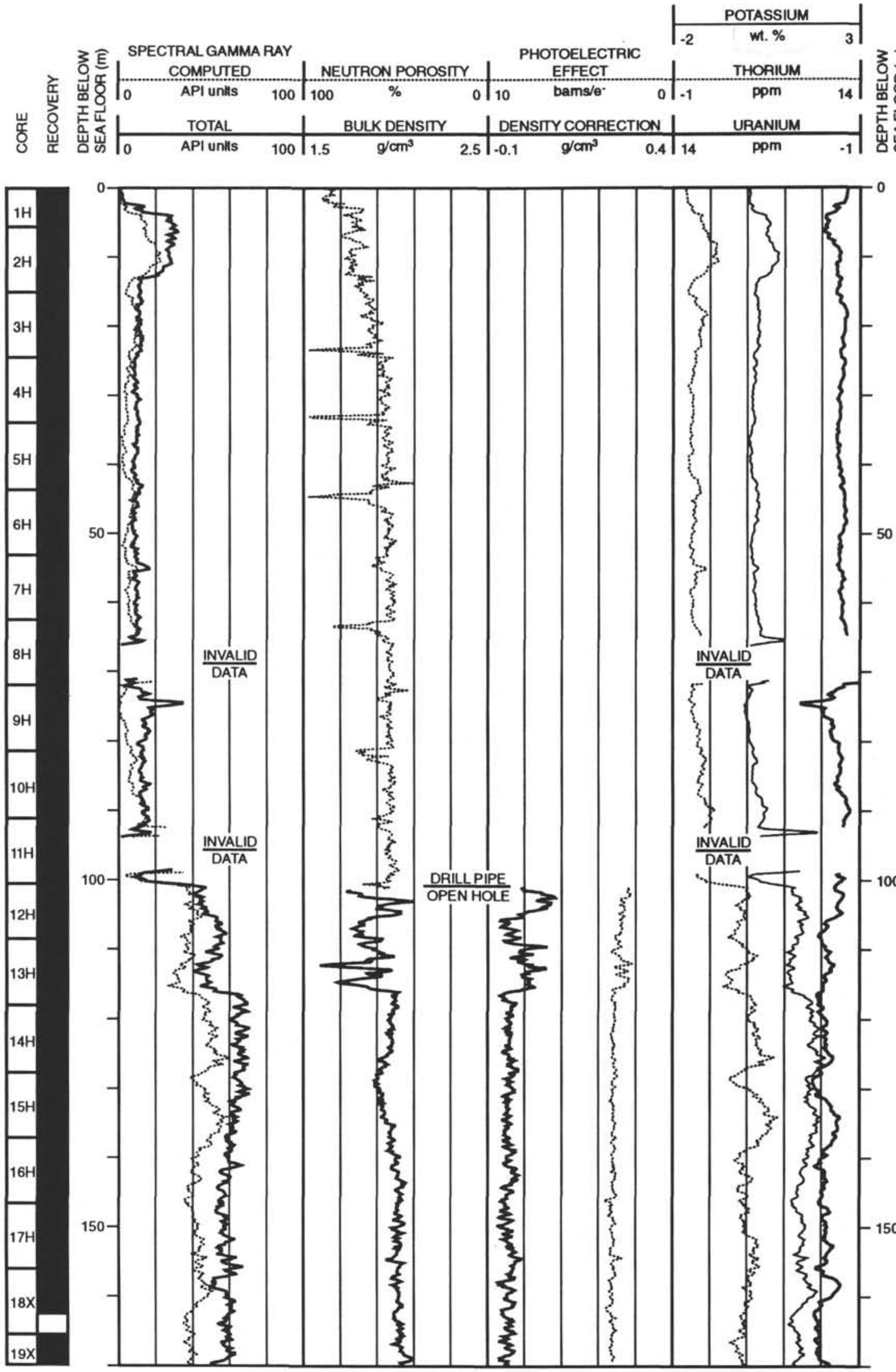

Hole 888C: Density-Porosity-Natural Gamma Ray Log Summary (continued)

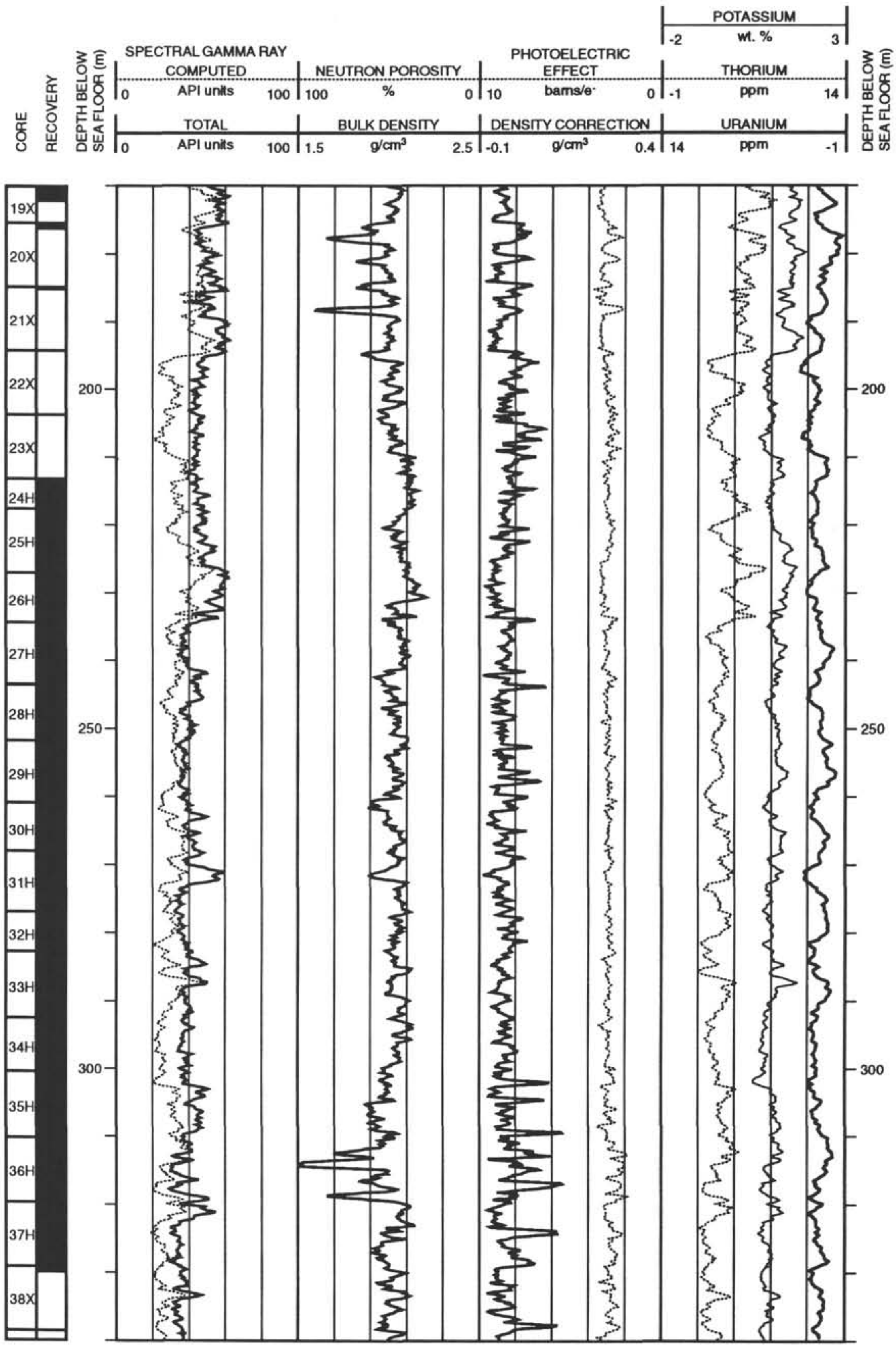

Hole 888C: Density-Porosity-Natural Gamma Ray Log Summary (continued)